

Study of the Silicon Photomultipliers and Their Applications in Positron Emission Tomography

Dissertation

zur Erlangung des Doktorgrades
des Department Physik
der Universität Hamburg

vorgelegt von

CHEN XU

aus Beijing, China

Hamburg
2014

Gutachter/in der Dissertation:	Prof. Dr. Erika Garutti Prof. Dr. Peter Schleper
Gutachter/in der Disputation:	Prof. Dr. Erika Garutti Prof. Dr. Grüner Florian
Datum der Disputation:	16.05.2014
Vorsitzender des Prüfungsausschusses:	Prof. Dr. Dieter Horns
Vorsitzender des Promotionsausschusses:	Prof. Dr. Daniela Pfannkuche
Leiter des Departments Physik:	Prof. Dr. Peter Hauschildt
Dekan des MIN-Fakultät:	Prof. Dr. Heinrich Graener

Abstract

This thesis deals with silicon photomultipliers (SiPM) used in scintillation detectors and their applications in positron emission tomography (PET). The study of the SiPM is mainly focused on the application to the proposed EndoTOFPET-US detector, which is a multi-modality PET detector facilitating the development of new biomarkers for pancreas and prostate cancers.

A Monte Carlo simulation tool is developed for the optimization of the detector's single channel design. In order to obtain a 200 ps system coincidence time resolution and maximize the detector sensitivity, the requirements for the crystal geometry, light yield and SiPM photon detection efficiency are specified based on the simulation study. In addition, the nonlinear response of the SiPM can be corrected by the simulation tool and the energy resolution of the detector is extracted.

A series of measurements are established to characterize SiPMs in a fast and reliable way with high precision. The static characterization measures the value of different components in the derived electrical model of the SiPM, whereas the dynamic characterization extracts parameters that is crucial for the operation of the SiPM. Several SiPM samples are tested and their characteristics are compared. The developed setup and the precision of the measurement fulfill the requirements of the quality assurance test for the commissioning of the EndoTOFPET-US detector. The test foresees large quantities of SiPMs to be characterized. In addition, the developed measuring procedure has contributed to the study of X-ray induced surface damage of a SiPM from Hamamatsu. Characteristics of the device are measured before and after irradiating the SiPM with different X-ray doses, the results are compared and discussed.

A comparative study of a digital and an analog SiPM in gamma spectroscopy with the inorganic scintillator is presented. The characteristics of a prototype digital SiPM that is developed for the EndoTOFPET-US detector is measured and compared to an analog SiPM with similar form factor. Its non linear response to scintillation light is corrected by the simulation tool and the energy resolution is extracted. The work validates the digital SiPM to be a viable solution for the EndoTOFPET-US detector.

Zusammenfassung

Diese Arbeit befasst sich mit Silizium Photomultipliern (SiPM), die in Szintillationsdetektoren verwendet werden und behandelt ihre Anwendung in der Positronen-Emissions-Tomographie (PET). Die vorliegende Studie der SiPMs konzentriert sich hauptsächlich auf ihre Anwendung in dem EndoTOFPET-US Detektor, einem multimodalen PET-Detektor, der die Entwicklung von Biomarkern für Bauchspeicheldrüsen- und Prostata-Krebs ermöglicht.

Zur Optimierung der einzelnen Kanäle des Detektors wurde ein Monte-Carlo-Simulationswerkzeug entwickelt. Mit Hilfe solcher Simulationsstudien werden die Anforderungen an die Kristallgröße, Lichtausbeute und Photon-Detektions-Effizienz des SiPMs festgelegt, um die geplante Koinzidenz-Zeitauflösung von 200 ps zu erhalten und damit die Sensitivität des Detektorsystems zu maximieren. Außerdem können daraus Nichtlinearitäten des SiPMs korrigiert, und somit die Energieauflösung ermittelt werden.

Zur schnellen und genauen Charakterisierung der SiPM wurde eine Reihe von Messverfahren genutzt. Die statische Charakterisierung misst verschiedene Komponenten in dem abgeleiteten elektrischen Modell des SiPM. Die dynamische Charakterisierung untersucht weitere Eigenschaften des SiPM, die von dem Betrieb des SiPM abhängig sind. Unterschiedliche SiPM-Typen wurden getestet und ihre Eigenschaften verglichen. Die vorgestellten Messungen erfüllen die Anforderungen des Qualitätssicherungstests, der große Menge von SiPMs, die im EndoTOFPET-US-Detektor in Betrieb genommen werden, charakterisiert. Die entwickelten Messverfahren haben zur Untersuchung von Beschädigungen durch Röntgenstrahlen an der Oberfläche eines Hamamatsu SiPMs beigetragen. Eigenschaften des SiPMs wurden gemessen, bevor und nachdem sie mit unterschiedlichen Röntgendosen bestrahlt wurden. Die Ergebnisse werden in der vorliegende Arbeit verglichen und diskutiert.

Zusätzlich wird eine vergleichende Studie von digitalen und analogen SiPM in der Gammaspektroskopie mit anorganischen Szintillatoren vorgestellt. Die Eigenschaften eines digitalen SiPM-Prototypen, der für den EndoTOFPET-US Detektor entwickelt wurde, werden gemessen und mit einem analogen SiPM mit ähnlichem Formfaktor verglichen. Die Nichtlinearität der SiPM auf Szintillationslicht wird durch das Simulationswerkzeug korrigiert, um die Energieauflösung zu ermitteln. Die Arbeit bestätigt, dass die digitalen SiPMs eine praktikable Lösung für den EndoTOFPET-US Detektor sind.

Contents

1	Introduction	1
1.1	Positron Emission Tomography	1
1.2	The EndoTOFPET-US Project	2
1.3	Calorimetry	3
1.4	Thesis Outline	3
2	Principle of PET	5
2.1	Positron Emission	5
2.2	Photon Interactions with Matter	6
2.2.1	Photoelectric Effect	7
2.2.2	Compton Effect	8
2.2.3	Pair-Production	10
2.3	Time-of-Flight PET	10
2.4	Scintillation Detector	12
2.4.1	Scintillator	12
2.4.2	Photodetectors	15
2.4.3	Readout Electronics	18
3	The EndoTOFPET-US Detector Design	23
3.1	The PET Detector Head	24
3.2	The External Detector Plate	25
3.3	Data Acquisition	27
4	Monte Carlo Simulation	29
4.1	Single Channel Simulation	29
4.1.1	General Concept	29
4.1.2	Detector Construction	30
4.1.3	Physics List	31
4.2	Single Channel Optimization	34
4.2.1	Sensitivity	34
4.2.2	Simulation of the SiPM and MD-SiPM	35
4.2.3	Coincidence Time Resolution	36
4.2.4	Energy Resolution	39
4.3	Summary	40

5	Silicon Photomultiplier	43
5.1	Silicon Photodetectors	43
5.1.1	PIN Photodiodes	43
5.1.2	Charge-Coupled Device	45
5.1.3	Avalanche Photodiodes	45
5.1.4	Geiger Mode APDs (SPAD)	47
5.2	Theoretical Basis	48
5.2.1	SPAD breakdown voltage	48
5.2.2	SPAD Quenching	52
5.3	Figures of Merit of a SiPM	54
5.3.1	Gain	54
5.3.2	Dynamic Range	55
5.3.3	Dark Noise	57
5.3.4	Optical Cross Talk	58
5.3.5	Afterpulses	59
5.3.6	Photon Detection Efficiency	60
5.3.7	Single Pixel Time Resolution	61
6	Characterization of the SiPM	63
6.1	Static Characteristics	64
6.1.1	Forward Current	64
6.1.2	Reverse Current	66
6.1.3	Capacitance and Conductance Measurements	67
6.2	Dynamic Characteristics	72
6.2.1	Gain and Breakdown Voltage	73
6.2.2	Fitting Methods for Gain Extraction	78
6.2.3	Noise	81
6.2.4	Signal Pulse Analysis	84
6.3	Summary and Comparison	85
6.3.1	Quenching resistance	85
6.3.2	Breakdown Voltage	85
6.3.3	Gain and Pixel capacitance	85
6.3.4	Signal Decay Time	86
6.3.5	Noise	86
7	The Digital SiPM	89
7.1	The MD-SiPM Prototype	89
7.1.1	Dark Count Rate	90
7.1.2	Trigger Validation	91
7.1.3	MD-SiPM Response Function	93
7.1.4	Scintillator Measurement	94
7.2	Comparison between MD-SiPM and MPPC	96
7.2.1	Scintillation measurement of the MPPC	96
7.2.2	Comparison	97
7.3	Conclusion	99

8	Radiation Damage to SiPM	101
8.1	X-ray Radiation Damage in Silicon Detector	101
8.2	X-ray Irradiation	102
8.3	SiPM Characteristics Before and After Irradiation	102
8.3.1	Forward Current	102
8.3.2	Reverse Current	103
8.3.3	C/G versus Frequency	105
8.3.4	Gain and Breakdown Voltage	106
8.3.5	Dark Count Rate	106
8.3.6	The Correlated Noise	107
8.3.7	Pulse Shape	107
8.4	Discussion of the Results	109
9	Conclusion	111
	Bibliography	113
	Acknowledgements	119

Nomenclature

^{18}F -FDG ^{18}F -Fluoro-Deoxy-Glucose

ADC Analog-to-Digit Converter

APD Avalanche PhotoDiode

ASIC Application Specific Integrated Circuit

CE Collection Efficiency

CFD Constant Fraction Discriminator

CMOS Complementary Metal-Oxide-Semiconductor

CT Computed Tomography

CTR Coincidence Time Resolution

DAQ Data Acquisition

DCR Dark Count Rate

dSiPM Digital Silicon Photomultiplier

ENC Equivalent Noise Charge

EndoTOFPET-US Endoscopic Time-Of-Flight Positron Emission Tomography and Ultrasound

ENF Excess Noise Factor

FEB Front End Board

FPGA Field Programmable Gate Array

FWHM Full-Width at Half-Maximum

GAPD Geiger-mode Avalanche Photodiode

LOR Line-Of-Response

MC Monte Carlo

MD-SiPM Multi-channel Digital SiPM

MPPC Multi-Pixel Photon Counter, name of the SiPM produced by Hamamatsu

MRI	Magnetic Resonance Imaging
PCB	Printed Circuit Board
PDE	Photon Detection Efficiency, product of fill factor and photon detection probability
PDF	Probability Density Function
PDP	Photon Detection Probability, product of quantum efficiency and avalanche triggering probability
PEB	Premature Edge Breakdown
PET	Positron Emission Tomography
PMT	Photomultiplier Tube
QDC	Charge-to-Digital Converter
QE	Quantum Efficiency
SER	Single-photoElectron Response
SiPM	Silicon PhotoMultiplier
SPAD	Single Photon Avalanche Diode
SR	“Smart Reset”
STR	Single (detector channel) Time Resolution
TDC	Time-to-Digit Converter
TOF	Time-Of-Flight
ToT	Time-over-Threshold

Chapter 1

INTRODUCTION

Ever since the discovery made by Becquerel and Röntgen, radiation and radiation detectors have played an important role in medical diagnostic and therapy. The medical discipline using radioactive substances is known as nuclear medicine. Detector systems are key components to nuclear medicine instrumentations, their properties and performances have great impact on the result in nuclear medicine visualization. Among all different detector system concepts, the scintillation detector is one of the most often and widely used radiation detection devices nowadays.

The first scintillation detector was a Zinc sulfide (ZnS) screen flashing light that is observed by eye through a microscope. It was built in 1903 by Sir William Crookes. The application of this technique got significant boost only after the photomultiplier tube (PMT) was invented in 1930s [1]. For the first time, the PMT provides a quantitative and reliable measurement on the weak light produced by particle interactions in a scintillator. The concept of counting light emitted by a scintillator for radiation detection is still the basis of the modern scintillation detectors. Meanwhile, scintillators and photodetectors are rapidly developed and adopted by high energy physics (HEP) research and medical imaging.

A silicon photomultiplier (SiPM) is a novel semiconductor detector which may compete effectively with the PMT. It shows great potential in replacing the PMT in some fields of application, such as calorimeters for HEP or medical imaging, by providing enhanced properties and new features. The development of SiPM technologies had great progress in recent years. A growing number of SiPM design options for different applications are emerging. The work of this thesis is concerned with the application of SiPMs for Positron Emission Tomography (PET) within the scope of the Endoscopic Time-Of-Flight Positron Emission Tomography and Ultrasound (EndoTOFPET-US) project. In addition, the work also benefits from knowledge exchange relates to SiPMs from the calorimetry development in the HEP community.

1.1 Positron Emission Tomography

Positron Emission Tomography (PET) is a nuclear medicine imaging technique that uses positron annihilation emitted gammas to visualize functional processes in the body. Biologically active compounds labeled with positron-emitting radioisotopes are injected into the human body, their concentration at specific organs or cellular receptors represents certain physiological functions. A PET scan allows the reconstruction of the distribution of radioisotopes, therefore visualizes the physiological function of the body. Compared to anatomic imaging techniques such as Computed Tomography (CT) or Magnetic Resonance Imaging (MRI), PET reveals the cellular level metabolic changes occurring in an organ or tissue.

A large area of clinical use for PET imaging is in oncology. Using the ^{18}F -fluoro-deoxy-glucose (^{18}F -FDG) as the tracer [2], the tissue uptake of glucose can be marked. Since most tumor cells have a high metabolic activity, which means an increased consumption of glucose, the PET image can be effectively used for the diagnosis and staging of cancer diseases. This is valuable because early stage tumors that have not yet caused obvious structural alterations are often not found by morphological images from CT or MRI.

A step further from the PET imaging is the combined imaging modality, in which the functional and anatomic information are acquired simultaneously so that they can be viewed and interpreted together. The combined modality imaging is beneficial in more exactly localizing tumor tissues, which helps in more appropriate treatment during therapy.

The scintillation detector is an essential part of a PET system. Most of nowadays PET systems use the PMT as photodetectors. However, PET systems may benefit from the many unique properties provided by the SiPM. The compactness of SiPMs can greatly increase the granularity of the detector channels in PET, therefore improve the spatial resolution of the image. SiPM's fast timing property is promising for the Time-Of-Flight (TOF) PET technique, where the arrival time of the gamma is used for background rejection and possibly better localization of the annihilation position. With sufficiently high time resolution, the TOF PET technique provides effectively higher signal-to-noise ratio, which is beneficial in improving the image quality, or a faster data acquisition time that could eventually reduce the radiation exposure of the patient. As a semiconductor device, the SiPM is also insensitive to magnetic field. Therefore simultaneous PET/MRI scan using a SiPM facilitated PET is foreseeable whereas the PMT is ruled out in such applications due to its operation principle.

1.2 The EndoTOFPET-US Project

Early detection in pancreatic cancer is crucial for curative treatment. However, existing biomarkers¹ are inadequate for effective early detection [4]. On the other hand, prostate cancer is the most commonly occurring cancer for male patients, and the second leading cause of death by cancer. However, it can be treated with high efficiency provided that the disease is diagnosed during the early stage of development [5, 6].

An European Commission project (EndoTOFPET-US) [7] is devoted to developing new biomarkers of pancreas and prostate tumors. The objective will be addressed using a new endoscopic approach to allow more sensitive, more precise, less invasive imaging and intervention, possibly with lower radiation dose for the patient. The technical objective of the project is to implement a miniaturized TOF PET detector into an ultrasound assisted biopsy endoscopic probe. The proximity of the probe to the affected tissue will increase the probability for detection of smaller functionally marked structures, therefore be helpful in the early diagnosis of pancreatic and prostate cancers. The small geometrical acceptance of the detector, as well as the requirement of an in situ image generation makes the SiPM facilitated TOF PET detector an essential requirement for the project.

The proposed detector from the project has pushed boundaries of the TOF PET technique in terms of geometrical miniaturization, detector time resolution and spatial resolution. It is only possible with the help of the latest technology in the SiPM development. The work of this thesis has involved in the development phase of the detector, a series of studies on the various SiPM technologies are performed and the experimental methods developed from this work paves the way for the final assembly of the new PET detector.

¹Short name for biological marker, a measurable characteristic as an indicator of a particular disease condition [3]

1.3 Calorimetry

As a potential candidate to substitute PMT, SiPM becomes increasingly popular in the calorimeter development in HEP community. Their compactness and insensitivity to magnetic field are the most accentuated properties for future calorimeters. Pioneering detector researching and development from the CALICE collaboration has proposed the analog hadronic calorimeter (AHCAL) using SiPMs to realize unprecedented granularity [8] in a hadronic calorimeter. The proposed new detector consists of tens of millions of plastic scintillators readout by SiPM, which will be able to combine the tracking system and the calorimeter to reconstruct the full event topology in a future linear collider. One of the early requirements is to define a clear selection procedure and develop a reliable way to characterize a massive number of SiPMs. The process requires understanding of the SiPM working principle and well established measuring procedure, and can be beneficial for calorimetry development and nuclear medicine instrumentation.

1.4 Thesis Outline

The thesis is structured as the following:

- Chapter 2 provides an introduction to the physics background of positron emission tomography. Basic concepts of the imaging technique and requirements for the detector are discussed;
- Chapter 3 describes the specific details of the EndoTOFPET-US project from which most of the work in this thesis is motivated and funded;
- Chapter 4 presents a Monte Carlo simulation for the single channel of the proposed PET detector. The simulation tool shows its valuable prediction capability in the design phase of the new detector;
- Chapter 5 gives a brief overview of different photodetector technologies and introduces the silicon photomultiplier. Its working principle and figures of merit are explained.
- Chapter 6 describes the method developed to characterize the SiPM. Through the discussion of the experiment methods and their results, a deeper understanding in the operation of the SiPM is provided;
- Chapter 7 introduces an alternative flavor of the SiPM, namely the digital SiPM. As a relatively new technology the digital SiPM shows great potential in the application of nuclear medicine and is adopted in the EndoTOFPET-US project. Its unique working mode and the test of a prototype device is described;
- Chapter 8 describes the characterization techniques developed in this thesis being applied on an analysis of the radiation hardness of the SiPM. As a promising photodetector candidate for high energy physics and astronomy physics applications, the radiation hardness study of the device is an important requirement;
- Chapter 9 provides the conclusion.

Chapter 2

PRINCIPLE OF PET

Positron Emission Tomography provides metabolic information by imaging gammas emitted within the body. An adequate pharmaceutical compound labeled with a positron-emitting radionuclide is administered to the patient as the source for the production of positrons. A Certain amount of time is required for the injected pharmaceutical to be absorbed throughout the body.

This chapter is organized as following. First, the physics background involved in PET imaging and the time-of-flight PET technique are described. Then the physics concerning scintillation light detection is introduced.

2.1 Positron Emission

In proton-rich nuclei, a proton can decay (weak interaction mediated) to a neutron, a positron and a neutrino via the process:



which is known as β^+ decay. This process cannot happen to free, isolated protons due to energy constrains. β^+ decay can only happen inside nuclei when the daughter nucleus has a greater binding energy than the mother nucleus. Examples of isotopes which undergo β^+ decay are shown in Table 2.1, the table is readapted from [9].

Tab. 2.1: Commonly used positron emitting isotopes in PET, the positron range is given in Full-width-half-maximum (FWHM).

Isotope	Half-life [min]	Positron range in water [mm]
^{11}C	20.3	1.1
^{13}N	9.97	1.4
^{15}O	2.07	1.5
^{18}F	109.7	1.0

The emitted positron can loose its kinetic energy by Coulomb interactions with electrons and follows a tortuous path until it reaches approximately its thermal energy. Then the positron annihilates with an electron. The annihilation between positron and electron can happen directly or through a transition stage, where the positron-electron pair forms a quasi-stable system called positronium and then decays into two or three photons. With a probability of $\sim 99\%$ [10] the annihilation produces a pair of photons (gamma)

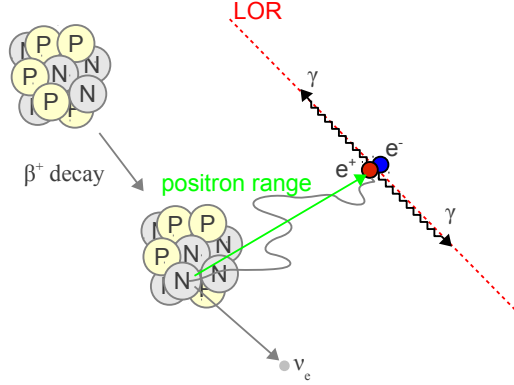


Fig. 2.1: Scheme shows the positron emission from a β^+ decay and its annihilation with an electron, and the definition of positron range and Line-Of-Response (LOR).

with a characteristic energy of 511 keV each, moving in opposite directions. This is the result of energy and momentum conservation. Both positron and electron have rest masses of 511 keV.

A PET scanner simultaneously (within a coincidence window of nanosecond range) detects the two anti-parallel annihilation gamma with two opposing detector sections, and forms a Line-Of-Response (LOR) which contains information of the annihilation position. A set of LORs detected by the PET scanner is then used to reconstruct the positron emission occurring place.

The distance from the emission point of the positron to the annihilation point is known as the positron range (shown in Fig. 2.1). It depends both on the energy of the emitted positron and the surrounding materials. The positron range produces an inherent error to the data collected by PET scanners and can not be corrected, therefore it is one of the limiting factors to the spatial resolution in PET. It is worth noting that the total momentum of the annihilating positron and electron may not be zero, this variation creates an angular uncertainty of around 0.2° to the 180° angle between the two 511 keV gamma [9], that is also an inherent positional inaccuracy in PET.

2.2 Photon Interactions with Matter

When photons pass through matter, they mainly interact via three processes: Compton effect, photoelectric effect and pair production. A photon beam of initial intensity I_0 after traversing a thickness x of a material will have a residual intensity I of unaffected primary photons equal to:

$$I = I_0 e^{-\sigma x} e^{-\tau x} e^{-\kappa x} \quad (2.2)$$

$$= I_0 e^{-(\sigma + \tau + \kappa)x} \quad (2.3)$$

$$= I_0 e^{-\mu_0 x} \quad (2.4)$$

where the quantity

$$\mu_0 = \sigma + \tau + \kappa \quad (2.5)$$

is the total linear attenuation coefficient. σ , τ , κ are the linear attenuation coefficients for the Compton effect, the photoelectric effect, and the pair-production respectively. The total linear attenuation coefficient

is a measure of the number of primary photons which have interactions. Fig. 2.2 shows the relative importance of the three major types of interactions as a function of the photon energy ($h\nu$, h is the Planck's constant and ν is the photon frequency) and material's atomic number Z [10].

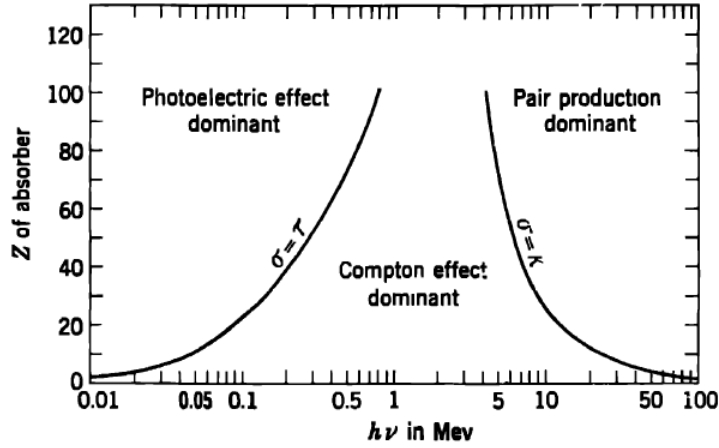


Fig. 2.2: Relative importance of the three major types of photon interactions. The lines show the values of Z and $h\nu$ for which two neighboring effects are just equal. [10]

The Photoelectric and Compton effect are the most relevant interactions for the 511 keV photons, whereas pair-production can be neglected. The three types of interactions and their relevance to PET imaging are summarized below.

2.2.1 Photoelectric Effect

In the photoelectric effect, the incident photon with energy E_γ is absorbed by an atom and in the process an electron is ejected from one of its bound shells with the kinetic energy E_{e^-} :

$$E_{e^-} = E_\gamma - E_b \quad (2.6)$$

where E_b is the binding energy of the ejected electron. Due to energy conservation, photoelectric effect can only take place if the energy of the photon exceeds the binding energy of the electron, typically a few tens of electron volt. The resulting hole left by the photo-electron leaving the atom can be filled by another orbital electron from outer shells and subsequently emits characteristic x-rays, or by an Auger electron. In the latter case, the surplus energy of outer electrons filling an inner vacancy is given to another orbital electron, resulting in the ejection of an Auger electron.

The probability of photoelectric effect occurring is measured by the cross section of interaction, which scales with the atomic number of the material by $Z^4 \sim Z^5$ and decreases rapidly with increasing photon energy [10]. The effective atomic number for water is 7.4, and the human body can be approximated fairly well by water. The probability of photoelectric absorption for 511 keV photons in water is negligible [11]. Therefore most gammas emitted by positron-electron annihilation can exit the human body without being absorbed. On the other hand, in order to detect the 511 keV photon, PET detectors use scintillating crystals with high atomic number to maximize the probability of photoelectric absorption, so that the incident gamma can deposit all its energy in the detector volume and hence be successfully detected. The inorganic crystals normally used in PET ranging from 33 for sodium iodide (NaI) up to 66 for the cerium-doped Lutetium-Yttrium Oxyorthosilicate (LYSO) nomenclatureLYSOcerium-doped Lutetium-Yttrium Oxyorthosilicate.

2.2.2 Compton Effect

The Compton effect is the inelastic scattering of photons by weakly bound or free electrons. The electrons are considered free if the energy of the photons is high with respect to the binding energy of the electrons. [10].

The incident photon with energy $E_\gamma = h\nu$ is deflected from its incident direction by an angle θ . The scattered photon has a smaller energy $E'_\gamma = h\nu'$, and the struck electron recoils at an angle ϕ with a kinetic energy of E_{e^-} . Using the momentum and energy conservation in two-body collision, the energy of the scattered photon and the energy transferred to the struck electron (E_{e^-}) is given by

$$E'_\gamma = \frac{E_\gamma}{1 + \varepsilon(1 - \cos\theta)} \quad (2.7)$$

$$E_{e^-} = \frac{E_\gamma \cdot \varepsilon(1 - \cos\theta)}{\varepsilon(1 - \cos\theta) + 1} \quad (2.8)$$

in which $\varepsilon = E_\gamma/m_e c^2$ is the ratio between the incident photon's energy and the rest mass of the electron ($m_e c^2$). The maximum energy transfer happens when the scattering angle of the incident photon is 180° :

$$E_{e^-}^{\max} = \frac{2\varepsilon \cdot E_\gamma}{2\varepsilon + 1} \quad (2.9)$$

which for the 511 keV photon, $\varepsilon = 1$:

$$E_{e^-}^{\max} = \frac{2}{3}E_\gamma \quad (2.10)$$

When elastic scattering occurs, photons are scattered by tightly bound atomic electrons without producing atomic excitation or ionization. This is known as Rayleigh scattering. Rayleigh scattering is more probable than Compton scattering for photons at low energies (<100 keV). Since the scattering angles are small and the change to photon's energy after scattering is negligible, the Rayleigh scattering does not have practical impact on PET.

On the other hand, the Compton effect is a major concern in PET. The impact of Compton scattering can be considered in two aspects.

Scattered Coincidence

A 511 keV photon emitted from positron-electron annihilation may undergo a Compton scattering process in the surrounding tissues and changes its direction. If the scattered photon is then detected by the PET detector and interpreted in a coincidence event, a false LOR will be formed. This is called a scattered coincidence event compared with a true coincidence event in which both gammas reach the detector system without any interactions as shown in Fig. 2.3. Scattered coincidence events give false position information and add noise to the image, which in turn decrease the image contrast.

It is possible to discriminate the scattered photon using an energy threshold in the detector. Known from Eq. 2.7, the scattered photon has an energy E'_γ and $\frac{1}{3}E_\gamma \leq E'_\gamma < E_\gamma$. The effectiveness of the method relies on the energy resolution of the detector system. Additionally, studies [12, 13] show that it is possible to use image reconstruction algorithms and the time-of-flight information of the detected gamma to identify and correct scattered coincidence events.

Compton Scattering in Detector

The Compton scattering of gammas occurs in the detector volume may lead to partial energy detection, result in a 511 keV gamma not successfully registered by the detector. Fig. 2.4 shows the principle response of a finite size scintillation detector to 511 keV photon. Photons that undergo photoelectric process will

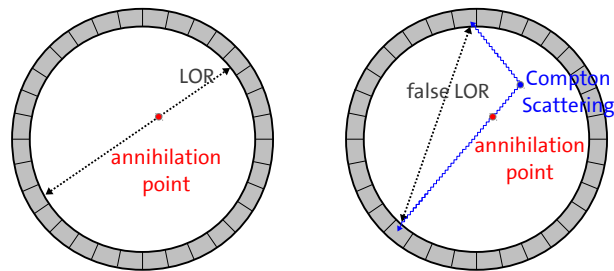


Fig. 2.3: The left drawing shows a true coincidence event, in which two gammas reach the detector system without any interactions. The right drawing shows a scattered event, one gamma undergoes a Compton scattering prior to the detection, a false LOR is formed by the detector.

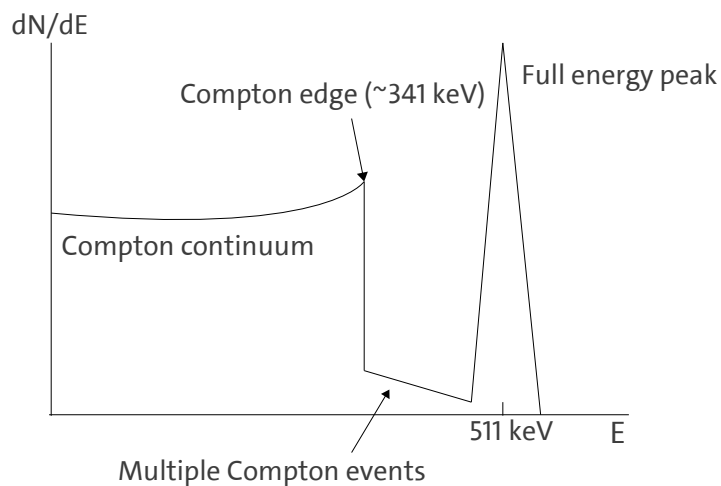


Fig. 2.4: The principle scintillation detector response to 511 keV gamma

deposit all their energy in the detector and form the 511 keV photo-peak. The Compton scattering of the photons in the detector volume result in an electron with kinetic energy E_{e^-} , according to Eq. 2.10 $E_{e^-} < \frac{2}{3}E_\gamma$. The struck electron deposits its energy in the scintillator by ionization and detected by the detector, forms the Compton continuum. The Compton edge corresponds to the maximum kinetic energy a 511 keV photon can transfer to the struck electron in a Compton scattering process. However, the scattered photon can further undergo Compton scattering or photoelectric absorption and thus contributes to the events fall between the Compton edge and the 511 keV photo-peak or the 511 keV photo-peak. Therefore the 511 keV photo-peak is also called full energy peak which is formed by both photoelectric events and multiple Compton events. The probability of multiple Compton events occurring within the same scintillator depends on the volume size of the scintillator.

The conventional PET detector uses an energy threshold (normally above the Compton edge of 340 keV) for the detected events to discriminate the 511 keV gamma from an annihilation event. Therefore the efficiency in the detection of 511 keV gammas, which is the ratio between the number of gammas with full energy deposited in the detector volume and the total number of gammas enters the detector volume, has great impact on the sensitivity of a PET scan. The sensitivity is defined as the ratio between the number of detected coincidence pairs to the total number of emitted photon pairs. It depends not only on the detection efficiency of single detector sections but also on the total solid angle coverage of the PET system. Detector sensitivity is a key parameter to a PET system. Higher sensitivity means accumulating more statistics within the same scan time for the image reconstruction and thus can have an improved image quality. Alternatively, the dose of radioactivity injected to the patient can be reduced without compromising the image quality.

Nevertheless, for the 511 keV photons, the probability of occurrence of photoelectric effect in the first interaction with the scintillator used in medical imaging is usually no more than 50% [14]. Using larger size scintillators may mitigate this effect by increasing the probability of multiple Compton process that result in full energy deposition of the 511 keV photon. However, the increase in scintillator's size may reduce the intrinsic detector spacial resolution which also affects the image quality. Studies in [15, 16, 17, 18] show that it is possible to identify and utilize detector Compton scattering events to increase the detector sensitivity by coherently combining data from multiple neighboring detector sections.

2.2.3 Pair-Production

Photons with energy above 1.022 MeV can create a positron-electron pair in the presence of a nucleus. Additional energy from the photon is converted into kinetic energy of the created electron and positron. This process is known as pair-production. Energy conservation requires the energy of the photon to cause pair-production must exceed the sum of a positron and an electron's rest mass (2×511 keV), and a nucleus as collision partner is necessary for momentum conservation. Gamma photons produced in a PET scan have too low energy (511 keV) for this process to occur.

2.3 Time-of-Flight PET

The concept of Time-Of-Flight (TOF) PET is to measure the precise time that each of the annihilation emitted photons is detected and calculate the difference. The difference in the arrival time between the two photons helps localize the annihilation point along the LOR.

Strictly speaking, the conventional PET scanner uses the time-of-flight information of the detected photons as well. The detected photons are tagged with a detection time. If the detection time is smaller than a set coincidence window, they are considered as correlated to the same annihilation event and therefore are used to form a LOR for the image reconstruction. The set coincidence window time directly relates to the time-of-flight difference of the photon pair, blurred by measurement uncertainty (time resolution of the detector). For conventional PET scanners, the coincidence window is usually in the range of several nanoseconds.

However, the time information is no longer considered in conventional PET once the photon pair is identified. The emission point and the distribution of radioisotopes are reconstructed by analytical or interactive reconstruction algorithms on the acquired sets of LORs. During image reconstruction, an equal probability along the LOR is assumed while in TOF PET, the emission point of the photon pair can be further localized using the TOF information.

As shown in Fig 2.5, the time-of-flight difference (t) between the two photons emitted by an annihilation relates to the distance (x) of the emission point from the center of the LOR.

$$x = \frac{c \cdot t}{2} \quad (2.11)$$

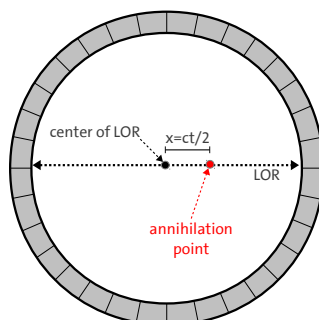


Fig. 2.5: The scheme shows how the time-of-flight different (t) between the photon pair relates to the distance (x) between the annihilation point and the center of the LOR.

where c is the speed of light. Hypothetically, if t is exactly measured by the detector, no image reconstruction algorithm is needed at all—for every LOR, the annihilation point can be determined by Eq. 2.11, and the distribution of the radioisotopes can be obtained by plotting all the annihilation points. In reality, t is measured with an uncertainty (Δt) that is limited by the coincidence time resolution (CTR) of the PET scanner. Hence, the uncertainty on the localization of the annihilation position is given by

$$\Delta x = \frac{c \cdot \Delta t}{2} \quad (2.12)$$

which makes the coincidence time resolution an important parameter in the localization of the emission point. Therefore the CTR becomes a more important figure of merit for a TOF PET imaging system than for conventional PET systems.

The CTR of a PET system is given by summing the single time resolution (STR) of the two opposing detector sections in quadrature, where the STR of a single detector section depends on its scintillator and photodetector properties as well as the time resolving ability of the readout electronics. Since in most cases, a PET scanner consists of a ring of identical detector sections with very similar performance, the CTR of the system can be very well estimated by

$$\text{CTR} = \sqrt{2} \cdot \text{STR} \quad (2.13)$$

where STR is the time resolution of a single section in the detector ring.

Random Coincidence

The time resolution of the detector system concerns PET in another aspect, the reduction of random coincident events.

Fig 2.6 shows the scheme of such an event. If gammas from different independently occurred annihilation events were detected by different detector sections within the same coincidence window, their origins can not be discriminated. Therefore they will be interpreted as if a single annihilation event occurred on the false LOR. Such events cause isotope's concentrations wrongly measured if not corrected for. Random coincidences also add statistical noise to the data. Both cases end up in the blurring of the reconstructed image.

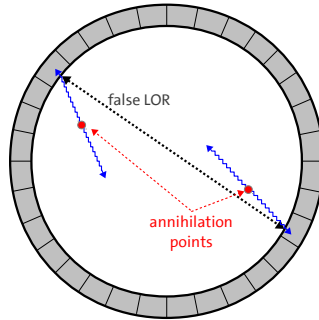


Fig. 2.6: Scheme of a random coincident event.

The number of random coincidences directly links to the radioactivity of the object being imaged and the time width of the set coincidence window. Detector system with higher time resolution allows the use of a smaller coincidence window. It should be pointed out that a conventional ring PET has a field of view of about 1 m in diameter, which means about 3 ns of transversing time for the photon. The detector should have a coincidence window larger than this time in order to be able to detect the true coincidence event. The motivation for increasing the time resolution of the system is mainly focused on using the TOF information to reduce the noise. However, for PET applications focused on smaller area, higher time resolving capability can help to reject random coincident events which occur out of the region of interest. According to Eq. 2.12, a coincidence time resolution of order 200 ps can help rejecting events outside a region of 3 cm.

2.4 Scintillation Detector

The scintillation detector is the key component to any PET system. The energy and time resolution as well as the sensitivity of the detector primarily define the performance of the system. Despite variations in the design, the principle of a scintillation detector is to generate an electrical signal proportional to the energy of the particle to be detected. Essentially, a scintillation detector consists of three components, a scintillator which absorbs the incoming particle and converts its energy into scintillation light, a photodetector which measures the light intensity and produces proportional electrical signals and the electronics that further process the signal so that the information can be correctly stored and analyzed later. In addition, front-end and back-end electronics are needed to control and monitor the detector parameters.

2.4.1 Scintillator

Scintillators have a long history of development for experiments in nuclear physics, high energy physics and nuclear medicine. They are widely used in various detector systems such as trigger systems, calorimeters, PET detectors or CT detectors. Their principle is to absorb the energy of the incident particle or radiation and re-emit the energy in the form of scintillation light in the visible or ultraviolet wavelength range (100 ~ 800 nm). A scintillator can be in any of the gaseous, liquid or solid phase depending on the application. Generally, scintillators can be categorized as organic and inorganic scintillators.

The organic scintillators are usually aromatic hydrocarbon compounds containing linked or condensed benzene-ring structures [19]. They have very rapid decay time in the order of few nanoseconds or less therefore provide excellent timing properties. However, because of their relative low density range between 1.0 to 1.5 g/cm^3 [20], particles and high energy radiations are usually not stopped by an organic scintillator. Therefore they are typically used in trigger systems where fast timing is required or sampling calorimeters in which not total energy of the particle (or particle shower) is measured. For PET applications, solid high density inorganic crystals are typically used.

Inorganic Scintillator

The inorganic scintillators are mainly crystals grown in high temperature furnaces, often with a small amount of activator dopant. The scintillation mechanism in inorganic scintillators is linked to the characteristic of the energy band structure found in crystals as shown in Fig. 2.7.

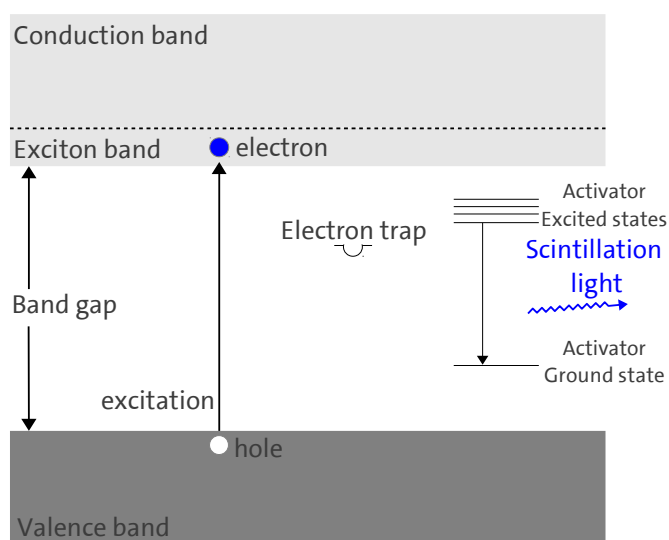


Fig. 2.7: Energy band structure of inorganic crystals.

A photon loses its energy due to photoelectric effect or Compton effect. The loss of energy by the incident photon can excite an electron from the valence band to the conduction band and create a free electron and a free hole. The free electron and hole then are thermalized by intraband transitions and lattice scattering. Also a loosely coupled electron-hole pair can be created by the excitation of an electron to an exciton band that is below the conduction band. All those free electrons, holes and coupled electron-hole pairs will move through the crystal lattice until they are captured by a luminescent center and excite an activator. The excited luminescent centers return to the ground state by emitting scintillation light. Since the emitted light has energy in the order of 2~3 eV, which is lower than the threshold to ionize the crystal ($O(10\text{ eV})$), the crystal becomes transparent to the scintillation light so that they can be detected by

photodetectors. The intrinsic rise time of the scintillation light depends on the detailed excitation processes of the luminescent centers [21], while the de-excitation of the luminescent centers determines the fast component in the decay time. Electron-hole pairs may also be trapped and recombine later, result in the slow component in the scintillation light. Also, the quenching effect may occur, in which case the de-excitation of the activators result in heat rather than the emission of scintillation light.

Inorganic scintillators normally have high atomic number to enhance the photoelectric interaction contribution and high density to increase the interaction efficiency. The attenuation length for 511 keV of the material, which is the distance where the intensity of the beam has dropped to $1/e$ is used to characterize its efficiency in stopping the photons. The number of emitted scintillation photons per unit absorbed energy by the scintillator is called light yield. Higher light yield of scintillators implies higher number of detected photons (N_{ph}), which is normally desirable from PET applications. Because the number of detected photons is governed by Poisson statistics, the standard error of the counting result is $\sqrt{N_{ph}}$.

Associated with the light yield requirement, a scintillator is normally prepared for a high light collection efficiency. Reflectors are used to wrap the crystal leaving only the side where photodetector is attached, so the light that otherwise would escape the crystal can be recaptured. An optical coupling compound with matching refractive index is normally used to fill the gap between the crystal and the photodetector, therefore total inner reflections can be avoided on the exit surface of the crystal.

A scintillator's rise time, decay time and light yield are associated to the intrinsic time resolution of the detector system. The probability density function (PDF) $f(t)$ of the scintillation light at time t is given by a bi-exponential function [22, 23]:

$$f(t) = \frac{e^{-t/\tau_d} - e^{-t/\tau_r}}{\tau_d - \tau_r} \quad (2.14)$$

where τ_r and τ_d are the rise and decay time of the crystal. Fast rise time allows a short coincidence window in PET, thus reduce the random coincidence events in the data. A fast decay time allows photodetectors to use faster readout data rate, this is more important in 3D PET applications [24] where the detector covers full (or a large part of) solid angle and the sensitivity of the detector is dramatically increased. In this case, slow decay time of the scintillation light may result in pile-up effect of the detector. The fast rise and decay time together with the high light yield indicate a fast initial light emission rate, which helps in improving the intrinsic time resolution of the crystal. The actual time resolution of the detector system also strongly depends on the temporal properties of the photodetector and readout electronics which will be discussed later.

Tab. 2.2: Properties of inorganic scintillation crystals used in PET detectors

	NaI(Tl)	BGO	LYSO:Ce	LSO:Ce(0.4Ca)
Density [g/cm ³]	3.67	7.13	7.4	7.4
Peak Emission Wavelength [nm]	410	480	420	420
Refractive Index	1.85	2.15	1.82	1.82
Attenuation Length for 511 keV[cm]	3.0	1.1	1.2	1.2
Light Yield [ph/keV]	38	7.2	30	34.8
Rise Time [ps]	-	-	100	100
Decay time [ns]	230	300	40	31

Sodium Iodine activated with Thallium, NaI(Tl), was initially used in the PET detector because of its high light yield of 38 photons per keV deposited energy (ph/keV) and also cost effectiveness. However, it

has slow decay time (~ 230 ns) that result in poor time resolution of the detector. Also, the low density is not efficient in stopping 511 keV gammas. In order to increase the sensitivity, thick NaI crystals are normally used, which results in worsening the spacial resolution. Bismuth germanate (BGO) was used to replace NaI as it has high atomic number and therefore high detection efficiency. However it is also slow in decay time and has a poor light yield. LSO (Lutetium orthosilicate) and LYSO (Cerium-doped Lutetium Yttrium Oxyorthosilicate) are the most favorable scintillators in recent PET detector development, they are high density material provide high light output as well as quick rise and decay time. Several most commonly used inorganic scintillation crystals and their important properties are listed in Tab. 2.2. Note that depending on the doping concentration and production process, performance of the crystals may vary for different producers. Numbers are taken and readapted from [25, 26, 27].

2.4.2 Photodetectors

Scintillation light emitted from the scintillator is then converted to electronic signal that is extracted for energy and time information. The most commonly used photodetectors for PET system is the photomultiplier tube (PMT). The rapid development of solid-state detectors has provided some promising candidates such as avalanche photodiode (APD) and silicon photomultiplier (SiPM). However, they are mostly used in prototype development or lab research while PMT appears in almost all commercial PET systems. This section will give a brief introduction to PMT and discuss the key parameters that define the performance of a PET system. The detail of the SiPM is discussed in Chapter 5.

A photomultiplier tube is typically constructed from glass vacuum tubes which encapsulates a photocathode, a focusing electrode, several dynodes and an anode. The series of dynodes are connected to the negative high voltage, at 1000~2000 V, using a resistor array so that a potential gradient between the dynodes is formed until the anode. Fig 2.8 shows the construction of a photomultiplier tube. Incident

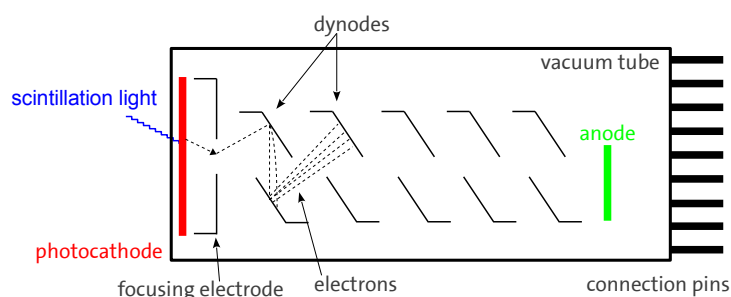


Fig. 2.8: The construction of a photomultiplier tube.

photon enters the front window of the vacuum tube and strikes the photocathode which is usually a layer of photosensitive compound coating on glass. If the photon's energy is higher than the work function of the material, a free electron can be released from the surface by photoelectric effect. Work function of a material is the minimum energy needed to remove an electron from a solid to a point in vacuum immediately outside the solid surface, it approximately equals to the sum of band gap energy between

the valence band and conduction band and the electron affinity. Photosensitive compound such as alkali metals or semiconductors has a small work function, so they are sensitive to low energy photons in blue or ultraviolet range. The emitted electron, normally called photoelectron, is then accelerated and focused by the focusing electrode on to the first dynode. The accelerated photoelectron gains enough energy (100~200 eV) to kick out further electrons from the dynode material through impact ionization. This is called secondary electron emission. Those secondary electrons are subsequently accelerated by electric field between the dynodes and multiplied at each dynode. By repeating the process for n times, and assuming the average secondary emission ratio is p , the photoelectron signal is amplified by a factor of p^n when it finally collected by the anode. This is the gain (G) of the PMT.

$$G = p^n \quad (2.15)$$

Modern PMTs with more than 10 dynodes can have a gain from 10^6 up to 10^8 . Therefore PMT can provide a robust and measurable electrical signal for very low intensity light down to single photon region.

Excess Noise Factor

The Excess Noise Factor (ENF) is usually used to describe the statistical fluctuation of the PMT gain. It is defined as the ratio between the output and input signal variation (σ_{out} and σ_{in}) if use the PMT to detect a Gaussian distributed light signal.

$$ENF = \frac{\sigma_{out}}{\sigma_{in}} = 1 + \frac{\sigma_G^2}{G^2} \quad (2.16)$$

where σ_G^2 is the variance of the PMT's gain. Typical ENF of a PMT is between 1.2 to 2. The ENF determines the photon counting capability of a PMT and high ENF also worsen the energy resolution of the PMT.

Dark Current

Dark current is the current output of a PMT even when it is operated in total darkness. The main component of dark current is the charge sum of several short pulses which are similar to the photoelectron pulses when doing photon counting, they are caused by the thermionic emission of single electrons from the photocathode. Hence, the rate of these pulses are also called dark count rate. Typical dark count rate of PMTs are in the order of 100 ~1000 Hz.

Dark counts may influence the time resolution and signal-to-noise ratio of a PET system. In order to get the best timing, a signal discriminator is usually used to provide trigger for the coincidence window. Better time resolution can be achieved by using lowest threshold level so that the jitter on the signal is minimized [28]. However, high dark count rate PMT has many random pulses that result in false triggering and worsening the time resolution. False triggers also increase the probability of random coincidence therefore reduce the signal-to-noise ratio in the collected data.

Afterpulses

Afterpulses of PMT are the pulses observed in the wake of true signals. They are time correlated with true pulses that triggered by the incident light. The cause of an afterpulse in PMT is either elastic scattering of electrons from the first dynode or the ionization of residual gases in the tube [29]. Therefore afterpulsing probability increases with the PMT gain. Afterpulses are potential noise source in low intensity photon counting experiments. Concerning PET detectors, after-pulses of a PMT can limit the data rate of a high sensitivity system and cause random coincident events.

Photon Detection Efficiency

The ratio between the number of emitted photoelectrons from photocathode to the number of incident photons is called quantum efficiency of the PMT, it is normally expressed as a percent. The probability that the photoelectrons emitted from the photocathode (primary electrons) will impinge on the first dynode and contribute to gain is referred to as collection efficiency [29]. The photon detection efficiency (PDE) of a PMT is then defined as

$$\text{PDE} = \text{QE} \times \text{CE} \quad (2.17)$$

where QE is the quantum efficiency of the photocathode and CE is the collection efficiency of the dynodes. The quantum efficiency depends on the material of the photocathode and is a function of the photon wavelength. The collection efficiency depends on the electric field between the cathode and the first dynodes as well as the structure design of the photomultiplier tube. Modern high efficiency photomultiplier tubes can provide up to 35% photon detection efficiency [30].

The quantum efficiency of a photocathode, therefore the PDE of the PMT, has wavelength dependence on the incident photon, which is called spectral sensitivity. At long wavelength, the work function of the photocathode material and its thickness determines the sensitivity and photo-emission threshold. While at the shorter wavelength, it more relates to the input window's transmission.

PDE of a detector has great impact on both energy and time resolution of a PET system. As discussed in section 2.4.1, the energy resolution is a function of the number of detected photons (N_{ph}), in which N_{ph} is the number of photons impinging on the detector sensitive area times the photon detection efficiency. Therefore the energy resolution (σ_E/E) given by a PMT can be described by

$$\frac{\sigma_E}{E} = \sqrt{\frac{\text{ENF}}{N_{ph}} + \left(\frac{\text{ENC}}{N_{ph} \cdot G}\right)^2} \quad (2.18)$$

where ENF is the excess noise factor of the PMT, ENC is the equivalent noise charge of the PMT. [28] also shows the measured time resolution of the scintillation detectors for PET system has a linear dependence on $1/\sqrt{N_{ph}}$.

Time resolution

A single photoelectron generated by the photocathode are multiplied by the series of dynodes and result in a pulse charge output at the anode, which is called single-photoelectron response (SER) of the PMT. The electron transit time which describes the delay from the photon hitting the cathode to the generation of a output signal is determined by the design of the PMT's structure. The width of the SER pulse is determined by the intrinsic capacitance of the PMT. Photomultiplier tubes designed for a fast timing property using optimized geometry to minimize the electron transit time, while the long distance between the cathode and anode helps in reducing the intrinsic capacitance of the PMT. [29] shows the pulse width and electron transit time of PMT can be lower than 2 ns and 5 ns respectively. The pulse width and electron transit time are in inverse proportion to the square root of the supply voltage.

However, when multiple photons hit the photocathode generating multiple photoelectrons, due to the random nature the the process, there is a fluctuation in the generation time as well as a transit time of each photoelectron. Therefore the output signal is a convolution between every SER pulse with a spread in time described as transit time spread (σ_{ts}). The transit time spread primarily determines the intrinsic time resolution of a PMT. The transit time spread is in inverse proportion to the square root of the supply voltage as well. It is also inversely proportional to the total number of photoelectrons generated [29]. The measured transit time spread at single photon level is normally in the order of several hundred picoseconds. Therefore in order to achieve the best time resolution for a PET system using PMT readout, it is important to maximize the scintillating crystal's light yield and the quantum efficiency of the PMT so that the

number of generated photoelectrons for each 511 keV photon is maximum thus the transit time spread is minimized.

Linearity

In general, the PMT exhibits good linearity over a wide range of incident light intensity, from single photon up to 10^6 photoelectrons. In other words, it offers a wide dynamic range [29]. This is important because deviation from linear response will deteriorate the energy resolution. However, PMTs used in PET system do not have this concern since the scintillation light expected from 511 keV gamma hitting an inorganic crystal is in the order of 10^4 photons. Only at very high radiation level, such as in high energy physics experiments, huge number of photoelectrons creates a large current flowing in the dynodes can cause space charge effect and saturate the current.

2.4.3 Readout Electronics

Readout electronics is required to extract the energy and time information from the output signal of the photodetector. A photodetector, e.g. PMT or SiPM, outputs a current (charge) signal. The signal is extracted by the preamplifier and is fed to a signal shaper or amplifier to output a voltage pulse signal with low distortion. The time information of the signal is normally extracted by using a signal discriminator followed by the time-to-digital converter (TDC), while the energy information which is proportional to the signal's amplitude or area is collected by a signal digitizer. For these purposes, ASIC (Application-Specific Integrated Circuit) chips dedicated to a specific detector system design are the optimum solutions. They can provide the optimized performance in noise suppression and power consumption. The compactness of the ASIC chips is also ideal for detector integration.

In addition, the FPGA (Field Programmable Gate Array) serves to program the chips and acts as an interface between the photodetector readout electronics and the data acquisition (DAQ) system. And power sources are necessary to drive the photodetectors and pulse generators generate clocks to synchronize between different electronic equipments.

Signal Readout

The extraction of the signal from the photodetector can be made using charge sensitive readout or voltage sensitive readout. In the former case, a charge sensitive preamplifier is connected to the output of the photodetector. Fig. 2.9 shows the principle schematic of a charge sensitive preamplifier connected to a photodetector which is represented as a capacitor with capacitance C_{det} providing an output charge of Q_{det} [31]. The charge sensitive preamplifier integrates the input charge on a feedback capacitor with capacitance of C_{fb} and output a voltage pulse with an amplitude of V_{out} , where

$$V_{out} = \frac{Q_{det}}{C_{fb}} \quad (2.19)$$

Therefore the voltage output of the charge sensitive preamplifier is proportional to the detector's output charge, the rise time of the signal approximately equals to the width of the current pulse from the detector and the decay time of the signal $\tau_f = R_{fb} \cdot C_{fb}$. The effective input capacitance of the preamplifier is $C_{eff} = (A + 1)C_{fb} + C_{in}$, where A is the amplification factor of the preamplifier and C_{in} is the capacitive load to ground at the input stage of the preamplifier. The value of effective input capacitance should be sufficiently higher than the detector capacitance i.e. the input impedance of the preamplifier is very low. Thus the charge output of the photodetector can be totally transferred to the preamplifier. Otherwise, charge loss or cross talk between connected photodetectors may happen.

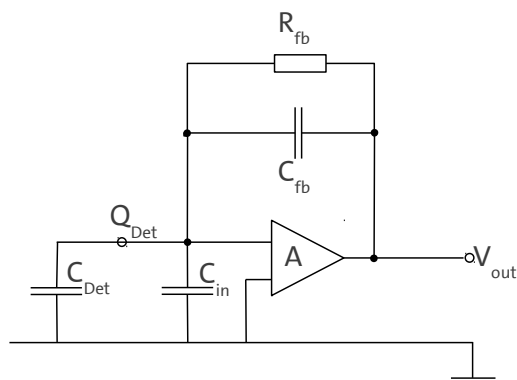


Fig. 2.9: Schematic of using the charge sensitive preamplifier readout a photodetector.

The detector output current can also be read out through a resistor, the voltage drop on the readout resistor is fed to a voltage amplifier. In this case, the output signal's amplitude is no longer proportional to the detector output charge. However, the low resistance of the readout resistor, typically $50\ \Omega$, helps to preserve the the charge output of the detector. Therefore the charge information can be obtained by integrating the output signal.

In PET, both the energy and time information of the output signal are needed for the image reconstruction. The energy information is used to separate Compton events from the $511\ \text{keV}$ gamma and is normally obtained by measuring the charge or amplitude of the output signal. A charge-to-digital converter (QDC) can directly integrate a signal within a predefined integration interval (gate) while a peak-sensing analog-to-digital converter (ADC) samples voltage after a charge to voltage amplifier and determines the maximum amplitude of the signal within the inspect interval. Both devices convert electrical signals to digital numbers in arbitrary units which can be stored and processed later. Note that all electronic devices used to process the output signal of the photodetector introduce electrical noise to the original signal, the effect can be seen as the original signal is convoluted with a series of noise signals generated by the different electronic components during signal processing.

The time information is used to determine the time of flight of the detected gammas. The simple way of measuring the occurrence of a signal is to use a leading-edge discriminator to generate a trigger pulse as the signal crosses a given threshold. The trigger pulse will start or stop the time-to-digital converter which constantly counting a high frequency system clock. Thus the time at which the signal crosses the threshold can be recorded. The usage of the discrimination method to determine the rise time can provide the best time estimation of the detected event with low uncertainty. However, the time-walk effect, in which the signal pulses with different amplitudes cross a fixed threshold level with a time shift (from t_1 to t_2 in Fig. 2.10), increases the uncertainty of the measurement. The constant fraction discriminator (CFD) can be used to solve this problem since signals with similar shapes but varying amplitudes cross the same fraction of their amplitudes at the same time [32] (c.f. Fig. 2.10).

The leading edge discrimination is suitable for small amplitude signals with fast rise time such as single photon counting experiments because the jitter associated with the signal discrimination procedure is minimum. The CFD method is used in cases where the signal of the photodetector has broad distribution in amplitude such as reading out scintillation light. However, the additional circuitry used for constant fraction discrimination introduces jitters and worsen the time resolution of the system.

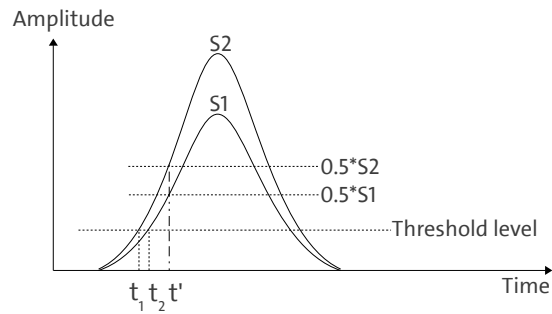


Fig. 2.10: The time-walk effect when using leading edge discrimination. The threshold cross time “walks” from t_1 to t_2 when using a fixed threshold level because the amplitude of the two signals are different. However they cross half of their amplitude level at the same time t' .

The Time-over-Threshold Technique

The Time-over-Threshold (ToT) technique measures the pulse width to estimate the amplitude of the signal. In this way, it transforms the amplitude (or charge) measurements to time measurement. The estimation of energy using pulse width is less precise than the charge integration measurement. However, the detector system design can be simplified by using only TDC for both energy and time readout. Therefore, the ToT technique is suitable for TOF PET since the energy resolution required to separate photoelectric events from Compton scattering events is moderate (normally better than 20% in FWHM) while the timing precision is crucial in improving the overall performance of the system.

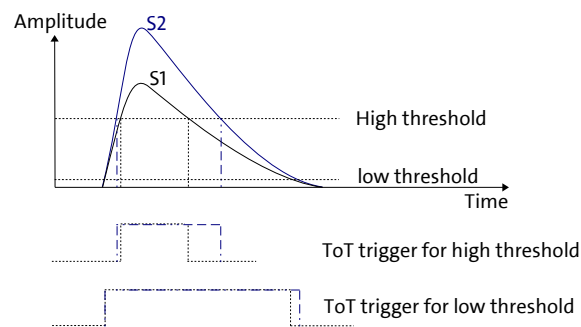


Fig. 2.11: The principle of time-over-threshold technique. The width of the pulse above the threshold level is correlated to the amplitude of the pulse.

The ToT technique uses an amplitude threshold and counting the time difference between the leading and trailing edge of a pulse crossing the threshold. As shown in Fig. 2.11, the amplitude of the pulse is correlated to the time over threshold, i.e. the triggered width. Such that the energy information provided by a signal is encoded into the width of the output ToT trigger. The signal with larger amplitude has longer ToT trigger width.

The energy resolution of the ToT technique depends on the signal’s pulse shape as well as the

triggering threshold. Fig. 2.11 shows the ToT trigger width for two signals with similar shapes but different amplitudes. The difference in trigger width of the two signals is better resolved for a higher triggering threshold. Thus, one can get a better energy resolution with higher triggering threshold. However, in order to improve the time resolution of the system, the triggering threshold for TDC should be set as low as possible [22]. Therefore a general solution when using the ToT technique for both energy and timing measurements is to use two different thresholds. The original signal is duplicated and processed independently by two signal discriminators with different threshold optimized for the time and energy resolution respectively [33]. [34] uses another method to solve the problem by using a capacitor to integrate the the signal if the higher threshold is exceeded. Then, the capacitor slowly discharges in small constant current. In this way, the time over threshold of a pulse signal is stretched, and the stretched ToT width is partially proportional to the charge of the signal. Therefore, using the lower threshold value can obtain both time and energy information, and the linearity of the detector system is also improved.

Chapter 3

THE ENDOTOFPET-US DETECTOR DESIGN

Pancreatic adenocarcinoma, which are the exocrine cells that lie in the pancreatic ducts, are the majority type of pancreatic cancers [35]. It is also one of the most aggressive neoplastic diseases and remains one of the most resistant cancers to current therapies, killing more than 266 thousands patients worldwide in 2008. Its curative resection rate is very low due to unspecific symptoms, the lack of early specific biological markers, delayed diagnosis and metastases formation [26]. Prostatic cancer on the other hand is the most commonly occurring cancer in men, and the second leading cause of death by cancer. It can be cured with high probability of success if detected in an early stage of development [6]. The two organs under study are surrounded by organs with a high metabolic update, such as liver, duodenum and gall bladder in case of the pancreas, and the bladder in case of the prostate. Therefore, a big effort is put on the development of new specific biomarkers for pancreas and prostate cancers to achieve a better prognosis of these cancer types.

Endoscopic ultrasonography plays a fundamental role in the diagnosis of pancreatic and prostatic cancers. By coupling an ultrasonic endoscopic probe with a PET detector, and being able to place this detector in close proximity to the organs under study and biopsy¹, one can narrow down the region of interest and thus reduce the background from neighboring organs. Such a device will dramatically improve the detection of early cancers and increase the precision of the diagnosis for small lesions or tumors. Therefore the EndoTOFPET-US project proposes to build a prototype of a PET detector head around a commercial ultrasound assisted biopsy endoscope [7]. The PET detector head can be in close proximity to the organ under study while covering a large solid angle and providing a high sensitivity. An external PET plate is required to cover the projection of the body region under the exam of the probe. Together with the PET detector head, the two modality images obtained by the asymmetric PET detector and the ultrasound probe will be fused to provide intuitive feedback and visualization during the intervention.

The technical objectives of the proposed detector can be concluded as the following:

- The extreme miniaturization of a PET detector system with high coincidence time resolution in the order of 200 ps in FWHM, which according to Eq. 2.12 can efficiently reject noise out of 3 cm along the line of response.
- High granularity of both PET detector systems, and a precise tracking of the detector head when operated in vivo to achieve a millimeter spatial resolution of the reconstructed PET image.

¹The biopsy only applies to the case of pancreatic version of the proposed detector.

- A successful fusion of the tomographic image obtained by the PET detector with the the ultrasound image to allow a hybrid visualization of the biomarker distribution (PET) and the anatomy (US).

In order to achieve these objectives, traditional PMTs used in PET system are not feasible to fulfill the requirement. Therefore novel detectors with better performance and compactness are foreseen to be chosen or developed. Part of this thesis devotes to the investigation of the criterion for selecting or developing the detector components that to be used in the proposed detector. The investigation includes the Monte Carlo simulation of the detector system, which predicts the figure of merit of the detector system and its dependence on the photodetector's characteristics. Therefore the characterization of the photodetector candidates and its correct interpretation.

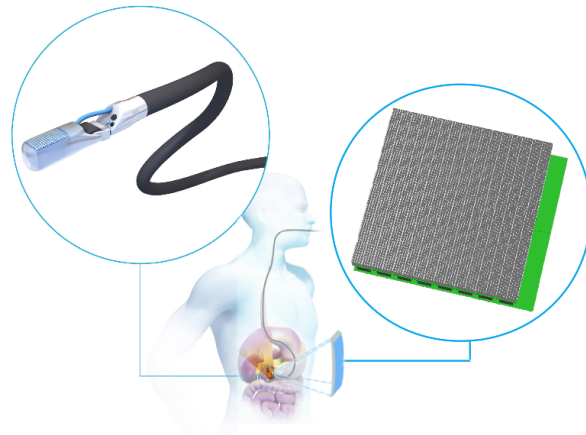


Fig. 3.1: The EndoTOFPET-US detector design concept in the application for pancreatic cancer diagnosis. The top left is the rendering of the ultrasound endoscope probe with the PET detector head extension. The bottom right shows the plate PET detector positioned outside of the patient on the opposite position to the PET detector head with respect to the pancreas.

The EndoTOFPET-US detector consists of two parts (shown in Fig. 3.1), the PET head extension to the endoscope probe and a plate PET detector which will be placed outside the patient for coincidence detection. General design of the two detector designs and the requirement for their performance in order to achieve the technical objectives will be described in this chapter. Detailed simulation and characterizations of the photodetector candidates will be presented in the later chapters.

3.1 The PET Detector Head

Depending on its use either as a trans-rectal (prostate) or gastrointestinal (pancreas) probe, the PET detector head has two different sizes so as to adapt to the respective body orifices. The allowed dimension for the two detector head designs are 23 mm and 15 mm in diameter, respectively. Considering the required performance and granularity for the detector system, high density fast inorganic scintillating crystals readout by semiconductor based photodetectors with dedicated designed readout electronics is the feasible choice for this design.

A custom-developed digital silicon photomultiplier (SiPM) chip will be used as the photodetector in the PET detector head [36]. The digital counter coupled to each single photon avalanche diode provides localized digitization of the photon signal, and on-chip time-to-digital converters are optimum in temporal response since the signal route from the photodetector to the TDCs are minimized. Additionally, multiple

TDCs can capture the arrival time of the earliest photons in a scintillating light flux, which can be used to improve the uncertainty of the timing information through mathematical treatment. It is shown in [37] that a photosensor generates individual timestamps for the first n detected photons is optimum for the timing performance. Moreover, the Cramér-Rao lower bound of timing uncertainty can be reached. The Cramér-Rao lower bound is the theoretical limit on the variance of any unbiased estimator of a deterministic system, which in this case can be interpreted as the intrinsic time resolution that is achievable with the scintillation detector.

The FWHM spatial resolution of a PET scanner can be described using a semi-empirical formula proposed by [38]:

$$FWHM = 1.25\sqrt{(d/2)^2 + (0.0022D)^2 + s^2 + b^2} \quad (3.1)$$

where d is the crystal width, D is the detector distance, s is the effective source size, b is the accuracy of the positioning system and the factor 1.25 takes into account the degradation in spatial resolution due to the tomographic reconstruction. We can assume a reasonable value for the source size to be 0.5 mm, and the detector distance with an endoscopic approach is about 5 cm. In order to achieve the millimeter spatial resolution, the granularity of the PET detector head needs to be less than a millimeter while the tracking precision for the detector should be better than 0.5 mm.

Thin LYSO crystal with the size of $0.71 \times 0.71 \text{ mm}^2$ will be used in order to achieve the millimeter spatial resolution. The crystals are grouped in a matrix of 9×16 and thin reflective material are used to wrap each individual crystal. As a modular component, one matrix will be used in the pancreatic detector head and two identical matrices are used in the prostatic probe. Since the signal digitization is accomplished at the photodetector level, only a low power consumption FPGA is required to be the interface between the photodetector and the front-end electronics. Signal and system clock lines are routed through the endoscope and connected with the data acquisition (DAQ) computer positioned in the operation room. Fig. 3.2 shows the technical design of the PET detector head for the prostatic detector. Since the performance of the digital SiPM is affected by the temperature variation and the influence on the temperature by the head dissipation of the FPGA is not negligible in the limited volume, cooling system to maintain the room temperature is needed. An electromagnetic tracking sensor for the tracking of the detector head during operation is necessary to be embedded in the structure.

3.2 The External Detector Plate

A PET detector plate as a complement to the PET detector head is used to co-register the back-to-back 511 keV gammas, and will be placed externally from the patient. For the optimum coincidence field of view, the detector will cover a $23 \times 23 \text{ cm}^2$ area and have the granularity to deliver the millimeter spatial resolution in the reconstructed image. The design of the detector plate consists of 4096 detector channels using $3.5 \times 3.5 \times 15 \text{ mm}^3$ LYSO crystals read out by analog SiPMs.

As shown in Chapter 2.4.1, the high density of LYSO crystal is efficient in stopping the 511 keV gammas while its high light yield is beneficial in achieving the desired timing resolution. The compactness of the analog SiPM ensures each crystal is read out by a discrete photodetector. For the analog SiPM, a self-triggering readout scheme based on the double-threshold system will be used to determine the energy and timing of each event. Therefore, a SiPM with low dark count rate is important for the implementation of single pixel level triggering threshold which provides the optimum timing performance. The photo detection efficiency of the SiPM is also relevant for the timing performance of the detector. On the other hand, the energy response uniformity to 511 keV gamma among the detector units is also important. The variation in energy response among the detector units may require individual tuning of the energy threshold for 511 keV event which complicates the controlling of the system. Otherwise, if a uniform energy threshold is used for all detector units, detector channels with higher energy response may contribute false hits while channels with lower energy response become less sensitive to gamma events. Therefore it is

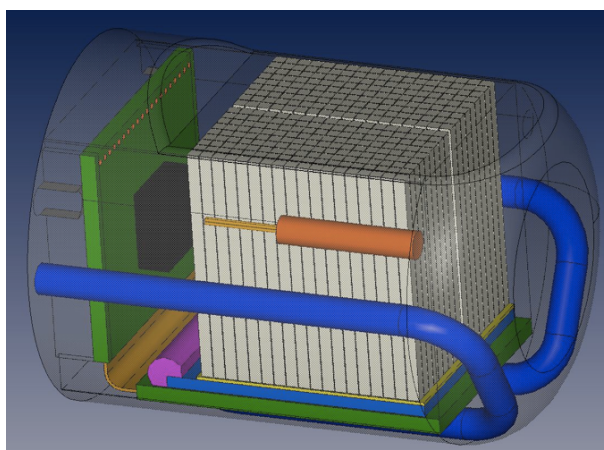


Fig. 3.2: Technical design of the PET detector head for the prostatic detector case. The two matrices of 9×18 crystals mounted on a common PCB hosting the digital SiPM. The readout is provided via the interconnection PCB hosting a control FPGA (black), which interfaces the photodetector to the DAQ. The two cooling lines (blue) maintain the PCB at room temperature. The electromagnetic tracking sensor (orange) is embedded in the support structure.

crucial to correctly characterize the SiPMs and maintain a robust and efficient characterization process for the SiPMs to be used in the detector.

Two dedicated fast 128-channel application specific integrated circuits (ASICs) for the SiPM readout are provided by the collaboration partners, STiC [34, 39] and TOFPET [33], both of which are developed to fulfill the strict requirements for the front-end electronics, such as low noise, low timing jitter and low power consumption along with the possibility to tune the bias voltage of the SiPMs by 0.5 V. In both chips, leading-edge technique is used for time measurement, while energy information is acquired by time-over-threshold (ToT) measurement for each input signal. The TOFPET ASIC chip has implemented the double-threshold system with a low threshold for time measurement and a high threshold for ToT. The STiC chip utilizes the integrating capacitor to stretch the over-threshold time for better signal linearity.

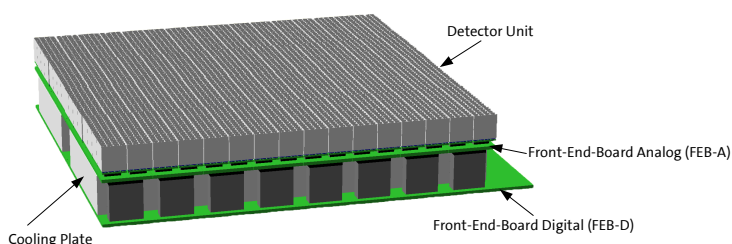


Fig. 3.3: Technical design of the external PET detector plate. The detector unit consists of analog SiPMs reading out LYSO crystals. A front end board (FEB-A) reads out the analog signal from the SiPMs, the on-board 128-channel ASIC chip simultaneously digitizes the signal from 8 detector units. Another front end board (FEB-D) with embedded FPGA board merges the data from different ASIC chips and send the data to the DAQ computer. The cooling plate placed in between the two FEBs takes away the head dissipation from the electronics.

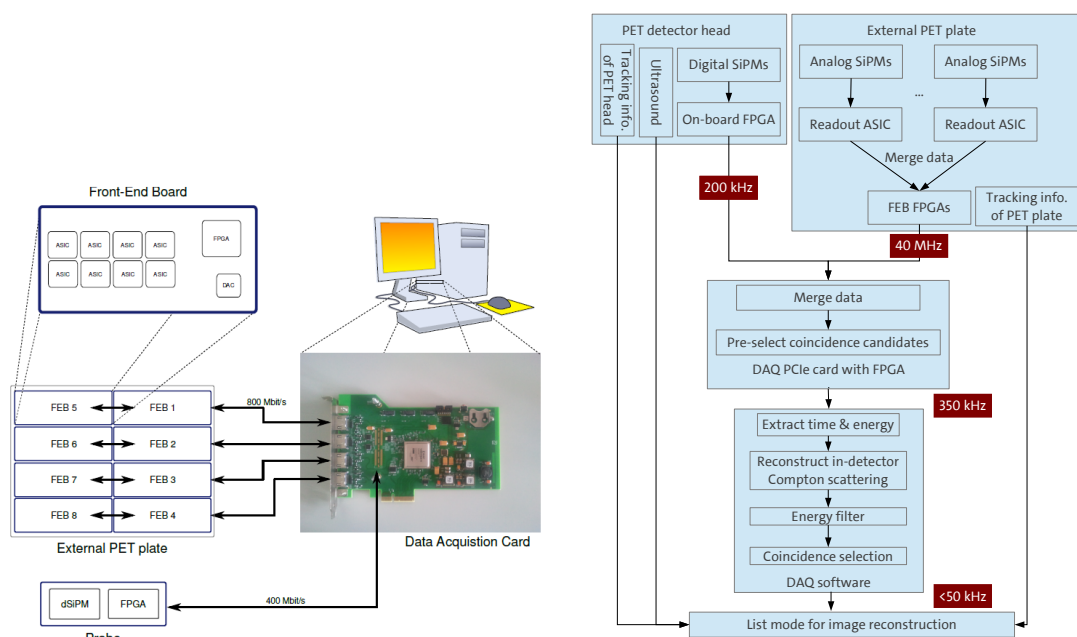


Fig. 3.4: The DAQ system components and the flow chart for the DAQ data processing chain.

In order to maintain the maximum flexibility before the choice is made on the readout ASIC chip, a common design for both chips is implemented for the external plate. As shown in Fig. 3.3, the ASIC chip will be mounted directly on the detector plate, the short signal route from the photodetector to the readout chip is optimum for the timing property. Besides, an aluminum plate with an integrated water pipe will be embedded in the detector housing in order to cool the front-end boards (FEBs) and ASICs. The detector will be held by a movable arm that moves the detector plate in concordance with the endoscope movement as well as tracks the position of the plate with high precision.

3.3 Data Acquisition

The data acquisition (DAQ) system consists of workstation computers for slow control, tracking and image reconstruction and a dedicated DAQ PCIe card installed on the computer and interfaces with the on board FPGAs on the detector plate as well as the PET detector head. The external plate houses eight front-end boards (FEB), each of which accommodates eight ASICs being controlled and read out by a FPGA. The signals from photodetectors are routed to ASICs via flexible printed circuits. After signal digitization, the energy and timing information are concentrated by the FPGAs and transmitted to the DAQ card via HDMI cables. On the other hand, the digital SiPMs used in the detector head are read out by a different FPGA mounted in the probe, which also transmits data to the DAQ card. The designed maximum event rate is 160 kHz per channel and 10 MHz per ASIC [40] for the external plate, this covers the expected event rate of 40 MHz. The designed maximum event rate for the probe is 625 kHz. The DAQ card then merges the data from both the external plate and the probe to perform a coarse event selection of coincidence candidates, using a 12.5 ns coincidence window. This selection reduces the event rate to 350 kHz while ensuring that no interesting events are discarded. The DAQ software then extracts the precise energy

and time information from the events, reconstructs in-detector Compton scattering and performs the final coincidence sorting. With a rate of less than 50 kHz the data is then processed to the image reconstruction software in list-mode format, along with the information from the ultrasound as well as the tracking data of probe and plate. Fig 3.4 shows a flow chart of the whole data processing chain.

Chapter 4

MONTE CARLO SIMULATION

Monte Carlo simulation is a useful and important process in almost all science studies. Simulation softwares can be used to conduct virtual experiments, thus to verify our understanding of the existing system or provide guidance for further development. Simulation studies are present at all stages in the detector development for either medical imaging or high energy physics. A predictive and precise detector simulation needs the implementation of correct and detailed description of the physics that is involved in the detection process. This is sometimes limited by the available computational power and algorithms. Approximations have to be made in order to have a converging simulation algorithm which delivers result in a reasonable time while remains in agreement with the experimental outcomes.

4.1 Single Channel Simulation

A single channel refers to the smallest detector unit in the proposed EndoTOFPET-US detector. It consists of a photodetector coupled to a scintillating crystal. For the internal detector probe, the proposed photodetector is the MD-SiPM, whereas a conventional analog SiPM will be used for the external detector plate. The scintillating material to be used in the detector are inorganic crystals with high light yield and fast decay time. The crystals will be wrapped in reflective material so the light loss at the crystal surface is minimized and most photons arrive at the detector surface. Since the number of detected photons have great impact on the energy and time resolution of the system. A simulation of the single channel detector is performed to provide guidance on the optimization of the crystal and photodetector.

The simulation of scintillation crystal interacting with 511 keV gamma and the transportation of optical light inside the crystal is carried out using the GEANT4 simulation toolkit [41, 42]. It is a software framework that simulates the passage of particles through matter with Monte Carlo methods. The toolkit delivers a wide range of functionalities including complex geometry, physics processes, tracking and hits. Physics models provided by the toolkit handles interactions of particles with matter across a wide energy spectrum ranging from 250 eV up to several TeV. The relevant components of the simulation framework are described in the following. More information on GEANT4 can be found at [43].

4.1.1 General Concept

The GEANT4 toolkit uses object oriented programming technology to provide set of tools for all areas of detector simulation. There are three mandatory classes for the implementation of the detector simulation:

- *G4UserDetectorConstruction*: The fundamental geometry information of the simulated detector and the material properties that is used to construct the detector. Details of the detector construction for

the single channel simulation is provided in the next section.

- *G4UserPhysicsList*: All the relevant physics processes and particle definitions are described. The GEANT4 toolkit provides *physics lists* that have detailed and accurate descriptions of physics processes and particles for medical applications. In addition, the transportation of optical photons and their reflection and refraction at material boundaries is also needed for the single channel simulation.
- *G4UserPrimaryGeneratorAction*: Defines the initial status and properties of the primary particles. The primary particle for the single channel simulation is a 511 keV gamma flying towards the entrance surface of the scintillating crystal.

Once the detectors, physics processes and initial conditions of the primary particles are defined, the simulation starts a *run* which is an analogy of the a real experiment. The *run* consists a sequence of *event* loops, each of which takes the primary particles as input and provides collection of hits or trajectories as output at the end of its processing.

The particles and their interaction in the detector material are simulated by “tracking” the particle trajectory using *track* and *step*. The propagation of a particle is divided into *steps*, and the step length is dived for every possible process and the one with the shortest step length is picked. A *track* object is a snapshot of the particle, it has physical quantities of the current status of the particle, while the *step* object provides the “delta” information between the start and the end of a step. A *track* object is deleted when it goes out of the simulated volume or the particle disappears due to absorption, decay, detected by the detector or its energy goes below the *range cut*. The *range cut* provides a production threshold for the tracking or production of secondary particles in order to keep the number of particles trajectories during the simulation within a reasonable range.

Once all tracks are processed the simulation of an event is finished. Hits collection is automatically stored by the *sensitive detector* volume which is defined by the user. In addition, information of tracking can also be collected by implementing user functions into the corresponding objects.

4.1.2 Detector Construction

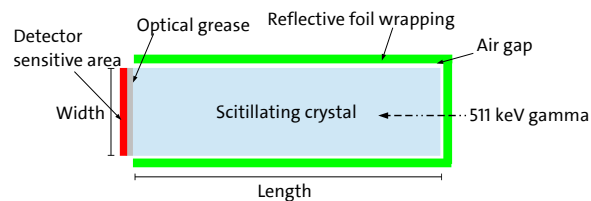


Fig. 4.1: A sketch shows the constructed single channel detector in the GEANT4.

The geometry of a single detector channel is constructed in the GEANT4. As shown in Fig 4.1, the cuboid shaped scintillating crystal has a square cross section. The width and length can be changed in the software. The physical properties, including the composition of the material and its optical properties are assigned to the volume. The crystal volume is “wrapped” by a layer of reflective foil, this is done by specifying the surface property of the crystal to the outer world. A layer of air can be explicitly added in between the crystal and the wrapping material in order to simulate a bad wrapping condition. The photodetector is simulated by declaring a *sensitive volume*, the information of the optical photons which enter the volume are recorded. A thin layer of volume is placed between the crystal volume and the

detector volume, its physical property can be changed between air or optical grease. This is used to simulate the dry contact or glued coupling between the photodetector and crystal.

4.1.3 Physics List

All the physics processes and particles to be considered in the simulation are registered in the *physics list*. The relevant physics processes for the single channel detector simulation are photo-electric effect, Compton scattering for the gamma, scintillation and optical process of the optical photons. Regarding the electromagnetic process of gamma, three different predefined physics lists are provided by the GEANT4, namely the *Standard Electromagnetic model*, the *Livermore EM model* and the *Penelope EM model*. The difference between the lists are described in [44]. The later two models are optimized for the low energy range physics from 250 eV up to 1 GeV. However, because of the relatively simple physics process involved in the simulation, no significant different is observed between the results from different models. In general, the three models use different approaches to compute the total cross section and the final state of the physics process, namely the photoelectric absorption and Compton scattering of the gammas, therefore they can be used to determined the uncertainty of the detector sensitivity simulation results. This is shown in the later section of this chapter.

Since the scintillation process and the transportation of the optical photons are described by a separate model (*G4OpticalPhysics*), which is independent from the above mentioned electromagnetic models. All three models provide the same energy resolution of the 511 keV photo-peak and detector timing performance using the same simulation setup and initial condition. However, the Livermore and Penelope model are more computational expensive, therefore the *Standard EM model* is mainly used through all simulations for time and energy performance of the system.

Scintillation Process

Several empirical quantities are implemented for the simulation of the LYSO crystal according to [45, 46]. The light emission property of the scintillating crystal is controlled by several parameters:

- Light emission spectrum defines the emitted light intensity as a function of the wavelength;
- Light yield defines the number of optical photons created per unit energy (typically MeV) deposited in the crystal. The number follows the Poisson distribution, the fluctuation is narrowed by the Fano factor or broadened due to impurities in the doped crystal.
- Light emitting time property, a rise (τ_R) and decay (τ_D) time constant is used and the emitted light intensity (I) as a function of time is described as:

$$I = e^{-\frac{t}{\tau_D}} \cdot (1 - e^{-\frac{t}{\tau_R}}) \quad (4.1)$$

The scintillation property of the inorganic crystal that is simulated in the program uses measurement results provided by the project collaboration colleagues [47] as input, this ensures the most realistic result of the simulation. The most promising candidate among the tested crystals is the LYSO crystal, its property is summarized in Tab. 4.1.

Tab. 4.1: Scintillation property of the simulated LYSO crystal

Light yield [ph/MeV]	Rise time [ps]	Decay time [ns]
32000	100	40

The Surface Concept

A photon is called optical if its wavelength is much greater than the typical atomic spacing. They are therefore treated in a different way than the gammas. This allows the incorporation of wave-like properties of electromagnetic radiation into the optical photon process [43]. The optical photons can undergo reflection and refraction at the medium boundaries, in flight bulk absorption, Rayleigh scattering or wavelength shifting.

The behavior of the optical photons at the surface of a material has to be considered. Fresnel reflection (R), including total internal reflection, or refraction ($T = 1 - R$) happens when the optical photon reaches a perfectly smooth interface between two dielectric materials. The probability is calculated according to the wavelength, incident angle of the optical photon and refractive indices of the two materials. If the photon encounters a metal like material, it can be reflected or absorbed. Therefore the detector surface is simulated by the metal-like material whereas the surfaces of the crystal, optical grease and the environment are dielectric.

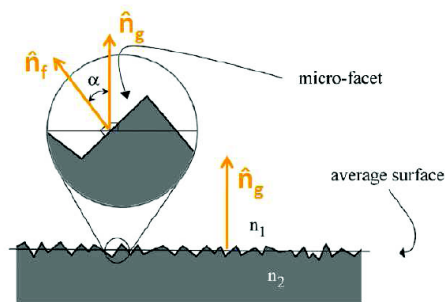


Fig. 4.2: The concept used in the simulation of surface roughness.

In a realistic situation, the crystal is often wrapped by reflective material to minimize losses of optical photons. This is simulated by implementing a UNIFIED model [48], which is developed to deal with the surface finish and reflector coating of the scintillator. The model assumes that a rough surface is a collection of micro facets, with the local facet normals randomly distributed around the average global surface normal with angle α (c.f. Fig 4.2), while the micro facet is considered to be smooth at scales comparable to the optical photon wavelength. The distribution of the angle α is assumed to be a normal distribution, and the roughness can be expressed by the deviation σ_α . [49] has provided the measured σ_α for three typical surface finishes, the result is re-adapted in Table 4.2. Four different boundary reflections may happen depending on the normal of the micro facet and the combination of their constants controls the radiant intensity of the surface (as shown in Fig. 4.3).

Tab. 4.2: σ_α for different surface finishes.

	Polished	Ethed	Ground
σ_α	1.3°	3.8°	12°

- C_{sl} the specular lobe constant, the probability of specular reflection about the normal of a micro facet.
- C_{ss} the specular spike constant, the probability of specular reflections about the average normal of the surface. The surface turns to a perfectly smooth mirror if set to 1.

- C_{dl} the diffuse lobe constant, the probability of Lambertian reflection, in which the reflected forms a diffuse lobe, and the radiant intensity is proportional to the cosine of the angle between the observer's line of sight and the surface normal [50].
- C_{bs} the back scatter spike constant, probability of backward reflection, the case that photons hits a micro facet at a normal angle, after several reflections within a deep groove, and is reflected back along its original path [49].

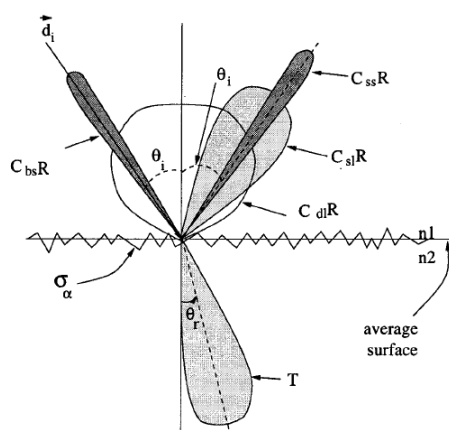


Fig. 4.3: Radiant intensity of different boundary reflections. R is the reflectivity of the surface and θ_i is the incident angle of the photons [49].

A perfect mirror like reflector is represented by $C_{ss} = 1$. While a more realistic case of the surface reflection type is a combination of the specular lobe reflection (C_{sl}) and the diffuse lobe (C_{dl}) reflection. The former type represents the mirror like reflective foil while the later one represents the diffuse light reflector such as the Teflon tape. Their influences on the number of photons arriving the surface of the detector are investigated using a simulation setup consists of a $3 \times 3 \times 15 \text{ mm}^2$ LYSO crystal. Different ratios between C_{sl} and C_{dl} are set to the wrapping material under the condition of $C_{sl} + C_{dl} = 1$, and the reflectivity of the material is 98% ($R = 0.98$). The number of photons in the 511 keV photo-peak as a function of C_{sl} is plotted in Fig. 4.4. The red marker represents the case of perfect mirror like wrapping material with $C_{ss} = 1$. The result indicates a mirror like reflective foil with about 10% of diffuse reflection can achieve the maximum number of photons arriving the detector surface, the perfect mirror like reflector shows about 10% light loss compared to the maximum photon case. A possible explanation is that if the scintillation light is not emitted in the direction of the photodetector, it takes more times of reflection to reach the photodetector in the perfect mirror reflector case, therefore the light loss probability is increased. However, both cases result in more photons than a diffuse reflector.

An other important factor which affects the number of detected photons significantly is the coupling between the photodetector and the scintillator. The simulation shows using the optical grease which has the similar refractive index as the crystal's can increase the number of photons arriving the detector surface in the 511 keV photo-peak by a factor of 2.

The simulation result of the surface condition suggests that a dedicated procedure of wrapping the scintillating crystal with mirror like reflective material and glued coupling between the photodetector and the crystal is required in order to maximize the possible number of photon to be detected by the photodetector. In the following studies, a simple case of perfect mirror like reflector is always assumed (the red marker in the Fig. 4.4).

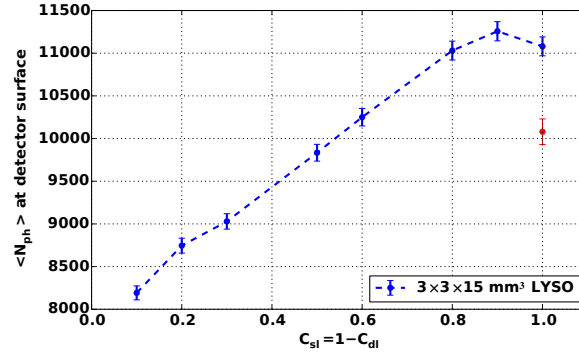


Fig. 4.4: The mean number of photon arriving at the detector surface of the 511 keV photo-peak as a function of the probability of specular lobe reflection (C_{sl}) of the wrapping material. The simulation requires $C_{sl} + C_{dl} = 1$. The red marker represents the case of perfect mirror like wrapping material with $C_{ss} = 1$.

4.2 Single Channel Optimization

The single channel optimization study provides design guidances for the EndoTOFPET-US detector. The single channel detector sensitivity is studied as function of the scintillator's volume, so the detector sensitivity can be achieved within the limit of the geometrical acceptance. More importantly, the selection criterion of the scintillator and photodetector for both internal and external detector is specified by the simulation study so that the time and energy resolution can be achieved. A software model which describes the functionality of the analog SiPM and the MD-SiPM is developed, the simulation of the detector takes characterization measurement results as input so the prediction of the detector's performance can be realistic. The detector simulation software can also be used for the nonlinearity correction of the detector signal.

4.2.1 Sensitivity

The sensitivity of the single channel is defined as the fraction of events in which the photon energy of 511 keV is fully contained in one crystal. This explicitly includes events where one or more Compton scattering occurred before the final photoelectric absorption and events which deposit 511 keV by one photoelectric absorption. Given the absorption length for the scintillating crystal, the sensitivity of a single detector channel scales with the total volume of the crystal. Therefore longer crystals with large cross section size are helpful in maximizing the detector sensitivity. Fig. 4.5a shows the fraction of interaction in different kinds for a simulated $3 \times 3 \text{ mm}^2$ LYSO crystal with different length. The sensitivity of the single channel is represented by the black square dots which have the 511 keV fully deposited in the crystal through either one photoelectric absorption or multiple times of Compton scattering and a photoelectric absorption. The *Standard EM physics model* is used for the simulation. The sensitivity simulated using the other two models shows up to 2% difference in the value.

On the other hand, the intrinsic spacial resolution of the detector is determined by the cross section size of the crystal, and the time resolution deteriorates with the increasing in length of the crystal. Therefore the size of the crystal has to be chosen that allows the design goal in spacial resolution and time resolution while maintains the detector sensitivity as high as possible. The spacial resolution of the detector is mainly determined by the crystal size of the internal probe. Using the size of about 1 mm^2 can allow a spacial resolution of 1 mm at the distance of $\sim 3 \text{ cm}$ from the source. The size of $0.75 \times 0.75 \text{ mm}^2$ is

chosen to match the size of the MD-SiPM sensor (details of the MD-SiPM is described in Chapter 7). The diameter of the internal detector is limited to 23 mm for the prostate probe (corresponds to 72.3 mm in circumference). The strict geometrical acceptance has effectively limited the choice of crystal length below 20 mm. The black marks in Fig. 4.5b shows the gain of detector sensitivity as a function of the crystal length. 15 mm is chosen for the internal probe for the maximum detector sensitivity.

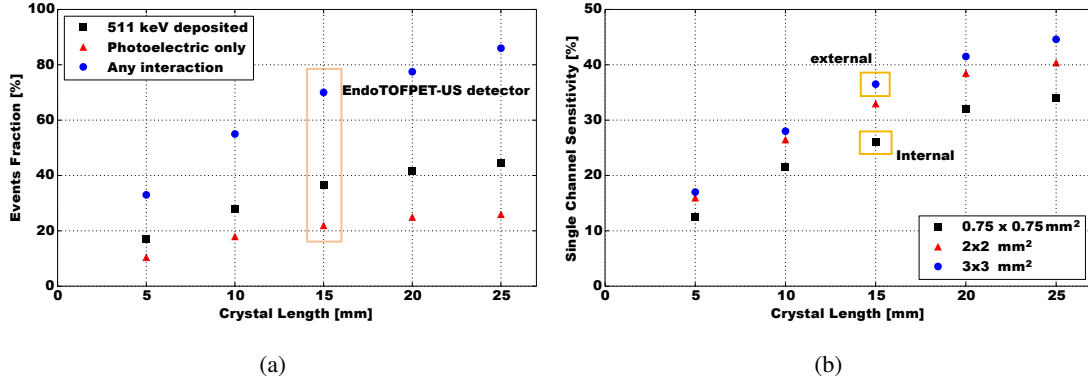


Fig. 4.5: (a) The fraction of events where any interactions occurred (blue), 511 keV is fully deposited in the crystal (black) and 511 keV fully deposited by one photoelectric interaction (red) for a simulated $3 \times 3 \text{ mm}^2$ LYSO crystal with various length. (b) The single channel detector sensitivity by simulation as a function of the crystal length with different cross section areas.

The crystal for the external plate can be chosen from $2 \times 2 \text{ mm}^2$ or $3 \times 3 \text{ mm}^2$ both match the sensor size of most SiPM candidates while ensure the detector spacial resolution. The blue and red marks in Fig. 4.5b show the single channel detector sensitivity as a function of the crystal length for both cross section areas respectively. It shows that the gain in sensitivity saturates for crystal length above 20 mm, and the single channel sensitivity increases by 30% when the length of a $3 \times 3 \text{ mm}^2$ crystal changes from 10 mm to 15 mm, but only increases by 10% when the length changes from 15 mm to 20 mm. Therefore the crystal length for the external PET plate was decided to be 15 mm. By checking the coincidence time resolution (CTR) of the system as a function of the crystal length, it also shows the crystal length shorter than 15 mm allows the system CTR smaller than 200 ps (c.f. Fig. 4.6). The crystal length choice of the EndoTOFPET-US for the internal and external detectors is shown in Fig. 4.5b. The final sensitivity provided by the crystal is obtained by multiplying the sensitivity value of the internal probe and the external plate.

4.2.2 Simulation of the SiPM and MD-SiPM

In order to study the performance of the detector system, custom programs that dedicated to the simulation of the SiPM and the MD-SiPM are developed. The implementation of the program is based on the understanding of the detector working principle, and the program uses measurement results as input parameter. The random process such as photon detection efficiency and the generation of dark count events are achieve by using random number generators. Optical photons simulated by the GEANT4 package are recorded with their detection position and time. The resulted files are used as input parameters for the detector simulation. In such way, the overall detector performance can be studied.

4.2.3 Coincidence Time Resolution

The coincidence time resolution is one of the most challenging and important goals of the proposed EndoTOFPET-US detector. Because the detector design for the external plate leaves some liberty on the choice of SiPMs and crystal size. In order to achieve the design goal of 200 ps coincidence time resolution (CTR), the impact of crystal geometry and detector performance on the coincidence time resolution are investigated. Due to the asymmetric design of the detector system, the requirement for the photodetectors and crystal to achieve the 200 ps coincidence time resolution is studied separately.

External Plate

The default setup for the external detector simulation is a noise free SiPM¹ coupled to a LYSO crystal with cross section size of 3×3 mm². The light yield of the crystal is 32000 photons per MeV, the scintillation rise time is 100 ps and the decay time is 40 ns. The property of the crystal uses realistic inputs measured by [47]. The optical grease gluing is assumed for the coupling of the SiPM to the crystal, and the crystal is wrapped by a reflective material with 98% reflectivity. This guarantees the maximum number of photons arriving the detector surface. In order to consider the time uncertainty introduced by the readout electronics, a 100 ps error is added in quadrature to the obtained simulation result.

The length of the crystal is one of the dominant factor on the travel time of the emitted light in a scintillation process, thus has great impact on the time resolution of the system. The default simulation setup with SiPM PDE set to 20% is used to investigate the impact of crystal length on the time resolution. The uncertainty of time distribution given by the first detected photon from the detector is used as the single channel time resolution (STR), and the coincidence time resolution is calculated by assuming a similar timing performance of the other detector and therefore expressed by:

$$\text{CTR} = \sqrt{2} \cdot \text{STR} \quad (4.2)$$

The obtained CTR is plotted as a function of the crystal length as shown in Fig. 4.6. The result shows a approximately linear deterioration of the system CTR with increasing crystal length. It suggests that for the external plate, a crystal length less than 15 mm is required to achieve the 200 ps CTR design goal.

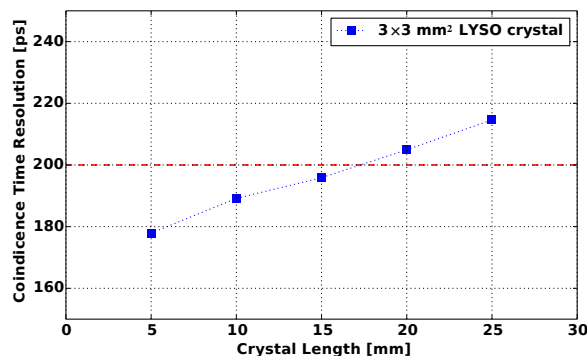


Fig. 4.6: The coincidence time resolution (CTR) as a function of the crystal length. The simulated crystal is a LYSO with section size of 3×3 mm² and light yield of 32000 photons per MeV. The simulated detector has 20% PDE and is noise free. An estimated time jitter of 100 ps introduced by the detector noise and readout electronics is considered. The design goal of the CTR for the system is 200 ps.

¹Detailed description of the SiPM and its characteristics are provided in Chapter 5, here the concepts relating to the SiPM are used without introduction.

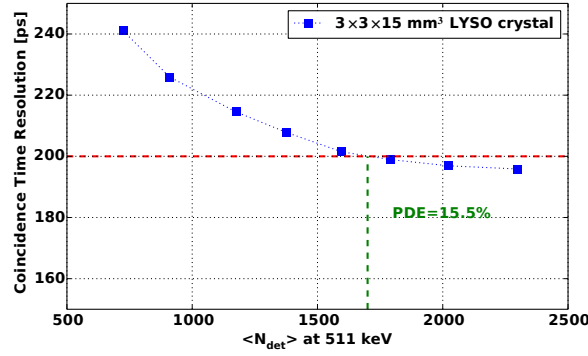


Fig. 4.7: The system CTR as a function of the mean number of photons detected for the 511 keV photo-peak. For the given LYSO crystal with a light yield of 32000 photons per MeV, this translates to the PDE of the SiPM used in the system.

The CTR also strongly depends on the photon statistic of the detector, namely the number of photons detected by the photodetector (N_{det}). This number is mainly affected by the light yield of the crystal, the photon detection efficiency (PDE) of the SiPM and the loss of light during the light propagation in the scintillator. Study in section 4.1.3 already shows the influence of crystal wrapping and detector coupling to the number of photons arriving the detector surface. Using a given condition (represented by the red marker in Fig. 4.5b), the system CTR as a function of the SiPM PDE is investigated.

The result of the study is plotted as the system CTR against the mean number of detected photon ($\langle N_{det} \rangle$) for the 511 keV photo-peak as shown in Fig. 4.7. For a $3 \times 3 \times 15$ mm³ LYSO crystal, It shows at least $\langle N_{det} \rangle = 1700$ photons is required in order to achieve the design goal of 200 ps in CTR. Assuming 11000 photons arriving at the detector surface (the red marker in Fig 4.5b), this corresponds to SiPM PDE of 15.5%. The estimated time jitter of 100 ps introduced by the detector noise and readout electronics is also included.

The reason of showing $\langle N_{det} \rangle$ for the 511 keV photo-peak instead of SiPM PDE is that the former variable is an easier measurable parameter of the detector system. The convolved effects of SiPM PDE, crystal light yield and light loss during propagation is reflected by this single parameter. A systematic study of each individual factor would be time consuming and not necessary. In the final design for the external plate, after measuring the light output of the selected crystal, the requirement for the SiPM PDE can be calculated correspondingly. Since the simulation of the crystal takes the real measurement result as input already, if the wrapping and coupling of the crystal to the SiPM can be assumed near perfect, the requirement for the SiPM PDE is larger than 15.5%.

Internal Probe

The time resolution of the internal probe is mainly affected by the performance of the MD-SiPM² due to its high dark count rate (DCR). However the DCR of the MD-SiPM can be suppressed by turning off the noisy pixels, causing a decrease in the photon detection efficiency (PDE). The simulation study is mainly focus on the trade off between the detector's DCR and PDE and their impacts on the system coincidence time resolution. Fig. 4.8 shows the measured DCR decreases after turning off noisy pixels, the corresponding detector PDE is calculated base on the PDE when all pixels are available.

The DCR of the MD-SiPM affects the coincidence time resolution of the system in two folds. The

²The detailed description of the MD-SiPM and its characteristics are provided in Chapter 7.

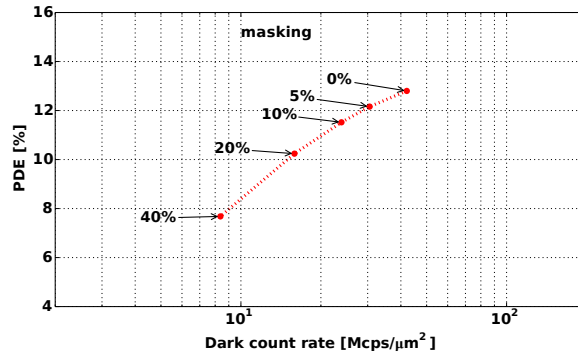


Fig. 4.8: The trade off between MD-SiPM's DCR and PDE. By turning off noisy pixels, the DCR is suppressed at the cost of lower PDE. The data is measured at 20°C with 2.5 V excess bias voltage. The percentage of turned off pixels (masking) are labeled in the plot.

MD-SiPM has multiple time-to-digit converters on the chip connected in parallel to the pixels. A burst of pixel firing within the checking interval indicates a scintillation event, and causes multiple number of TDC being activated. The MD-SiPM therefore utilizes the TDC occupancy as a trigger validation to decide if reads out the data or reset the detector. High DCR may increase the TDC occupancy and pass the validation threshold (false positive), therefore result in dark count events being readout by the detector. These events may not pass the coincidence window, however they increases the number of background events and decreases the detector sensitivity, which eventually affect the system time and energy resolution. The TDC occupancy by DCR is check by using the MD-SiPM simulation tool. The average number of occupied TDC triggered by dark counts within 100 ns is shown in Fig. 4.9. The red line in the plot shows the 90% probability of the TDC occupancy triggered by dark counts, setting validation threshold above it can minimized the case of false positive. In addition, the dark counts recorded together with the scintillation event may increase the uncertainty in determining the first arrived photon.

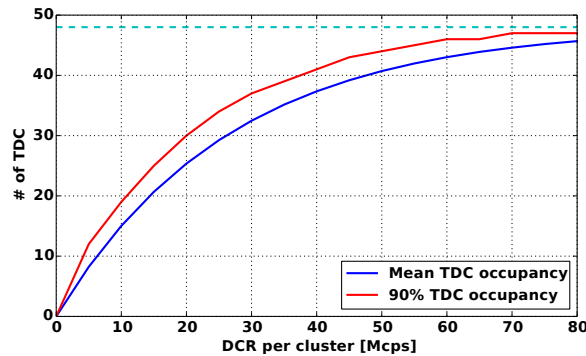


Fig. 4.9: The average TDC occupancy, and 90% cases of TDC occupancy as a function of the dark count rate in a checking interval of 100 ns. The total number of available TDC per column of 18 clusters is 48. This is marked by the dash line on the top of the plot.

The PDE of the device determines the photon statistics and therefore affect the time resolution of the system. According to the measurement of [36], a maximum PDE of 12.5% is expected at 2.5 V excess

bias voltage at 25°C.

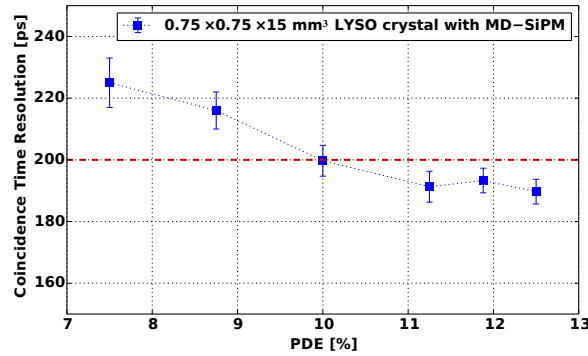


Fig. 4.10: The coincidence time resolution of the simulated system as a function of the MD-SiPM PDE. The MD-SiPM is simulated with 10 MHz DCR and the signal digitization is included in the simulation. The TDC bin width is 45 ps.

The investigation of the time performance for the internal probe has also considered signal digitization effect from the MD-SiPM. The TDC digitization bin width of 45 ps is implemented. A single pixel time jitter of 100 ps is considered for the MD-SiPM. The simulated LYSO crystal has a dimension of $0.75 \times 0.75 \times 15 \text{ mm}^3$ and light yield of 25000 photons per MeV. These numbers are provided by the collaboration colleagues based on their measurements. Due to the complicated combination of the MD-SiPM's DCR and PDE, only the CTR for 10 Mcps DCR per cluster as a function of the PDE is shown in Fig. 4.10. The 10 Mcps DCR can be achieved by either masking about 30% pixels of the MD-SiPM at 20°C with 2.5 V excess voltage, or cooling the device to 0°C. The result indicates that a low temperature operation condition for the final device should be considered in order to achieve the 200 ps CTR.

In conclusion, the simulation of the internal probe shows a tight margin on the performance of the MD-SiPM in order to achieve the 200 ps CTR design goal. A detector PDE higher than 10% and DCR smaller than 10 Mcps per cluster is required. Higher DCR not only deteriorates the coincidence time resolution, but also reduces the detector sensitivity. However, according to [23, 37], the detector system may reach the intrinsic timing resolution limit by making use of timestamps from multiple photons during the initial part of the scintillation signal. This is possible provided by the multiple on chip TDCs of the MD-SiPM. Further studies are required once the MD-SiPM chip with a dedicated crystal is available.

4.2.4 Energy Resolution

The energy resolution of the detector system is the fraction of the 511 keV photo-peak width in full-width-half-maximum ($\frac{\sigma_{FWHM}}{E}$). This is a function of the detector photon detection efficiency for a given scintillating crystal, and is affected additionally by the noise of the readout electronics.

For the SiPM with limited number of pixels and a finite pixel recharging time, its response to large number of photons is not linear. Therefore additional correction to the energy spectrum is needed before quoting the energy resolution. This is done with the help of the Monte Carlo simulation tool. Arbitrary number of photons are generated and detected by the simulated SiPM, thus a detector response curve can be generated. The curve is then used to correct the measured signal from the SiPM. A certain number of fired pixels is back projected to a Gaussian distributed number of photons in the linear axis. Therefore the detector signal is corrected for its nonlinearity. It is worth mentioning that the time distribution of the photons and spacial distribution of the light intensity both influence the linearity correction results.

Therefore the light emission time profile of the scintillator is used when generating the photons for the non-linearity correction. Uniform light distribution over the detector surface is assumed.

The saturation effect is more severe for the MD-SiPM since it has limited dynamic range and it is further decreased by its high dark count rate. A simulation of the above mentioned $0.75 \times 0.75 \times 15 \text{ mm}^3$ crystal with a MD-SiPM of 10 Mcps per cluster DCR and 10% PDE shows an energy resolution of 17~19% at FWHM for the 511 keV photo-peak. Higher DCR up to 50 Mcps can deteriorate the energy resolution to 23~24%.

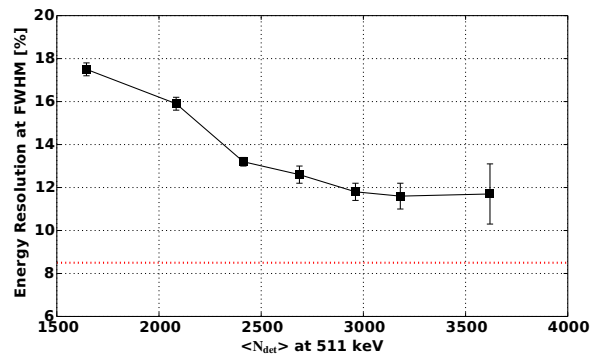


Fig. 4.11: The energy resolution at FWHM for the 511 keV photo-peak as a function of the SiPM PDE after non-linearity correction. The red line shows the intrinsic energy resolution of the crystal that is implemented in GEANT4.

For the external plate, the commercially available SiPMs with $3 \times 3 \text{ mm}^2$ area and $50 \mu\text{m}$ pixel pitch have 3600 pixels. Study of the system time resolution suggests a SiPM with PDE larger than 15.5%, or more than 1700 photons detected for the 511 keV photo-peak is required in order to achieve the 200 ps CTR. Therefore the energy resolution of SiPM with PDE larger than 15% is investigated with the Monte Carlo simulation. The result is presented as a function of the mean number of detected photons in the 511 keV photo-peak. After the non-linearity correction to the spectrum, the energy resolution at FWHM for the 511 keV photo-peak is shown in Fig. 4.11. The simulation and non-linearity correction result depends on the characteristics of SiPM as an input to the program. The simulated SiPM takes the input from a Hamamatsu SiPM with the type number MPPC S12643-050CN with 3600 pixels.

4.3 Summary

The design of a single channel detector of the EndoTOFPET-US detector is simulated in this work. The study of the crystal surface simulation suggests the crystal to be wrapped in a reflective material and using optical glue with similar refractive index for the maximum yield of light on the detector surface. The single channel sensitivity is studied as a function of the crystal length and suggests 15 mm for both internal and external detector. The simulation using different physics lists shows the $3 \times 3 \times 15 \text{ mm}^3$ crystal gives a single channel sensitivity of 34~36%. While the $0.75 \times 0.75 \times 15 \text{ mm}^3$ crystal for the internal probe shows a single channel sensitivity of 24~26%. Therefore the overall single channel sensitivity is 8.2~9.4%. However, this value may be further deteriorated by the event loss due to false positive trigger validation from the MD-SiPM.

In order to achieve a coincidence time resolution (CTR) of 200 ps at FWHM, the crystal length of the external plate should be shorter than 15 mm, and the SiPM PDE of the external plate should be high enough so that more than 1700 photons are detected for the 511 keV photo-peak. Given the assumed

crystal light yield, this corresponds to 15.5% of PDE. Commercially available analog SiPMs are able to match the value. According to [51], the Hamamatsu SiPM provides more than 30% PDE at excess bias above 2 V. Also a time jitter of 100 ps in FWHM contributed by the readout electronics and detector signal time jitter is assumed. With the knowledge of the MD-SiPM, there is very little margin in the performance of the device for the 200 ps CTR. Cooling of the detector to reduce the DCR is suggested. The using of multiple time stamp to improve the time resolution is an essential requirement in order to reach the 200 ps CTR.

The energy resolution of the SiPM for the external plate is expected to be better than 17% with more than 1700 photons detected in the 511 keV photo-peak. The simulation tool has provided a method to correct for the nonlinearity response from the SiPM. The energy resolution of the MD-SiPM depends on its PDE and DCR. Better than 20% at FWHM can be expected with 10% PDE and less than 10 Mcps dark count rate. With DCR of 50 Mcps, the energy resolution deteriorates to 23~24% due to the further reduced dynamic range.

Chapter 5

SILICON PHOTOMULTIPLIER

Semiconductor material, especially silicon, are widely researched and adopted in building photodetectors. Although the vacuum photomultiplier tubes are still the most commonly used photodetectors in many fields, it is a common trend that silicon photodetectors of different kinds start replacing PMTs or being considered as the first choice when building new detectors.

Silicon has several unique properties that make them the suitable material for photodetectors. Compared with vacuum photomultiplier tubes, silicon photodetectors have a higher quantum efficiency over a wide range of wavelength. Photons induce a signal in silicon by lifting an electron from valence band to conduction band. It generally requires less energy than kicking a free electron into the vacuum from a photocathode of a PMT. Silicon photodetectors are insensitive to strong magnetic field while PMTs require magnetic shielding to be properly operated. This feature makes the application of silicon photodetectors possible where conventional PMTs cannot be employed. For example, the PET-MRI dual-modality detector in nuclear medicine. The compactness of silicon photodetectors also allows high channel density or miniaturized detectors to be build. Furthermore, silicon is the fundamental material for most electrical components and circuits. The rapid development of the silicon fabrication technique in the electrical engineering industry is also beneficial in reducing the cost and adopting mass production of the silicon photodetectors. Moreover, it would be possible to integrate functionality and readout circuits directly in the photodetector, further extending its capability.

5.1 Silicon Photodetectors

In general, photodetectors are developed to detect one or several aspects of a light signal including intensity, wavelength, arrival time and spacial distribution. Depending on the applications, emphasis may be put on certain aspect while constraints for the others may be relaxed. Therefore many different kinds of silicon photodetectors exist. Several most commonly used devices are briefly described in this section.

5.1.1 PIN Photodiodes

The PIN photodiode was invented by Jun-ichi Nishizawa and his colleagues in 1950. It consists of highly doped $p^+ - n^+$ junction with low-doped, 'near' intrinsic n^- or p^- region in between. The high-doped regions provide ohmic contacts. When the diode is reversely biased, the intrinsic layer is fully depleted. Photons with energy greater than 1.12 eV can create an electron-hole pair in the intrinsic region. Under the influence of the electric field the electron and the hole drift towards the n^+ and the p^+ regions respectively. A current is generated at the electrodes during the drift time. If more photons enter the intrinsic region at

the same time, the generated current is proportional to the number of electron hole pairs produced by the photon flux.

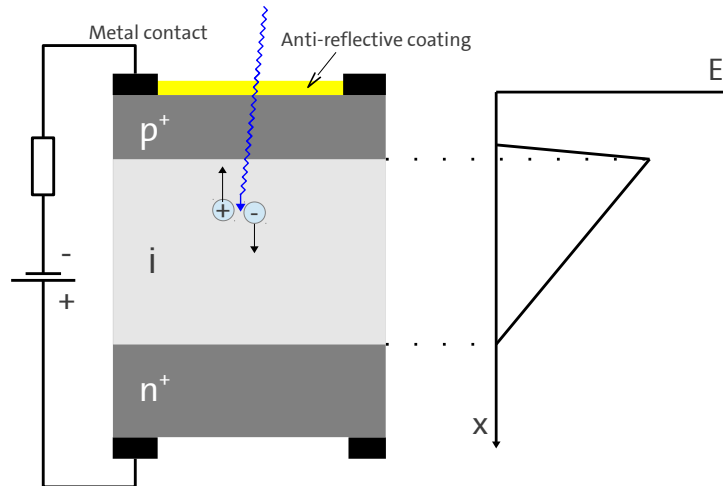


Fig. 5.1: The cross-section of a pin photodiode operated in reverse bias and the electric field distribution of the device.

As shown in Fig 5.1, the features of the PIN diode can be concluded as following:

- The thickness of intrinsic layer can be from a few micrometers up to several hundreds micrometers, it provides large volume for photon absorption. Therefore the device has good sensitivity.
- There is a large potential barrier between p and n side, so the dark current of the device is small.
- The charge carriers created in the intrinsic layer have a long life time, therefore most of the photon generated free charge carriers can be read out before they recombine, which means the device features a high efficiency.
- The device has very fast time response to a signal (typically in nanosecond or sub-nanosecond range.), because the high electric field in the device can quickly remove the photon generated charge carriers and the separation of p -type and n -type layer by the intrinsic layer greatly reduces the capacitance of the device, thus reduces the the RC time constant of the output signal.

However, the pin photodiode does not have intrinsic signal amplification, in other words the gain of the device is one. Therefore it is not sensitive to single photons. A pin diode suffers from an intrinsically generated current in the highly doped regions. This current is typically from few hundreds picoampere up to 1 nA. Only signals generated by a photon flux larger than the intrinsic noise of the device can be detected. Therefore the pin diode is not sensitive for the detection of single photons. Moreover, charged particles ionizing in the silicon can also generate a current signal which can not be discriminated from the photo-current. Therefore the pin photodiode is not suitable for reading out scintillators where low intensity light signal needs to be detected.

5.1.2 Charge-Coupled Device

The *charge-coupled device* (CCD) is the first widely used solid-state imaging sensor. The photon sensing part in a CCD is essentially a p-n junction reversely biased. Photon generated charge carriers are read out by MOS capacitors. Similar to the pin photodiode, a CCD is normally not sensitive to single photons. Only when adding a gain stage between the diode and the readout single photon detection can be achieved. Such a device is called *electron-multiplying CCD* (EMCCD). Cooling is normally needed in order to suppress the dark current of the device, many CCDs are operated in cryogenic environment so that the thermal noise can be ignored.

Another drawback of the CCD is their pixels can not capture the arrival time of the light signal. Self triggered operation for CCD is not possible. Thus they can not be used in the detectors for coincidence measurement such as PET.

A device similar to CCD is called CMOS APS (*active pixel sensor*), it features an in-pixel active element which amplifies the signal from the p-n junction diode. Specially designed sensor [52] can achieve time resolved measurements with gating. However, the noise level of the device does not allow single photon level measurement and the time resolution of the device is not good enough for coincidence measurements in PET.

5.1.3 Avalanche Photodiodes

The *avalanche photodiode* (APD) has a p-n junction operated at reverse bias voltage in the proportional avalanche region. Similar to the pin photodiode, incoming photon creates electron-hole pair by photoelectric effect and the created electron and hole are separated by the electric field. Due to high electric field in the device, the electron or hole can be accelerated strongly enough in between collisions to obtain sufficient energy for the creation of new electron-hole pairs (impact ionization). An avalanche may thereafter be developed and thus the primary photoelectron produces an amplified current signal. With this internal signal amplification, APD can be used for low intensity light detection.

The probability for creating secondary pairs is field dependent and is different for electrons and holes. The ionization coefficient α_n and α_p for electrons and holes describe the number of secondary pairs created per unit length. Fig 5.2 shows the measured ionization rate for electrons and holes in silicon. If the electric field is raised such that only one kind of carrier (electrons for silicon) will produce secondary pairs, the charge generated by the multiplication process will be proportional to the primary generated charge. As a result, the signal produced by the APD linearly depends on the number of detected photons. Typical multiplication factor (gain) of an APD is below 300 and varies with the applied voltage and temperature.

Fig. 5.3 shows the cross section of an APD built on p -type substrate. Assuming uniform doping in the n^+ , p and p^- regions, the distribution of the electric field in the device is shown on the right side. The middle p region is fully depleted and the maximum electric field occurs at the $n^+ - p$ junction. Since the APD is reversely biased, electrons produced in the absorption region will drift pass the high electric field region and initiate the multiplication process, i.e. the electron avalanche. The region which contributes 95% of the multiplication process is called multiplication region [53] while the rest of the depleted region is called drift region where the carrier generation can be neglected. APDs can also be built on n -type substrate in which the photon is absorbed closer to the surface and the generated electrons drift downward through the multiplication region and produce avalanches. In this case if the photon is absorbed below the multiplication region, no avalanche will be produced. Therefore this kind of APD has a reduced efficiency for red or infrared light due to their longer absorption length. Since the absorption region in an APD is much less than the intrinsic layer of a pin photodiode, the APD is much less sensitive to ionization particles compared to pin photodiode.

The reverse bias voltage is crucial for the operation of an APD. At low voltages, no secondary electron-hole pairs are generated, the device behaves as a simple diode. As the voltage goes higher, the ionization rate for electrons in silicon increases rapidly while that for holes stays negligible. The device produces a

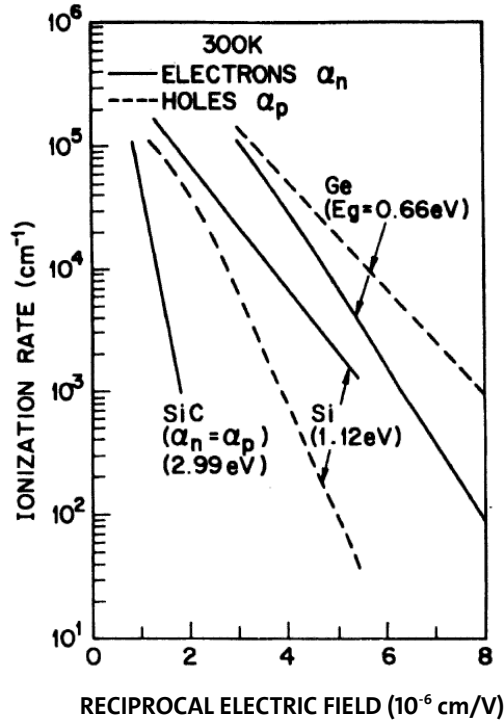


Fig. 5.2: The ionization rate for electrons and holes in silicon and its dependence on the strength of electric field. The plot is taken from [31].

signal that is proportional to the detected light intensity. This is known as the linear mode, the APD works as a linear device similar to PMT in this mode. At even higher voltages, holes will also start to generate secondary electron-hole pairs, and secondary electrons generated by holes may also pass the multiplication region and initiate further avalanches. As a result, the output signal is highly non-linear with respect to the detected light intensity.

The charge multiplication in the device is a statistical process, so the APD's gain fluctuates. The *excess noise factor* (ENF) of the gain can be expressed as:

$$\text{ENF} = \kappa \cdot M + \left(2 - \frac{1}{M}\right)(1 - \kappa) \quad (5.1)$$

where κ is the ratio of the hole ionization coefficient to that of electrons ($\kappa = \alpha_p/\alpha_n$) and M is the gain of the APD. For a sufficient large gain value, Eq. 5.1 can be simplified as:

$$\text{ENF} = (M - 2) \cdot \kappa + 2 \quad (5.2)$$

The silicon APD has $\alpha_n/\alpha_p \gg 1$ in a wide range of voltages as shown in Fig 5.2, thus the excess noise of the silicon APD mainly relates to the gain of the device. When increase the reverse bias voltage of an APD, the gain increases and the excess noise gets worse. When the excess noise produced by the gain dominates the electric noise of the readout circuits, further increase the gain will deteriorate the signal to noise ratio.

The strong dependence of gain to the operating voltage and the temperature has complicated the implementation of APDs in experiments. The operational condition needs to be strictly controlled and

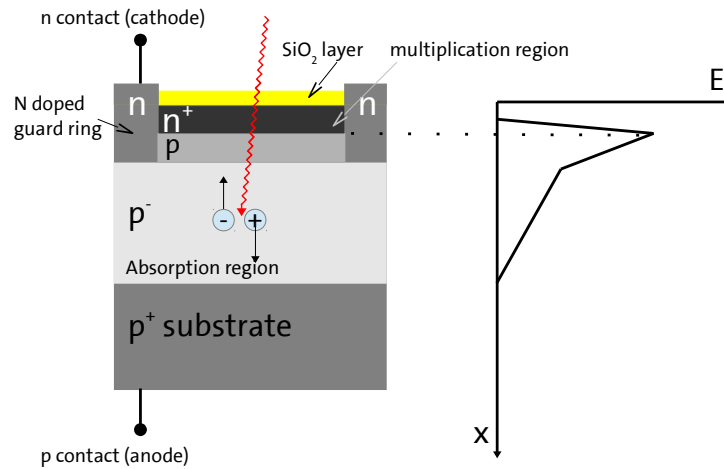


Fig. 5.3: The cross section of an APD built on p-type substrate and the strength of electric field in the device. The figure is not drawn to scale. The p layer is fully depleted and the depletion region extends partially to the lower part of n^+ layer. A lightly doped, 'near' intrinsic p^- layer helps increasing the absorption efficiency. The n -type doped guard ring helps forming a uniform electric field in the multiplication region. The figure is remade from [31].

monitored. Moreover, it is difficult to have a large area silicon device with homogeneous properties. Non-uniformities may cause variation of the electric field in the device thus affect the performance of the device. The limited signal multiplication factor also indicates rather poor time resolution of the device compared to high gain devices such as PMTs and SiPMs. Therefore although APDs are used to build high granularity PET-MR hybrid system [54], they are not the optimum choice for PET detectors, especially when time-of-flight method is required.

5.1.4 Geiger Mode APDs (SPAD)

The avalanche process in an APD ceases when all the produced electrons and holes are extracted from the device without further impact ionizations. However, if the electric field in the device is so strong that on average charge carriers have impact ionization faster than the extraction of charge carriers, the avalanche can be self-sustained and the number of charge carrier increases exponentially with the time. This condition is called "avalanche breakdown" of the diode, and APD designed to be operated above the breakdown point of the diode is called *Geiger-mode APD* (GAPD) due to the similarity of its operation to a Geiger-counter.

The gain of a photoelectron generated in the GAPD is virtually infinite. In practice, the gain of a GAPD remains a finite number, though significantly larger than the gain of a linear mode APD, due to signal quenching which will be explained in section 5.2.2. This feature can be used for the detection of a single photon. Extremely high electric field leads to significantly higher quantum efficiency of the device compared to linear mode APDs and the large gain means excellent timing response. However, the device is not able to discriminate if there are more than one photon simultaneously arriving due to its operational principle; in other words, it becomes a digital detector. Therefore later GAPD specially designed for single photo detection is also called *single photon avalanche diode* (SPAD). Fig 5.4 shows the gain in different

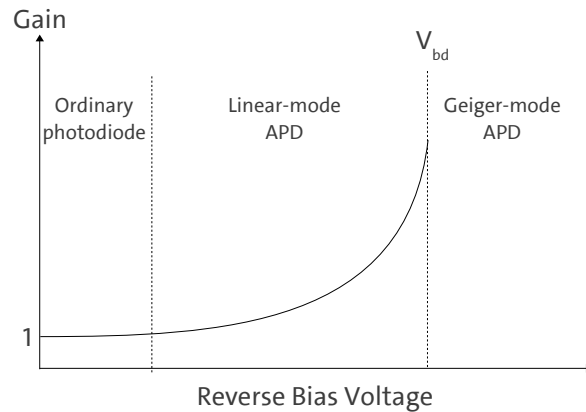


Fig. 5.4: The schematic drawing shows the gain to reverse bias voltage dependence of a photodiode. Operated above the breakdown voltage, the gain is virtually infinite.

working modes of a diode as the reverse bias voltage increases.

Silicon Photomultipliers

The *Silicon Photomultiplier* (SiPM) has multiple identical SPADs connected in parallel to form a single output. In this way, the device preserves the high sensitivity and high gain of a SPAD, and at the same time it has the dynamic range to detect light with higher intensities. The same device also has other different names which normally originate from their producers, such as *Multi-Pixel-Photon-Counter* MPPC, *Solid-State photomultiplier* (SSPM), *multi-pixel avalanche photodiode* (MPAD) etc. Sometimes the name *Geiger-mode avalanche photodiode* (G-APD) is also used for the device. In order to avoid confusion, only SiPM will be used for this type of device, other names may be referred to as a product name for a specific device when necessary.

The name ‘SiPM’ indicates its similarity to the vacuum photomultiplier tubes both in operation and signal interpretation. However the underlying physics of the semiconductor device dominates the design, choice, and adaptation the device for a PET system. The following section will discuss the theoretical basis of the SiPM in details.

5.2 Theoretical Basis

A SiPM consists of a large number of pixels connected in parallel. Within the content of this thesis, a pixel of a SiPM refers to the entire SPAD with its complementary circuit. Fig. 5.5 shows microscopic photos of SiPMs produced by KETEK GmbH and Hamamatsu. The features of a SiPM relates to the properties of the SPAD and the complementary circuit. Therefore the theory for the operation of the SPAD will be given first, followed by the figures of merit of the SiPM.

5.2.1 SPAD breakdown voltage

The SPAD is operated in reverse bias, the p-n junction of the diode is in Geiger mode when the number of created electron-hole pairs per unit time exceeds the extraction rate of the charge carriers, thus the avalanche is self-sustaining. Mathematically, the breakdown condition can be described as the integral

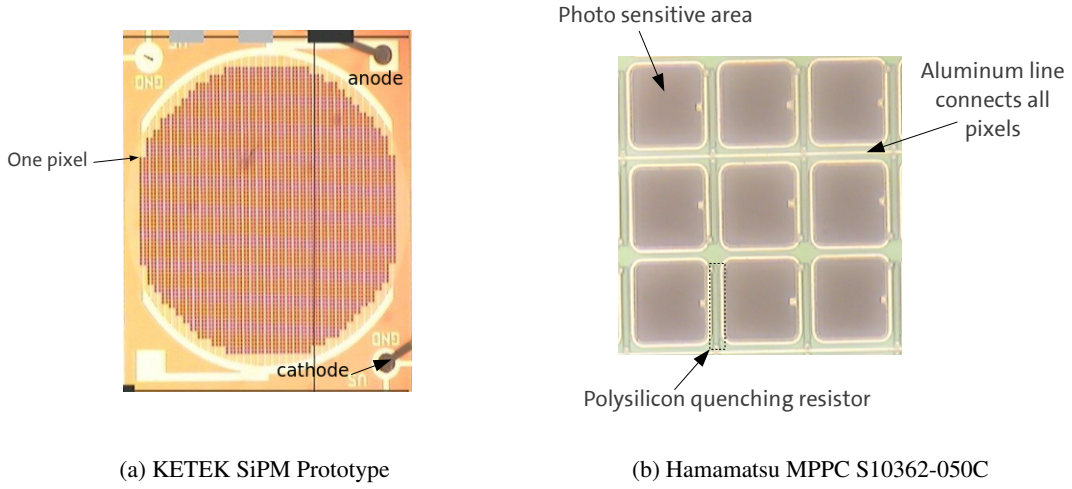


Fig. 5.5: Microscopic photos of SiPM produced by KETEK and Hamamatsu. The left photo shows the cathode and anode node which connects to the corresponding nodes of all pixels of the SiPM. The right photo shows the detail of a pixel in SiPM.

of the ionization rate (α) of the charge carriers along the depleted region, where impact ionization can happen, is larger or equal to one:

$$\int_0^{W_D} \alpha dx \geq 1 \quad (5.3)$$

where W_D is the width of the depletion region, and α is the ionization rate of the charge carriers (assuming the ionization rate of electrons and holes are equal) [53]. The condition where Eq. 5.3 equals to one defines the breakdown point of the device, and the voltage for this condition is called the *breakdown voltage* (V_{bd}) of the diode. In silicon, the avalanche is initiated by the electron and the ionization rate of electrons and holes are different. Therefore, according to Ref [53], Eq. 5.3 becomes:

$$\int_0^{W_D} \alpha_n \cdot \exp\left[\int_x^{W_D} (\alpha_p - \alpha_n) dx'\right] dx \geq 1 \quad (5.4)$$

The difference between the applied bias voltage to V_{bd} when the condition in Eq. 5.4 is fulfilled is called the *excess bias voltage* (V_{ex}).

The breakdown voltage depends on the doping profile of the p-n junction and also to the temperature. The doping profile of a SPAD determines the electric field distribution within the diode and therefore directly affects the breakdown voltage and performance of a SPAD. The breakdown voltage can be derived using the Poisson equation of the p-n junction with depletion boundary condition defined by Eq. 5.3. The solution for a simple model such as the one-side abrupt junction is given by [53].

$$V_{bd} = \frac{\epsilon_s E_m^2}{2q_0 N} \quad (5.5)$$

where ϵ_s is the dielectric constant of the material (silicon), E_m is the maximum electric field in the junction, q_0 is the elementary charge and N is the doping concentration for the lightly doped side. An one-side abrupt junction is a p-n junction with one side distinctly higher doped than the other, and the characteristic of the device is primarily determined by the low-doped side. Although not all SPADs can be approximated by one-side abrupt junction, the device's breakdown voltage is in general inverse proportional to the doping concentration.

Temperature Dependence of the Breakdown Voltage

The temperature dependence of the breakdown voltage originates from the charge carrier's ionization rate ($\alpha(T)$) in Eq. 5.3. Qualitatively, with higher temperature, charge carriers lose more energy to crystal lattice scattering by emitting phonons, thus they need a higher field to acquire the energy needed for impact ionization. Therefore a higher bias voltage is needed to create stronger electric field in the diode for the breakdown condition at higher temperature.

A free charge carrier generated in the depletion region of the diode may lose its energy by two processes, scattering with the crystal lattice and emission of a phonon with energy ϵ_r , or impact ionization and production of a new electron-hole pair. According to the Baraff theory [55], the ionization rate (α) of the charge carrier is a function of the electric field (E) in terms of three parameters:

- ϵ_r the optical-phonon energy, which can be assumed constant for a fixed temperature;
- ϵ_i the ionization threshold energy for the charge carrier;
- λ the carrier mean free path for phonon generation, which means the average distance a charge carrier can travel before it scatters with the crystal lattice and emit a phonon. It can be approximated by

$$\lambda = \lambda_0 \tanh(\epsilon_{r0}/2kT) \quad (5.6)$$

where λ_0 and ϵ_{r0} are λ and ϵ_r at 0 °K, k is the Boltzmann constant and T is the temperature [56].

The derived dependence between ionization rate and the electric field is rather complicated, but can be simplified to two different physics models in the low-field and high-field region [56]:

- In the low-field region, only those carriers which do not experience lattice scattering can reach the threshold energy ϵ_i and contribute to the production of electron-hole pairs.

$$\alpha(E) \propto \frac{q_0 E}{\epsilon_r} \cdot \exp(-\epsilon_i/q_0 \lambda E) \quad (5.7)$$

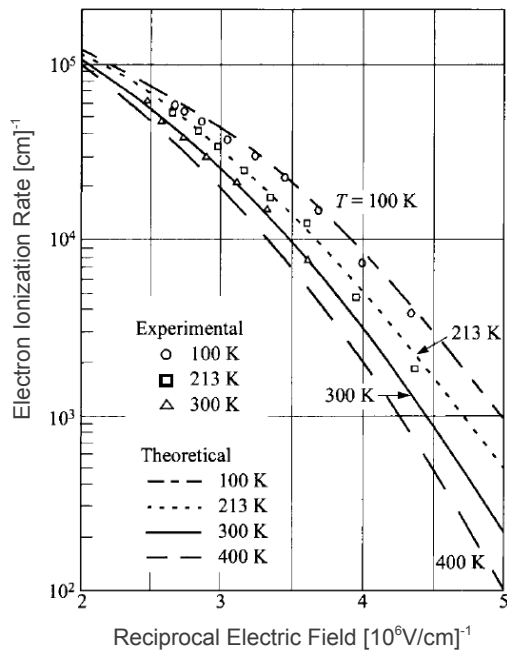
- In the high-field region, the energy loss by the charge carriers due to lattice scattering is small compared to the energy they gained from the field, then lattice scattering only randomizes the energy distribution of the carriers.

$$\alpha(E) \propto \exp[-3\epsilon_r \epsilon_i / (q_0 \lambda E)^2] \quad (5.8)$$

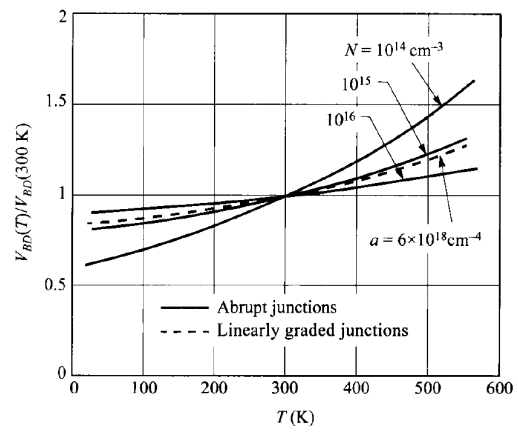
Crowell and Sze have provided a numerical approximation [57] for the dependence between α and E which fits the experimental data in a wide range of electric field for different temperatures, c.f. Fig. 5.6a. The figure indicates SPADs with higher electric field at the multiplication region may have breakdown voltage with less temperature effect. Fig. 5.6b shows the influence of doping concentration on the breakdown voltage's temperature effect. While the curves in Fig. 5.6b shows a quasi exponential shape, when using the SiPM in a small temperature range, the behavior can be very well described by a linear function.

Premature Edge Breakdown

The premature edge breakdown (PEB) effect occurs when an avalanche is initiated at the junction edge before the intended photo sensing area reaches its breakdown. This is undesirable since the PEB effect confines the multiplication region at the corner and prevents spreading of the avalanche. The reason of the PEB effect is that the junction curvature at the corner of a pixel causes higher electric field and therefore has lower breakdown voltage compared to the planar area [59]. The cause of the PEB effect is associated with the design and fabrication process of the SPAD. Solutions to the problem are the implementation of guard rings with different doping profiles such that the electric field is reduced at the edge of the photon



(a)



(b)

Fig. 5.6: (a) Silicon's electron ionization rate changes with electric field and temperature. Experiment points overlay on the Baraff's curve predicted by [55]. (b) The normalized breakdown voltage versus temperature for different doping concentrations, in silicon. Both figures are taken from [53]

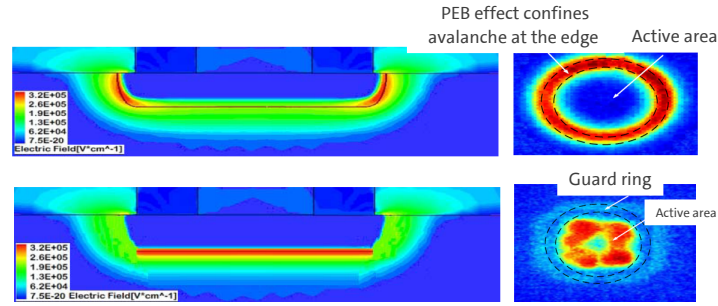


Fig. 5.7: The upper figure shows a SPAD without guard ring implemented, in which the avalanche confines at the corner of the active area. This can be seen from the photoluminescence photo on the right side. The lower figure shows the electric field distribution in a SPAD with PEB prevention guard ring, in which the avalanche can spread to the whole active area. [58]

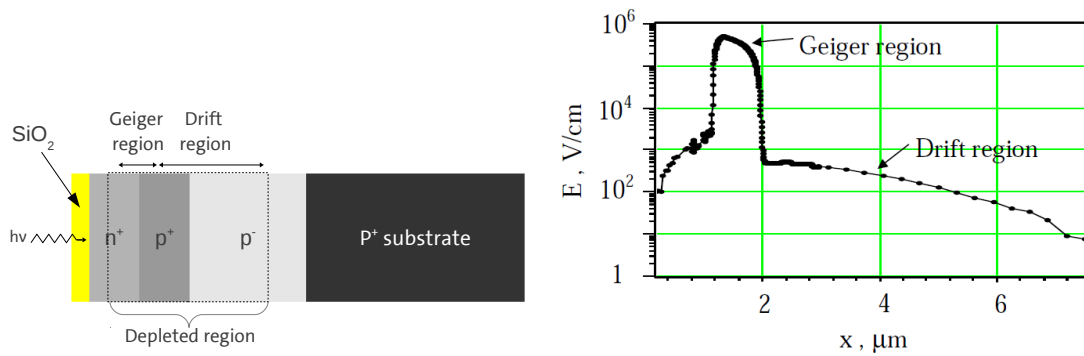
sensitive area, or the use of trenches as guard ring which truncates the junction edge and remove the PEB effect. Fig. 5.7 shows the simulated electric field distribution in the junction of a SPAD with and without guard ring implemented, the figures are taken from [58].

5.2.2 SPAD Quenching

Fig 5.8 shows the cross section of a n-on-p structured SPAD and the electric field distribution within the depletion region of the diode. Because of the coupled space-charge resistance, the avalanche current will not keep growing. As the current grows, the voltage drop across the coupled resistance increases while the local potential on the multiplication region drops until it reaches to V_{bd} . Then the current reaches a steady state with only statistical fluctuations and continues to flow indefinitely which is called latching current [61]. Therefore, shutting off the avalanche current (quench) is required when operating the SPAD. The reason is that only after the avalanche is quenched, the device will be able to detect further photons. Moreover, the current can quickly heat up the diode resulting in thermal damage to the device. A negative feedback mechanism is needed such that the voltage applied to the diode will be brought below V_{bd} every time an avalanche is initiated; after the avalanche is ceased the voltage needs to be raised back (recharge). The diode is in an idle state for the next photon detection. This working cycle is represented by the current-voltage dependence of a working SPAD shown in Fig. 5.9. By quenching the avalanche, the gain of a SPAD remains a finite number. There are two different ways to quench and recharge the SPAD, namely the passive and the active quenching circuits.

The Passive Quenching

The passive quenching circuit can simply be a quenching resistor with large resistance ($R_q = 100\text{k}\Omega \sim 1\text{M}\Omega$) connected in series with the photodiode (c.f. the inset circuit schematics of Fig. 5.9). Since R_q is significantly larger than the coupled resistance of the diode (typically a few hundreds ohm and depending on the structure of the diode [62]), a voltage drop is developed on the quenching resistor which reduces the voltage on the photodiode to V_{bd} . If the asymptotic current $I_f = V_{ex}/R_q$ is small enough that none of the carriers have impact ionization in the high field region of the SPAD, the avalanche is self-quenching. Without the avalanche current, the voltage drop on the quenching resistor decreases, and the SPAD goes back to the idle state for the next photon detection.



(a) Cross section of a $n^+ - p$ junction from a SPAD. (b) Electric field distribution in the depleted region.

Fig. 5.8: Cross section of a SPAD. The p^+ layer is fully depleted, and the depletion region extends to the lower part of the n^+ region and part of the lightly doped p^- layer. However the high electric field multiplication region (or the Geiger region) only exists at the junction between the n^+ and p^+ layer. The p^- region increases the sensitivity for red light and decreases the device capacitance. The left figure is not to scale, the right figure is taken from [60].

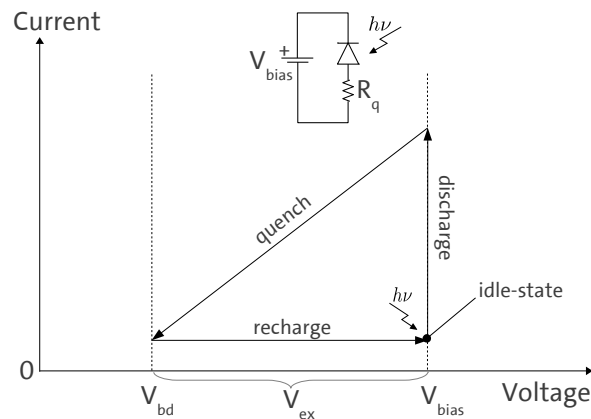


Fig. 5.9: The current voltage dependence of a working SPAD with passive quenching. The diode discharges upon the detection of a photon.

Due to its statistical nature, the switching off of an avalanche has a probability which increases as the current decreases. [62] suggests an avalanche is self-sustaining with a latching current above $\sim 100 \mu\text{A}$ and is self-quenching below it. However, the threshold current is not sharply defined, and designing a quenching circuit with asymptotic current (I_f) close to this value may result in very long dead time of the diode and high power consumption. As a rule of thumb, the designed I_f should be below $20 \mu\text{A}$,

The SPAD is insensitive to further photon detection during the avalanche quenching and junction recharging, this is known as the dead time of the SPAD. The dead time depends on the recharging time of the SPAD which is determined by the RC characteristic of the SPAD circuit. The time constant (τ_r) is dominated by the values of quenching resistance (R_q), pixel capacitance (C_{pix}) and the parasitic capacitance

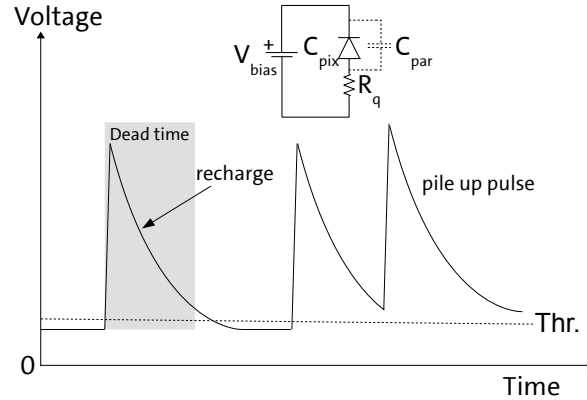


Fig. 5.10: Output signal amplitude of a SPAD. The recharge time is determined by the RC constant of the circuit. Under high event rate, the pile up effect reduces the timing performance of a SPAD.

(C_{par}).

$$\tau_r = R_q \cdot (C_{pix} + C_{par}) \quad (5.9)$$

The dead time reduces the counting capability of a SPAD under high event rate. It also causes pile up effect which decreases the timing performance of a SPAD when using the threshold signal discrimination (c.f. Fig. 5.10).

The Active Quenching

The active quenching circuit normally uses an integrated circuit to sense the pulse signal from the SPAD and generate a delayed signal to turn on a transistor that is connected in series with the SPAD, thus recharging the SPAD actively [63]. The recharge scheme can be specifically designed to decrease the recharging time constant therefore increase the counting capability and timing performance of the SPAD under high event rate. Also, an active quenching scheme can help reducing the afterpulses¹ since the charge flowing in each avalanche can be minimized [64].

The active quenching is more suitable for CMOS compatible SPAD designs in which the circuit can be integrated on chip. The use of a more complex circuit for the active quenching scheme also requires additional area closer to the SPAD, therefore reduces the fill factor when fabricating the SiPM. However, as the feature size in CMOS technology shrinks, the required area for an active quenching circuit will decrease.

5.3 Figures of Merit of a SiPM

5.3.1 Gain

A SiPM consists of large number of pixels connected in parallel, each of which gives same amount of charge output when it fires, meaning produce a Geiger-discharge upon a photon detection. The process can be represented electrically as the discharge of a capacitor with pixel capacitance (C_{pix}). Fig. 5.11a shows the electrical model of a pixel with passive quenching. After triggering an avalanche, the voltage

¹See in section 5.3.5

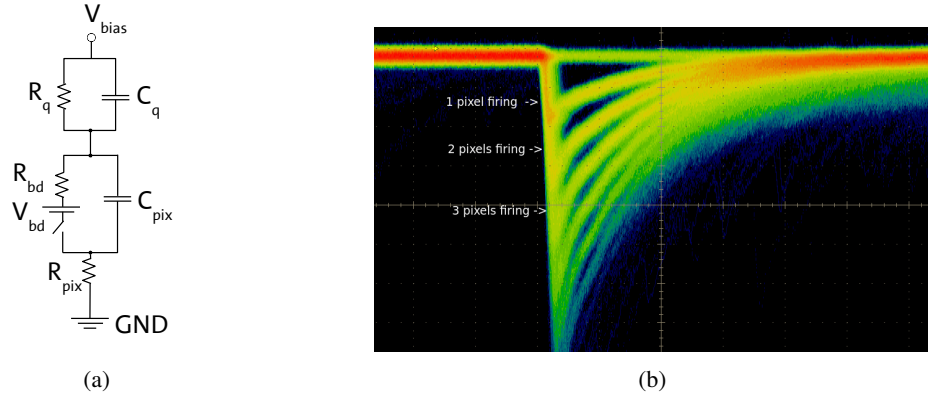


Fig. 5.11: (a) Electrical model of a single pixel in a SiPM using passive quenching. An avalanche breakdown of the diode equals switching on the switch in the circuit. (b) A SiPM's charge output captured by an oscilloscope using persistent mode, due to the large gain, signal separation between different number of pixel fired is clearly visible.

drop on the diode is brought down to V_{bd} by the quenching resistor R_q . So the charge output, which is the gain (G) to a photon detection, can be calculated as:

$$G = \frac{Q_{out}}{q_0} = \frac{C_{pix} \cdot (V_{bias} - V_{bd})}{q_0} = \frac{C_{pix} \cdot V_{ex}}{q_0} \quad (5.10)$$

where Q_{out} is the charge output of the pixel, q_0 is the electron charge. If more than one pixel has fired simultaneously, the charge output of the SiPM will be a multiple of Q_{out} . The nominal gain of a SiPM is in the order of 10^6 , this is enough to distinguish between different number of pixels fired (c.f. Fig. 5.11b).

5.3.2 Dynamic Range

As stated previously, one pixel of a SiPM output a fixed amount of charge regardless the number of photons impinging on the pixel simultaneously. Only with large number of pixels in a small area, a SiPM is able to detect the intensity of a photon flux. However, the response of a SiPM to light flux is not linear, it is normally described by an exponential function [60]:

$$\bar{N}_{fired} = N_{tot} \cdot [1 - e^{-\eta}] \quad \text{where} \quad \eta = \frac{N_{ph} \cdot PDE}{N_{tot}} \quad (5.11)$$

$$\sigma_{\bar{N}}^2 = N_{tot} \cdot e^{-\eta} \cdot (1 - e^{-\eta}) \quad (5.12)$$

where \bar{N}_{fired} and $\sigma_{\bar{N}}^2$ are the average number of fired pixels and its variance, N_{tot} is the total number of available pixels in the SiPM, N_{ph} is the number of photons impinging on the SiPM surface and PDE is the photon detection efficiency of the device. η can be interpreted as the average number of detected photons per pixel. Eq. 5.11 is based on the assumption that the incoming light pulse has very short duration (much shorter than the pixel recovery time) and the photons are uniformly distributed over the surface of the SiPM and the detector noise including optical cross talk and afterpulses are low enough to be ignored. Nevertheless, for a device with higher detector noise, an effective PDE' in which the optical cross talk is included can be used:

$$PDE' = PDE \cdot (1 - \kappa) \quad (5.13)$$

where κ is the cross talk probability and Eq. 5.11 can be modified to:

$$\bar{N}_{fired} = N_{tot} \cdot [1 - e^{-\eta}] + N_{ph} \cdot PDE' \cdot p_{ap} \quad \text{where} \quad \eta = \frac{N_{ph} \cdot PDE'}{N_{tot}} \quad (5.14)$$

where p_{ap} is the afterpulse probability. Fig 5.12 shows a SiPM response curve with its photon resolving capability measured by [60].

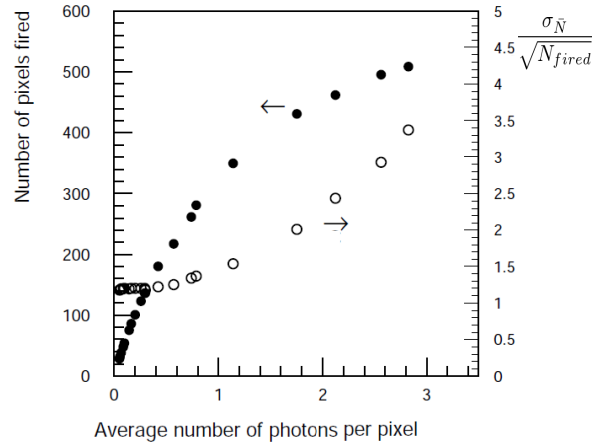


Fig. 5.12: Average number of pixels fired and its fluctuation as a function of average number of photons per pixel (η).

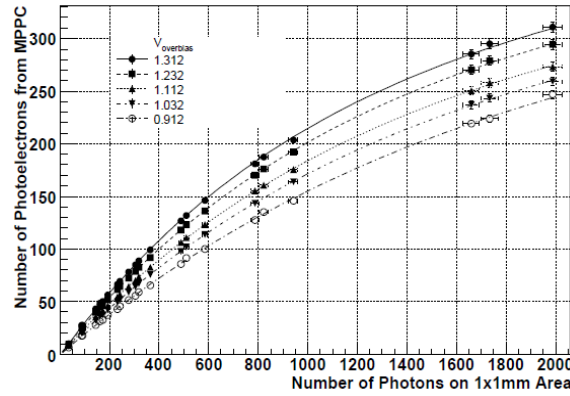


Fig. 5.13: The response curve of a SiPM from Hamamatsu (MPPC S10362-11-50) to different number of photons under different bias voltage [65], experimental data is fitted using Eq. 5.14.

The dynamic range of a SiPM is dominated by the number of available pixels for detection. However, the bias voltage also affects the dynamic range of the SiPM since the PDE' and p_{ap} in Eq. 5.14 depends on the bias voltage. Fig 5.13 shows the different response curves of a SiPM from Hamamatsu with 400 pixels using various bias voltages [65], the experimental data is fitted using Eq. 5.14. Further ways to increase the dynamic range of a SiPM including increase the pixel density or manipulate the light intensity. Zecotek

Photonics Inc. uses a non-conventional process to fabricate their SiPMs (named MAPD, *Multi-Pixel Avalanche Photo Diode*), in which a double $n-p-n-p$ junction with micro-well structures located at a depth of 2-3 μm below the surface. This technique allows the quenching of the discharge in the absence of an additional resistor. In this way a pixel density of $15000\sim 40000\text{ mm}^{-2}$ is possible on an area up to $3 \times 3\text{ mm}^2$. Ref [66] shows that use optical lens to alter the light intensity distribution on the surface of the SiPM, the dynamic range of a SiPM can be increased without increasing the number of pixels in the SiPM.

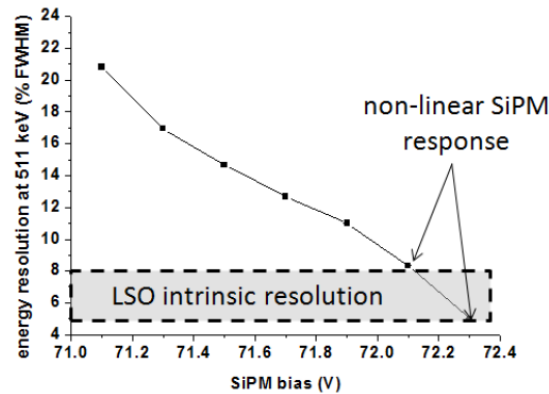


Fig. 5.14: The energy resolution of the 511 keV photopeak taken by a SiPM from Hamamatsu ($3 \times 3\text{ mm}^2$ device with $50\mu\text{m}$ pixel pitch) coupled to a $3 \times 3 \times 5\text{ mm}^3$ LSO scintillating crystal under different bias voltages. Due to the nonlinear response of the SiPM, the calculated energy resolution has exceeded the intrinsic energy resolution of the crystal which is not physically possible [67].

If the light pulse has a duration of the order of the SiPM's pixel recovery time, e.g. the scintillation light with an exponential decay constant from a scintillator, the response of SiPM is more complicated. The effective dynamic range of a SiPM can be extended beyond the total number of pixels of the SiPM since the pixels can be recovered when later photons arrive. With a given operational condition of a SiPM, the description to the response of a SiPM in such case can be achieved with the aid of a Monte Carlo simulation. Also, the energy resolution of the detector system with a non-linear photodetector such as SiPM can not be defined straightforwardly. The usual way of using the ratio between the FWHM of a photo-peak to its energy does not correctly represent the energy resolving capability of the detector. Fig. 5.14 shows an experiment from [67], where a scintillation detector system using SiPM as photodetector has a calculated energy resolution better than the intrinsic energy resolution of the scintillator. In order to correctly show the energy resolution of a detector system, linear correction to the SiPM response is necessary. This can also be done with the aid of Monte Carlo simulation.

5.3.3 Dark Noise

The dark noise refers to the spontaneous Geiger discharge of a SPAD without any photon detections. Mainly due to thermal generation or tunneling effect, free charge carriers may be generated and trigger an avalanche breakdown in the SPAD. The signal in this case is indistinguishable from photon induced signals, and the SiPM will seemingly count photons even when it is operated in dark, thus named dark noise or dark counts. The occurring of dark counts follows Poisson statistic, and is normally characterized by the average rate (Dark count rate) of the whole device or per unit area. The dark count rate (DCR) is a limiting factor for low intensity photon detection, it also limits the timing performance of the detector. As stated in Chapter 2, the optimum time resolution of a scintillation detector system can be achieved

by lowering the threshold to trigger on the first detected photon from the scintillation light. SiPMs with high dark count rate will frequently produce false triggers which increase the uncertainty in the time measurement.

Thermal Generation

The thermal generation of free charge carriers in the depletion region is the major contribution to dark count rate at high temperature (room temperature or above). Due to the indirect band gap of the silicon, direct transition of an electron from the valence to conduction band is very rare. The presence of trap levels in the band gap introduced by crystal impurities facilitates the thermal generation. This process is described by the Shockley-Read-Hall model. The contribution to DCR from thermal generation (DCR_{SHR}) is given by

$$DCR_{SHR} \propto N_t \cdot W_D \cdot \sigma_n \cdot T^2 \exp\left(-\frac{E_a}{k_B T}\right) \quad (5.15)$$

where N_t is the intrinsic carrier density, W_D is the width of depletion region, σ_n is the defect cross section, T is the temperature, k_B is the Boltzmann constant and E_a is the activation energy which is the energy difference between the conduction band and the trap level [68]. Using the Arrhenius plot in which the DCR is plotted against the reciprocal of temperature in logarithm scale, the activation energy can be investigated. [68] suggests that for the SiPM produced by STMicroelectronics, at higher temperatures, the diffusion of the carriers from the quasi-neutral boundaries also contributes to the DCR. However this effect is not observed for SiPMs from other producers.

The DCR contributed by the thermal generation has strong dependence on the temperature, mainly due to the exponential term in Eq. 5.15 [53]. As a rule of thumb, the DCR increases a factor of two for each increase of the temperature by 8 K when the thermal generation dominates.

Band-to-Band Tunneling

In the reversely biased p-n junction, with the presence of strong electric field, electrons have probabilities to penetrate through the band gap and transfer from the valence band to conduction band. This is known as the tunneling effect. The probability of tunneling increases with stronger electric field. The tunneling effect becomes a significant noise source when electric field is 10^6 V/cm or higher [53]. This becomes a major concern for the SPAD fabricated using CMOS process below $35 \mu\text{m}$ technology node, since the field strength scales up as the feature size goes down. Trap levels within the band gap can also facilitate the tunneling process since the potential barrier between the conduction and valence band is effectively decreased by intermediate energy levels.

The thermal generation of carriers dominates the DCR at room temperature. The tunneling effect becomes dominant in low temperature because the thermal generation of the charge carriers is much suppressed. The DCR scales with the bias voltage since the triggering probability for a charge carrier to induce an avalanche increases proportionally with the excess bias voltage. However, at higher bias voltage, the afterpulses² become significant, therefore the measured DCR also scales faster than linear with the bias voltage. The DCR also increases with the pixel size. The impurity density remains constant for the silicon material, therefore larger size pixels have more trap centers for the trap-assisted thermal generation which result in higher DCR. Typical values of dark count rate of the SiPM are below 1 MHz/mm^2 .

5.3.4 Optical Cross Talk

The optical cross talk occurs when the breakdown of one pixel in a SiPM trigger an avalanche in a neighboring pixel. During avalanche breakdown, photons can be emitted on a broad-band spectrum [69].

²See section 5.3.5

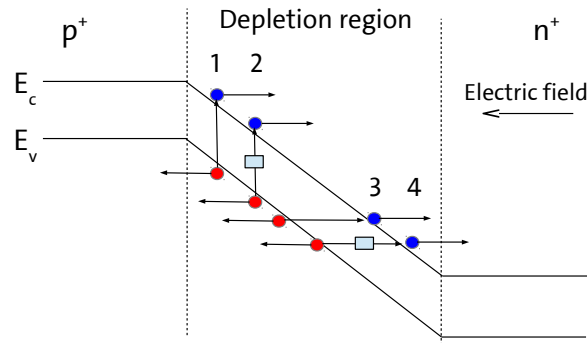


Fig. 5.15: The drawing shows the two processes mainly responsible for the dark noise. 1. Direct transition of electron from valence band to conduction band (very rare); 2. Trap assisted thermal generation; 3. Tunneling effect; 4. Tunneling effect through a trap level.

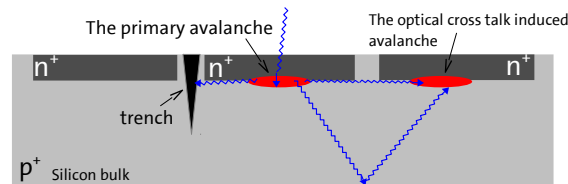


Fig. 5.16: The drawing shows an avalanche in a pixel can emit photons which triggers optical cross talk in the neighboring pixel. There are two paths for the emitted photons to propagate to the neighboring pixel, direct path and reflected from the backside of the silicon bulk. With the help of an opaque trench in between the pixels, the direct propagation of the emitted photon can be stopped.

[70] has measured a photon emission efficiency of 2.9×10^{-5} photons with energy higher than 1.14 eV per carrier crossing the junction, independent of the lattice temperature down to 20 K. Therefore, a SiPM with gain of the order of 10^6 can emit on average 29 photons for each pixel firing. If a photon emitted during the avalanche breakdown has reached sensitive region of the neighboring pixels, it can cause a simultaneous pixel firing thus happens the optical cross talk. [71] suggests that the emitted photon can also be reflected at the back of the silicon bulk and finally be detected by the neighboring SPAD.

The optical cross talk is a noise source that correlated to the original pixel firing. The probability of pixel cross talk increases with the gain of the SiPM, therefore increases with the excess bias voltage. An effective way of reducing the optical cross talk is to implement an opaque trench between the pixels of a SiPM which stops the propagation of photons outside the junction.

5.3.5 Afterpulses

Another correlated noise source is afterpulses of the pixel discharging. It is related to the traps that is created by impurities in the silicon. Free charge carriers generated during an avalanche can be captured by the trapping centers with energy level in the band gap and released later with a characteristic time constant. If the time constant is longer than the avalanche time, the released free carrier can cause an additional avalanche breakdown of the pixel which is called an afterpulse. The probability of an afterpulse (P_{ap}) as a

function of time can be expressed as:

$$P_{ap}(t) = P_t \cdot \frac{\exp(-t/\tau_t)}{\tau_t} \cdot P_{tr} \quad (5.16)$$

where P_t is the trap capture probability which depends on the density of impurities in the silicon and the carrier flux during the avalanche (gain), τ_t is the trap lifetime, it depends on the energy level of the trap in the band gap and the lattice temperature, and P_{tr} is the avalanche triggering probability, it depends on the strength of the local electric field thus the excess bias voltage. In summary, the afterpulse probability increases with V_{ex}^2 since both the trap capture probability and the avalanche triggering probability increases linearly with the excess bias.

If a charge carrier is released before the bias voltage is fully recharged, it can cause an additional pixel breakdown with less charge output than the gain of the pixel. This kind of afterpulses can further reduce the photon counting capability of the SiPM since the reduced charge output smears the separation in charge between different number of pixel fired.

5.3.6 Photon Detection Efficiency

The probability that a photon impinging on the SiPM detector surface triggers an avalanche is called photon detection efficiency (PDE) of the device. The PDE of a SiPM can be expressed in three terms.

$$PDE = FF \cdot QE \cdot P_{tr} \quad (5.17)$$

where FF is the fill factor of the pixel, QE is the quantum efficiency of photoelectron conversion and P_{tr} is the avalanche triggering probability. The product of the later two terms is sometimes called Photon Detection Probability (PDP).

The fill factor is the ratio of the photon sensitive area to the total area of a pixel. As shown in Fig. 5.5, minimum space is required between the pixels for the routing of bias lines, quenching resistors and the separation of the sensitive area from different pixels. Only photons which fall on the sensitive area of a pixel can be detected. The fill factor of a SiPM depends on the design of the pixels which includes the pixel shape, the pixel size, routing of the signal lines and the placing of electrical components. Larger pixel size helps increase the fill factor, however it decreases the pixel density thus the dynamic range of the SiPM, it may also cause higher noise as stated in previous sections. Fill factor values of the SiPM may between 20% up to 70%.

The quantum efficiency is the probability for a photon generates an electron-hole pair once it falls within the sensitive area of a pixel. This depends on the transmittance of the entrance window as well as the photon absorption coefficient, both of which have wavelength dependence. The surface of the sensitive area in the SiPM is normally coated with anti-reflection material. For example using a layer of SiO_2 with thickness of one quarter of the detecting light's wavelength can effectively reduce the reflection of the light thus enhance the PDE. Also, SiO_2 is transparent to UV light which is ideal because the inorganic scintillator used in PET imaging, such as LYSO, emits UV light. The absorption coefficient of light in silicon increases for higher photon energy (shorter wavelength) and has a dependence on the lattice temperature (c.f. Fig. 5.17). Therefore the UV and blue light is absorbed much closer to the detector surface whereas red and IR light can penetrate deeper into the detector bulk.

Free charge carriers may be generated at different places in the p-n junction depending on the photon absorption point. Only those free carriers which drift pass through the multiplication region have high probability to trigger the avalanche breakdown. The minority carriers generated outside the depletion region will quickly recombine. Electrons or holes generated in the depletion region may drift away from the the multiplication region due to the direction of the electric field. Finally, known from Fig. 5.2, electrons have higher ionization coefficient than holes of the same electric field in silicon, thus the triggering

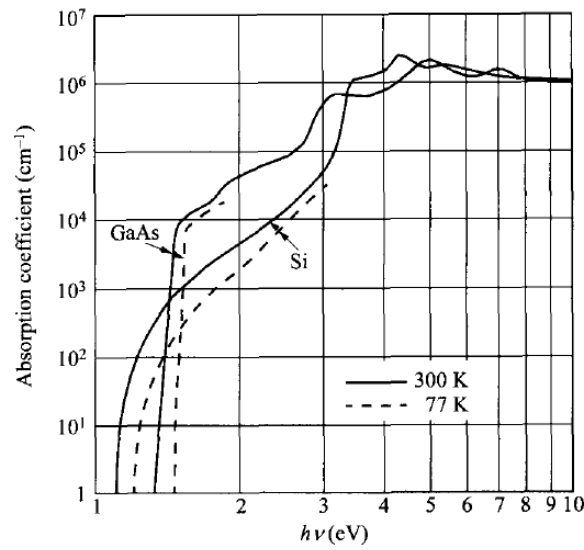


Fig. 5.17: The absorption coefficient of silicon as a function of photon energy at different temperatures [53].

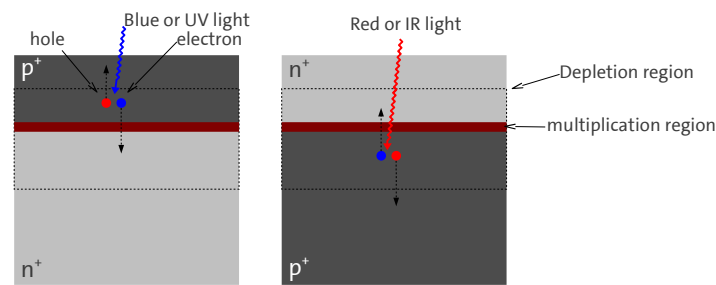


Fig. 5.18: The two different doping profile of SPAD optimized for high PDE on detecting blue or red light. Both use electrons which have higher ionization coefficient to trigger the avalanche in the multiplication region.

efficiency for electrons is higher than for holes. These aspects have great impact on the design of the SPAD for high PDE. For example, the p-on-n device has optimum PDE for the detection of blue and UV light, since the light absorption mostly happens closer to the surface, and when reversely biased, electrons will flow across the multiplication region to trigger avalanche breakdown. On the other hand, n-on-p device has higher PDE for the red and IR light for the same reason that the generated free electrons are used to trigger the avalanche.

5.3.7 Single Pixel Time Resolution

The generation of electron-hole pair by photon absorption and the building up of an avalanche are both statistical processes, the timing variations of the processes are responsible for the time jitter in the output signal, that is called the time resolution of the single pixel.

The free charge carriers that trigger the avalanche may be generated at different depths in the depletion region of the p-n junction. They drift through the depletion region with a saturation speed of about 10 ps

per micrometer of depth [72] until they reach the multiplication region. Once the free carriers have impact ionizations in the multiplication region, the avalanche spreads over the whole multiplication region with a timing uncertainty. The hot-carriers in the avalanche can diffuse or emit photons, both processes assist the spreading of the avalanche. The propagation process of the avalanche in both vertical and lateral directions dominates the timing uncertainty of the pixel response. Therefore SPAD with narrow sensitive area may have relatively better time resolution [73]. Since the electric field is not uniform in the SPAD, photon impinging position also affects the timing uncertainty of pixel response [74].

In addition, the signal transmission time is a Gaussian-like distribution with the mean jitter depending on the delay, thus pixels at different positions within a SiPM may have different time resolutions due to the signal routing distance [74]. This effect can be avoided by using a balanced signal routing for all pixels in a SiPM. The time resolution is usually given as the full-width-half-maximum (FWHM) of the measured photon arrival time distribution.

Chapter 6

CHARACTERIZATION OF THE SiPM

A set of experiments was developed and established in the scope of this thesis, with two main purposes set in mind. Firstly is to select the best suitable SiPM for the external PET detector plate of the EndoTOFPET-US project. Secondly, once the SiPM is chosen, it is foreseen that a large number of SiPMs will be characterized for the commissioning of the detector.

In order to have an objective comparison between the SiPMs from different producers, identical measurement procedure should be applied to all candidate devices. All the figures of merit of a SiPM are important and have different impacts on evaluating the performance of the device. However the information provided by the SiPM producers is often inconsistently defined or incomplete, thus a common setup which is able to perform the same set of tests on different SiPM samples under a controlled environment is necessary. And well established measuring procedures are required to accomplish measurements for a large quantity of SiPMs.

The characterization data of the SiPM provides guidance for the selection of the SiPMs suitable for the project. The interpretation of the detector signal relies on the correct measurement of the gain. The understanding of the SiPM noise can be used to specify the optimal operation condition for specific applications. In addition, the current-voltage (IV) and capacitance/conductance-voltage (C/G-V) characteristics of normal diodes can be obtained and help in the better understanding of the SiPMs. This chapter describes the measuring techniques used in characterizing SiPMs, results obtained by different methods are discussed and compared at the end of this chapter.

The SiPM produced by Hamamatsu, with the type number MPPC S10362-11-050C is used as an example for all experiments that is carried out in this thesis. The device features 400 pixels with a pixel pitch of $50\ \mu\text{m}$. The total active area of the device is $1 \times 1\ \text{mm}^2$. In addition, three SiPMs with type number PM1125 and PM1150 produced by KETEK and MicroFB-10020 produced by SensL are measured. The difference in specifications provided by these devices can help in explaining the results. Their basic specifications are summarized in Tab. 6.1.

Tab. 6.1: Specifications of the SiPMs

Name	Pixel pitch [μm]	N_{pix}	Sensitive Area [mm^2]
MPPC S10362-11-050C	50	400	1×1
PM1125	25	2304	1.2×1.2
PM1150	50	576	1.2×1.2
MicroFB-10020	20	1296	1×1

6.1 Static Characteristics

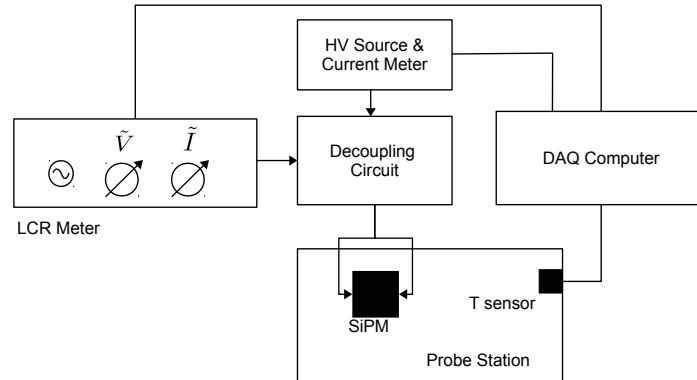


Fig. 6.1: The sketch shows the setup used for the IV and C/G measurement of the SiPM.

The static characteristics of a SiPM include the current-voltage (IV) and capacitance/conductance (C/G-V) characteristic of the device. One setup is used for both measurements. As shown in Fig. 6.1, the probe station facilitates an easy connection to the SiPM anode and cathode pins despite the form factor of the device. It is contained in a lightproof environment with temperature and humidity monitoring sensors. The setup also features a dry-air flow system and a cooling system to maintain the dry atmosphere and stable temperature. A switch on the decoupling circuit selects between IV and C/G measurement without having to reconnect the device and instruments. The DAQ computer has a LabVIEW program to perform the parameter sweeping while recording the measurement results. A Keithley 6517B voltage source with current meter, and an Agilent E4980A precision LCR meter are used in the setup.

6.1.1 Forward Current

Even without bias voltage, a small depletion region is formed in the p-n junction of the diode due to the diffusion of charge carriers. The depletion region acts as a potential barrier which creates a voltage drop over the diode when the diode is biased in forward direction. Once the biased voltage exceeds the voltage drop over the diode, the diode is seemingly conductive with a small resistance R_{pix} . As stated in the previous section, the resistance of the diode is much smaller than the quenching resistance R_q . Therefore, if we assume the forward current flows through all the pixels that is connected in parallel in a SiPM, the quenching resistor used for the pixel can be determined. The forward IV curve can be described by

$$V = V_d + I \cdot R_s \quad (6.1)$$

Where V is the applied voltage, V_d is the voltage drop over the diode, I is the measured current and R_s is a series resistance connected to the diode. The quenching resistance R_q can be obtained by

$$R_q = R_s \cdot N_{pix} \quad (6.2)$$

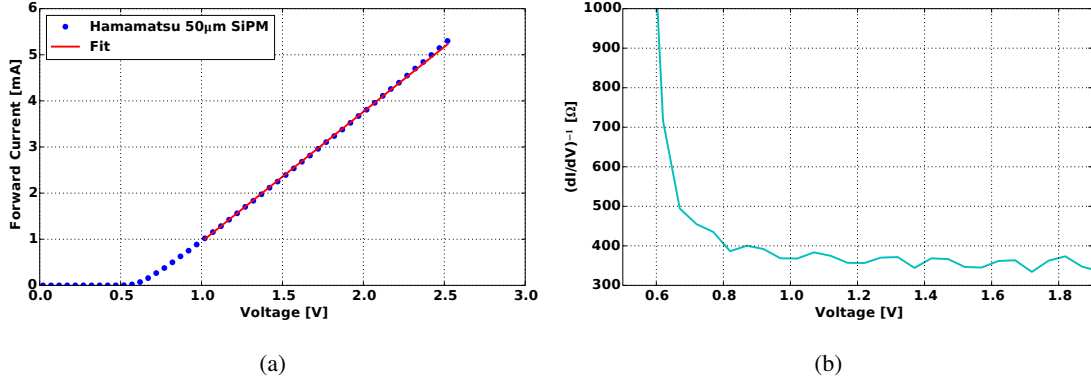


Fig. 6.2: (a) The forward current measurement of the Hamamatsu SiPM. A linear fit is performed on the curve for the determination of the quenching resistance. (b) The reciprocal derivative curve of the forward IV curve. It shows that when the bias voltage exceeds 1.0 V, the reciprocal derivative value stays stable. The periodic structure in the reciprocal derivative curve is an artificial effect from the changing of measuring scales of the current meter.

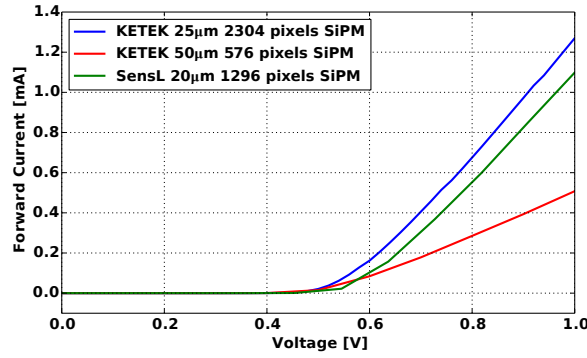


Fig. 6.3: The forward IV curves of the SiPMs from KETEK and SensL.

where N_{pix} is the number of pixels in the SiPM.

Fig. 6.2a shows the forward IV curve of the Hamamatsu SiPM measured at 25°C. The equivalent series resistance is determined from the linear fit on the curve where the fitting range is determined by using the reciprocal derivative of the curve (c.f. Fig 6.2b). $R_s = 355 \pm 5 \Omega$ is obtained from the fit, and the error was estimated by varying the voltage range of the fit. Using Eq. 6.2, the quenching resistance $R_q^{IV} = 142 \pm 2 \text{ k}\Omega$ can be obtained. The superscript indicates the method that is used to obtain the value, parameters obtained using different methods will be compared and discussed at the end of this chapter.

Fig. 6.3 shows the forward IV measurement of the rest three SiPMs from KETEK and SensL. The calculated quenching resistance for the PM1125 is $817 \pm 16 \text{ k}\Omega$, for the PM1150 is $517 \pm 7 \text{ k}\Omega$ and for the MicroFB-10020 is $482 \pm 10 \text{ k}\Omega$. The two SiPMs produced by KETEK should have similar doping profiles, so it can be assumed that the discharging current of a pixel scales with the pixel size. As a result, the SiPM with smaller pixel size requires larger quenching resistance.

The quenching resistance can also help in estimating the upper limit of the excess bias voltage that can be applied to the SiPM. As stated in Chapter 5.2.2, the designed threshold current for the passive quenched

SPAD should be below $20\ \mu\text{A}$. Therefore the tested Hamamatsu SiPM should not be operated above $V_{ex} = 20\ \mu\text{A} \times 142\ \text{k}\Omega \sim 2.8\ \text{V}$, otherwise the pixels can not recover to idle state once fired. On the other hand, the relatively larger quench resistance of the SiPMs from KETEK and SensL indicates that these devices can be operated at much higher excess bias. The calculated upper limit for V_{ex} of these devices are beyond $10\ \text{V}$. However, the determination of the operating voltage of a SiPM is mainly constrained by its dynamic characteristics and the chosen value for the operating voltage is normally much smaller than the calculated upper limit.

6.1.2 Reverse Current

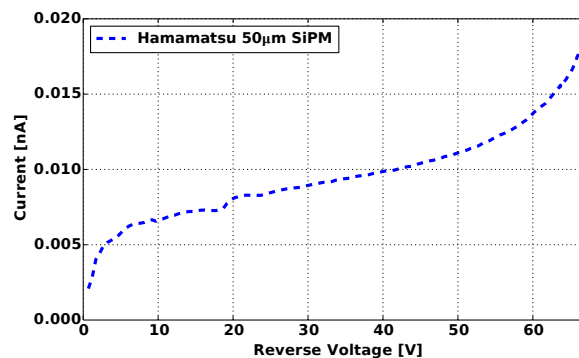


Fig. 6.4: The reverse current of the Hamamatsu SiPM below the breakdown voltage.

When a reversely biased voltage is applied to the SiPM, the width of the depletion region in the p-n junction widens as the voltage increases, until the highly doped region in the diode is fully depleted. The thermally generated free charge carriers in the depletion region are separated by the electric field, thus create a bulk leakage current. In addition, positive oxide charges or defects at the Si-SiO₂ interface act as current generation centers under an electric field and create a measurable surface current. The total measured current is the sum of these two currents and is in the order of several nA/cm². Both bulk leakage current and the surface current increase with the local electrical field, thus the applied voltage.

Fig 6.4 shows the reverse current of the Hamamatsu SiPM below its breakdown voltage. Pixels of the device reach full depletion at about 25 V. The steps shown in the IV curve below the depletion voltage may be interpreted as “sudden” changes in depletion volumes in between the pixels and/or at the periphery of the SiPM. Above the depletion voltage, the measured current increases smoothly with the voltage. When the applied voltage is approaching the breakdown voltage, the thermally generated charge carriers start to have impact ionizations and the number of free carrier is amplified in the diode. Therefore the increasing rate of the measured current to the voltage becomes significantly higher.

Above the breakdown voltage, where the SiPM is operated, pixels can Geiger discharge due to the dark noise. The measured current can be seen as the sum of the surface current and the dark count rate (DCR) together with the correlated noise such as cross talk and afterpulses multiplied by the gain. The gain of the SiPM increases linearly with the voltage while the noise rate increases faster than linear to the voltage and varies between different devices. The total increase rate of the current to the bias voltage is therefore assumed to be between V^n to e^V , where $n > 2$ can be assumed. In order to determine the breakdown voltage of the SiPM, the derivative of the current curve in logarithm scale is calculated, as shown in the lower plot of Fig. 6.5. Considering the derivative $\frac{d\log(x^n)}{dx} = \frac{n}{x}$, the position of the local maximum value in the calculated curve is used as the breakdown voltage, denoted as V_{bd}^{IV} . The error of the obtained breakdown voltage is the step size of the voltage sweeping around V_{bd}^{IV} .

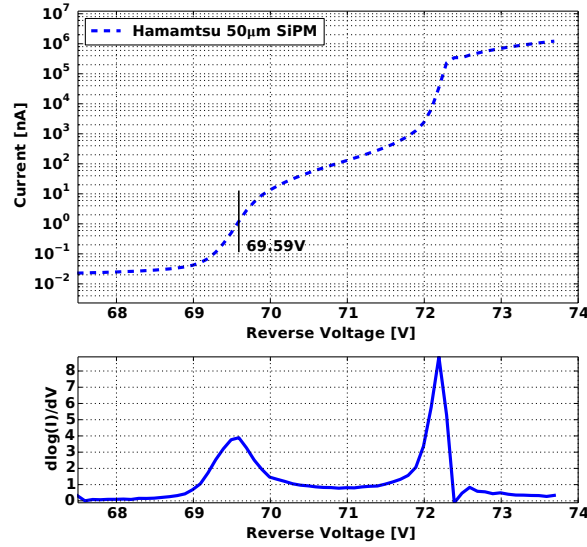


Fig. 6.5: The upper plot shows the reverse IV measurement of the Hamamatsu SiPM in the region near the breakdown voltage at 25°C. The lower plot shows the derivative of the upper curve, which is $\frac{d\log(I)}{dV}$. The breakdown voltage is determined by the position of the first local maximum in the lower curve.

When further increasing the bias voltage, a second sharp increase on the IV curve can be observed. This is the point where the quenching resistance can not effectively quench the avalanche anymore. A latching current flows through the fired diodes, the device shows ohmic behavior and the dependence of current on the bias voltage becomes roughly linear. Therefore another peak can be observed on the derivative of the logarithmic curve.

Fig. 6.6 shows the reverse IV measurements and the determination of V_{bd}^{IV} for the SiPMs from KETEK and SensL. Compared to the curve of the MPPC, the first observation is devices from KETEK and SensL feature much lower breakdown voltages. Although the difference may result from fundamental differences in the doping profiles of the devices, a potential advantage of the device with lower breakdown voltage is the lower power consumption. This may have great impact when designing a detector with large amount of detector channels. In addition, it shows that the devices from KETEK and SensL have larger operating voltage range compared to the Hamamatsu SiPM, this is consistent with the prediction from the measured quench resistance in the forward current measurement.

The reverse IV measurement provides a fast way of determining the breakdown voltage of the device. The precision can be improved by using fine step size during the voltage sweeping. And it is less sensitive to the variation of the environment temperature because the scan around the breakdown voltage region is performed in short time. However, the practical purpose of measuring the breakdown voltage is for the prediction of the gain at a given voltage, therefore the effectiveness of the value determined by this method has to be further investigated.

Table 6.2 summarizes the quenching resistance of the four SiPM samples measured in forward IV measurement and the breakdown voltages extracted by the reverse IV measurements.

6.1.3 Capacitance and Conductance Measurements

The Agilent 4980A LCR meter is used to perform the capacitance and conductance (C/G) measurement on the SiPM. It applies an alternating voltage signal (AC voltage \tilde{V}) with frequency f on top of the DC bias

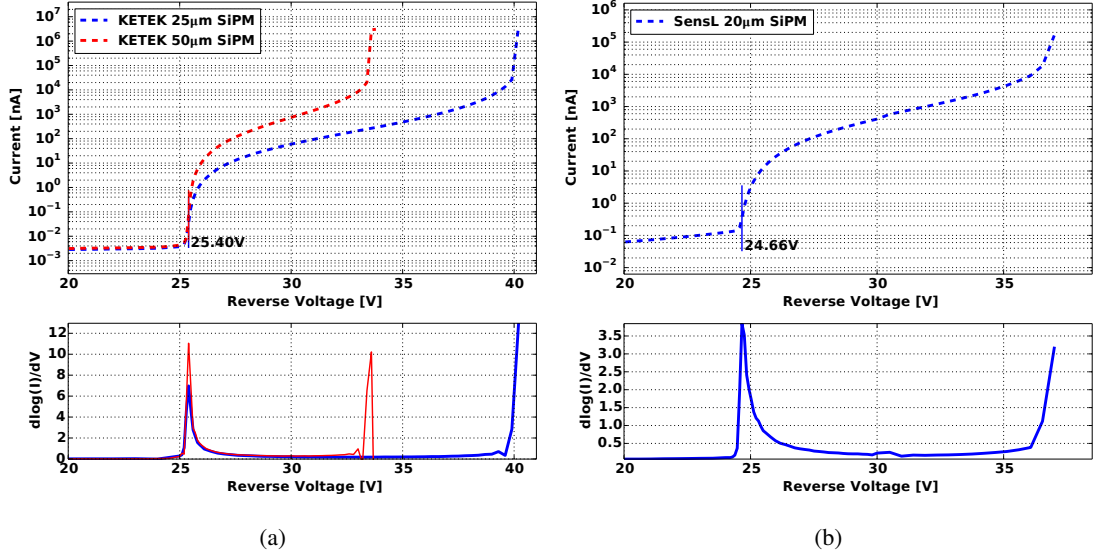


Fig. 6.6: The reverse current of the SiPMs from KETEK and SensL in the region near their breakdown voltages. The determination of their breakdown voltages.

Tab. 6.2: Figures of merit measured by forward and reverse IV measurement

Name	Pixel Pitch [μm]	N_{pix}	R_q^{IV} [$\text{k}\Omega$]	V_{bd}^{IV} [V]
MPPC S10362-11-050C	50	400	142 ± 2	69.6 ± 0.1
KETEK PM1125	25	2304	817 ± 16	25.4 ± 0.1
KETEK PM1150	50	576	517 ± 7	25.4 ± 0.1
SensL MicroFB-10020	20	1296	482 ± 10	24.7 ± 0.2

voltage and measures the resultant AC current \tilde{I} and the phase shift θ . The measured complex impedance of the device under test (DUT) is

$$Z = \frac{\tilde{V}}{\tilde{I}} = |Z|e^{j\theta} \quad (6.3)$$

where j is the imaginary unit.

The result is interpreted by using an equivalent circuit consists of a resistor and a capacitor connected in parallel or in series (c.f. Fig. 6.7¹). When using the equivalent parallel circuit, the admittance $Y = \frac{1}{Z}$ is calculated. The conductance G^p of the resistor and the capacitance C^p of the capacitor is given by

$$Y = \frac{\tilde{I}}{\tilde{V}} = G^p + j\omega C^p \quad (6.4)$$

where $\omega = 2\pi f$ is the angular frequency of the applied AC voltage signal. When using the equivalent series circuit, the impedance Z is calculated. The resistance R^s of the resistor and the capacitance C^s of the

¹The superscript is used for the conductance, the capacitance and the resistance in the two equivalent circuits in order to avoid confusion from the parasitic capacitance and resistance labels used in the SiPM equivalent circuit.

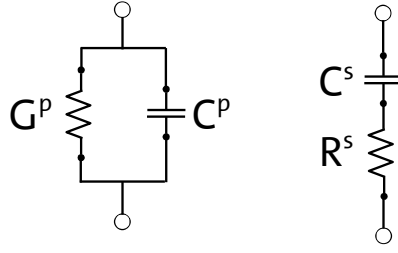


Fig. 6.7: The equivalent parallel (left) and series (right) circuit. Labels are explained in the text.

capacitor is given by

$$Z = \frac{\tilde{V}}{\tilde{I}} = R^s + \frac{1}{j\omega C^s} \quad (6.5)$$

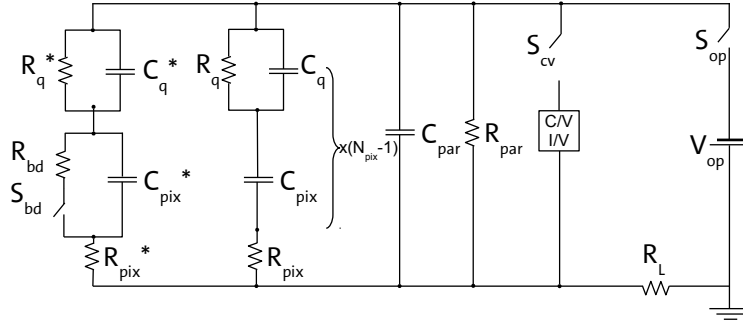


Fig. 6.8: The equivalent electrical circuit model of a reversely biased SiPM. To the left is a firing pixel with Geiger discharge. The remaining $N_{pix} - 1$ pixels are represented in the middle. A parasitic capacitor and resistor are connected in parallel to the pixels to account for the coupling of the biasing lines to the readout electrode. The load resistance R_L represents the readout. The C/V characteristic is simulated by connecting an AC-voltage via the switch S_{CV} to the SiPM with the switches S_{op} and S_{bd} open. The discharge of the pixel is simulated with S_{op} and S_{CV} closed, by closing the switch S_{bd} until the voltage over the pixel capacitance drops from V_{op} to the breakdown voltage V_{bd} .

Using the pixel equivalent circuit shown in Fig. 5.11a, the equivalent circuit a SiPM with N pixels (N_{pix}) can be modeled as shown in Fig 6.8. The firing pixel with Geiger discharge is denoted by an asterisk symbol while the remaining pixels are connected in parallel. A parasitic capacitor C_{par} is connected in parallel to all the pixels in order to account for the coupling of the biasing lines to the readout electrode. The leakage current outside the pixels is represented by a parasitic resistor R_{par} . The complex resistance Z of a SiPM with N_{pix} pixels is given by:

$$Z = \left(\frac{1}{R_{par}} + j\omega C_{par} + N_{pix} \cdot \left(R_{pix} + \frac{1}{j\omega C_{pix}} + \frac{R_q}{1 + j\omega C_q R_q} \right)^{-1} \right)^{-1} \quad (6.6)$$

By comparing the SiPM equivalent circuit to both series and parallel circuits, the C/G measurement with frequency sweeping allows the determination of the pixel capacitance and quenching resistance of the SiPM.

- If the parasitic capacitance C_{par} and the quench capacitance C_q are sufficiently small and can be ignored, the parallel capacitance C^p at bias voltages higher than the depletion voltage of the device equals to $C_{pix}^{CV} \cdot N_{pix}$.
- At high frequencies, the parasitic resistance R_{par} can be ignored, therefore the series resistance $R^s = R_q^{CV} / N_{pix}$.

Where C_{pix}^{CV} and R_q^{CV} denote the pixel capacitance and quenching resistance determined by the C/G measurement with frequency sweeping.

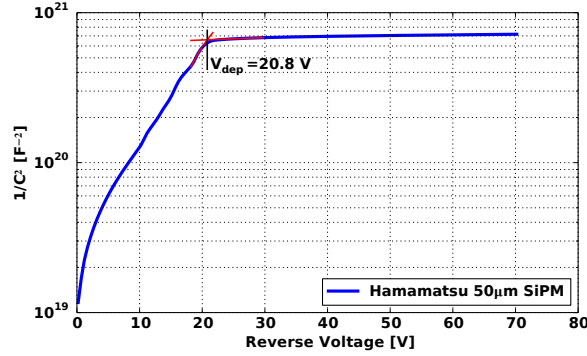


Fig. 6.9: The $1/C^2$ versus reverse bias voltage curve of the Hamamatsu SiPM. The depletion voltage is determined by extrapolating the intersect point of the two linear fit lines in the region before and after the depletion voltage.

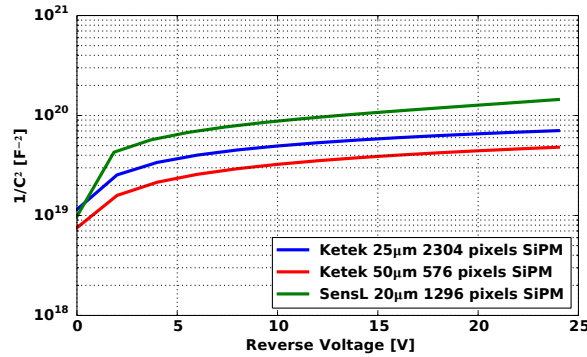


Fig. 6.10: The $1/C^2$ versus reverse bias voltage curve of the SiPMs from KETEK and SensL.

In order to determine the depletion voltage of the SiPM, the C/G measurement with bias voltage sweeping is performed. For a diode consists of one-sided abrupt junction with uniform doping and constant area, the dependence of $1/C^2$ on the bias voltage is expected to be linear until the depletion voltage is reached, where the capacitance remains constant thereafter. Fig. 6.9 shows the C/G-V measurement of the Hamamatsu SiPM in the region from 2 V to 70 V at 10 kHz and 25°C. The observed CV dependence is more complicated than the assumed uniformly doped one-side abrupt junction. Although lacking the knowledge of the doping profile, it can be concluded that the SiPM has reached full depletion above 25 V. The depletion voltage is obtained by extrapolating the intersect of two linear fit in the region before and

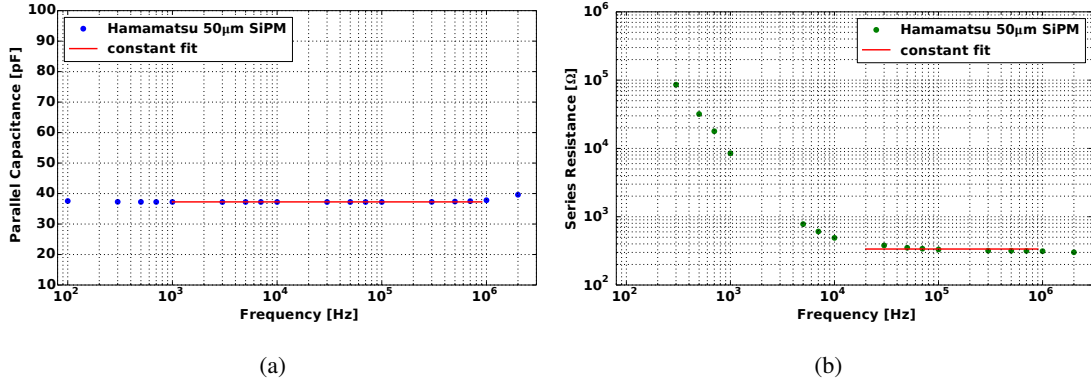


Fig. 6.11: The C/G measurement with frequency sweeping for the Hamamatsu SiPM at 67 V and 25°C. A constant fit is applied to the data at high frequencies for (a) the parallel capacitance and (b) the series resistance.

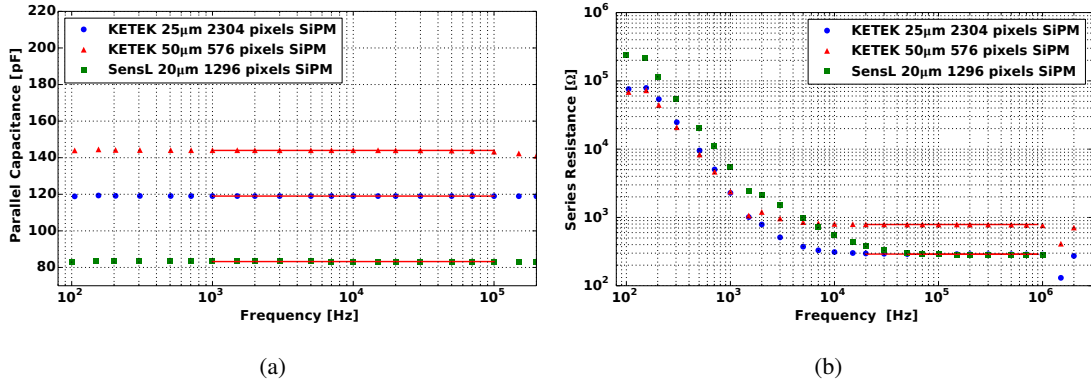


Fig. 6.12: The C/G measurement with frequency sweeping for the SiPMs from KETEK and SensL, (a) parallel capacitance and (b) series resistance. Details of the measurement conditions are given in the text.

after the depletion voltage. The value of depletion voltage of the tested SiPM is $V_{dep} = 20.8 \pm 0.3$ V, the uncertainty is estimated by changing the fitting range of the two linear functions by ± 1 V.

The $1/C^2$ versus voltage curves of the SiPMs from KETEK and SensL are dramatically different from the one from the Hamamatsu SiPM. This maybe because the actual doping profile of the KETEK and SensL SiPMs deviate further from the uniform doping one-side abrupt junction assumption. As shown in Fig. 6.10, the curves are measured at 10 kHz and 20°C. It is not possible to determine the full depletion voltage from the curves. Lacking the knowledge of doping profiles of these devices, it is hard to further compare the differences between them.

Fig. 6.11 shows the parallel capacitance and series resistance from C/G measurement as a function of the AC voltage frequency at 67 V, which is well above the depletion voltage and below the breakdown voltage, for the Hamamatsu SiPM at 25°C. The amplitude of the AC voltage signal is 0.5 V. A constant is fitted to the high frequency range up to 1 MHz, where the measurement result is reliable, to extract the parallel capacitance and series resistance. The obtained $C^p = 37.28 \pm 0.07$ pF corresponds to a single pixel capacitance $C_{pix}^{CV} = 93.2 \pm 0.2$ fF. And the series resistance $R^s = 336 \pm 9$ Ω, which corresponds to a quench resistance of $R_q^{CV} = 135 \pm 4$ kΩ.

The C/G versus frequency measurements of the KETEK and SensL SiPMs is shown in Fig. 6.12. Since the depletion voltage can not be determined from the CV measurement, the reverse bias voltage used for the frequency sweeping is 1 V below V_{bd}^{IV} , at which the pixels are considered to be fully depleted. The amplitude of the AC voltage signal is 0.5 V and the temperature of the measurements is at 20°C. All results from the C/G versus frequency measurement are summarized in Table 6.3. The RC constant, which corresponds to the pixel recharging time is calculated using C_{pix}^{CV} and R_q^{CV} . Comparison of the obtained parameters will be presented at the end of the chapter.

Tab. 6.3: C/G Measurement results of SiPMs

Name	N_{pix}	C^p [pF]	C_{pix}^{CV} [fF]	R^s [Ω]	R_q^{CV} [k Ω]	τ_d^{CV} [ns]
MPPC S10362-11-050C	400	37.3 ± 0.1	93.2 ± 0.2	336 ± 9	135 ± 4	12.6 ± 0.4
KETEK PM1125	2304	119 ± 2	51.6 ± 0.8	291.0 ± 0.8	670 ± 2	34.6 ± 0.5
KETEK PM1150	576	144 ± 20	250 ± 34	788 ± 2	454 ± 1	113 ± 15
SensL MicroFB-10020	1296	83.2 ± 0.1	64.2 ± 0.1	289 ± 3	371 ± 4	23.8 ± 0.3

The pixel capacitance scales with the size of the pixel. This is expected since $C_{pix} \propto A/d$ where A is the area of the pixel and d correspond to the thickness of the depletion region when the pixel is fully depleted. This effect can be seen from the KETEK SiPM. SiPMs from different producers may have significantly different doping profiles, therefore the values are not comparable.

6.2 Dynamic Characteristics

The dynamic characterization extracts figures of merit of a SiPM during the normal operation of the device. These parameters provide guidance on defining the operational conditions when using the SiPM. Figures of merit measured in the scope of this thesis includes the gain and its dependence on the bias voltage, the breakdown voltage, DCR, correlated noise and signal decay time. The photon detection efficiency and the nonlinearity, which are also dynamic characteristics of the SiPM, are not included in the scope of the thesis. This is mainly due to the lack of equipment to precisely measure the photon intensity of a light source, which is essential requirement of these measurements. However, the calibration of the SiPM's nonlinear response to scintillation light is discussed in Chapter 7 with the help of the Monte Carlo simulation tool.

Fig. 6.13 shows a sketch of the setup that is developed for the dynamic characterization of the SiPM. Essentially the setup performs the charge integration measurement to the signal output of the detector in a temperature controlled environment, and is able to provide parameter sweeping such as the bias voltage or integration interval. Devices used in the setup is described as the following. A Keithley 6517B voltage source is used to provide bias voltage for the SiPM. The remote control capability of the voltage source facilitates the automatic voltage sweeping. The diagram of the decoupling circuit used for SiPM readout is shown in Fig. 6.14. It features a low pass filter to attenuate noise from the voltage supply with frequency larger than 80 Hz. The output signal is amplified by a factor of 50 using a Philips Scientific Amplifier (Model 6954) [75] and recorded by a CAEN charge-to-digital converter (QDC 965A) [76]. The VME-based QDC module features 8 dual range charge integrating inputs with 50 Ω impedance. Each channel can measure 0-100 pC with 25 fC resolution or 0-900 pC with 200 fC charge within a integration time defined by a gate. For the SiPM characterization measurements, the lower range is used. An overall uncertainty of 10% for the charge measurement is estimated. When doing the signal pulse analysis, the QDC is replaced by the DPO7254 oscilloscope from Tektronix to record the waveform. A digital pulse generator DG645 from Stanford Research Systems is used to generate the gate for the QDC, it also generates a synchronized pulse to power the LED that is used in the gain measurement. The LED can flash

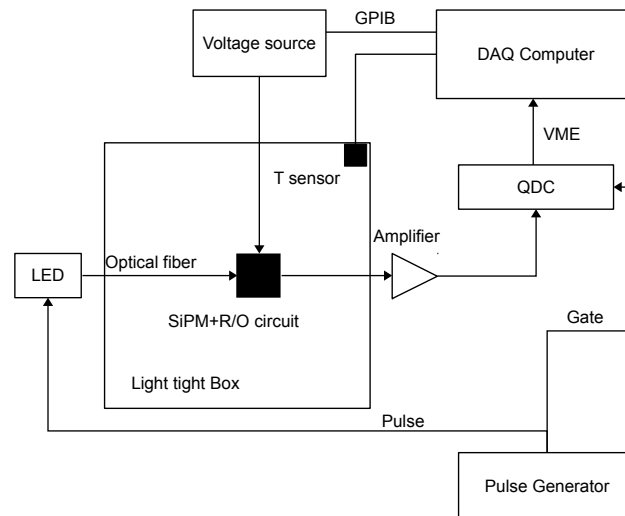


Fig. 6.13: The sketch of the setup for the dynamic characterizing measurement of the SiPM.

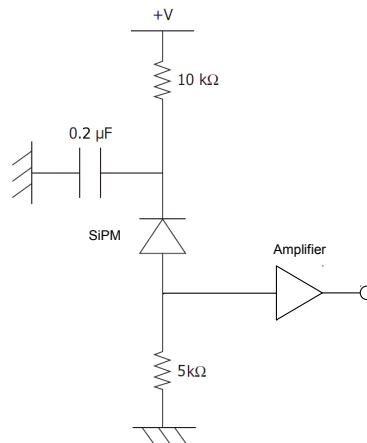


Fig. 6.14: The diagram of the decoupling circuit used for SiPM readout.

violate light with a wavelength of 405 nm. All measurements are carried out in a climate chamber which can stabilize the temperature between 0 to 40°C with an uncertainty of $\pm 0.5^\circ\text{C}$.

6.2.1 Gain and Breakdown Voltage

The gain (denoted by G) is a crucial parameter when interpreting the electronic signal of the detector, therefore a precise measurement of the value is one of the basic requirements for any kind of applications using the SiPM. The gain of a SiPM is not a constant value, Eq. 5.10 shows that it has a linear dependence on the excess bias voltage, which then relies on the precise determination of the breakdown voltage of the SiPM. The main purpose of the experiment is to determine the breakdown voltage and dG/dV , so that the gain can be adjusted to the desirable value when using the SiPM. In addition, when using large number of

SiPMs to build a detector of any kind, these parameters are used to calibrate the response of the detector.

The gain at a given bias voltage is measured by the pulse area spectrum obtained by the QDC, where the amplified signal from the SiPM is fed to the integrating input of the QDC. A square wave signal (gate) determines the time interval for the charge integration. The width of the gate should be larger than the signal, the method that is used to determine the gate width is explained later. The LED illuminates the SiPM to make sure the pixels fire within the gate. The width of the pulse triggering the LED is about 3 ns, this is much smaller than the signal width of the SiPM (in the order of 100 ns), so the pixels are considered firing at the same time by every pulse. The number of photons of the illumination light pulse follows Poisson distribution and the mean is adjusted to be around one, so that it ensures a good visibility to single pixel firing peak.

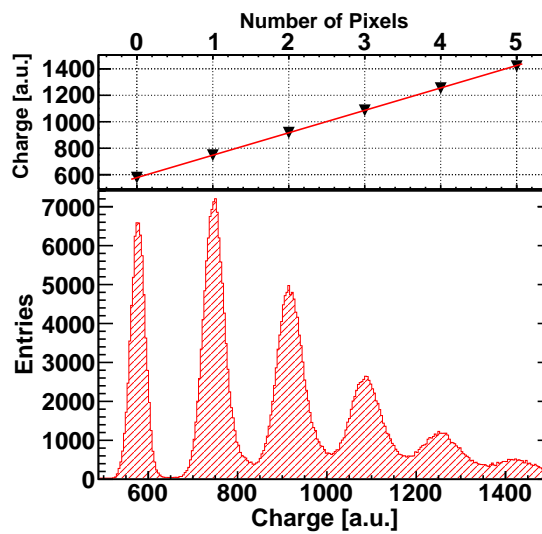


Fig. 6.15: Pulse area spectrum of the Hamamatsu SiPM in QDC units measured at 70.7 V at 25°C. In order to determine the gain, a linear fit is performed on the mean value of each peak and the corresponding number of pixels. The errors of the points in the upper plot, which are the sigmas of the Gaussian fits for the peaks in the lower plot, are smaller than the point marker.

Fig. 6.15 shows the result of a measurement performed on the Hamamatsu SiPM with bias voltage of 70.7 V at 25°C. The well separated peaks indicate good photon counting capability of the SiPM. The left most peak in the spectrum is the integrated charge when there is no pixel fired, which corresponds to the electronic noise of the setup. The second peak from the left corresponds to the amount of integrated charge when there is one pixel fired. Later peaks correspond to multiple number of pixels firing at the same time. Since the gain of every pixel in the SiPM is equal, the mean value of these peaks are equally distanced, the distance corresponds to the gain of the SiPM. The upper part of Fig. 6.15 shows the mean value of each peak plotted versus the number of fired pixels (n_{pix}). The values are obtained by fitting a Gaussian function to each individual peaks in the spectrum. A linear fit is applied to the data and the gain of the SiPM is given by

$$G(V) = \frac{1}{q_0} \frac{dQ_m}{dn_{pix}} \quad (6.7)$$

where Q_m is the integrated charge and q_0 is the elementary charge.

The peaks in the spectrum is often referred to as photoelectron (pe) peaks in other literature [51], thus the spectrum is also called single-photoelectron spectrum. This is a legacy name inherited from

similar measurements using PMT. However, it's worth noting that multiple photons enter the same pixel at the same time only cause one pixel firing and produce the amount of charge of one pixel discharging. Therefore strictly speaking, the spectrum only counts pixel's discharging rather than photons.

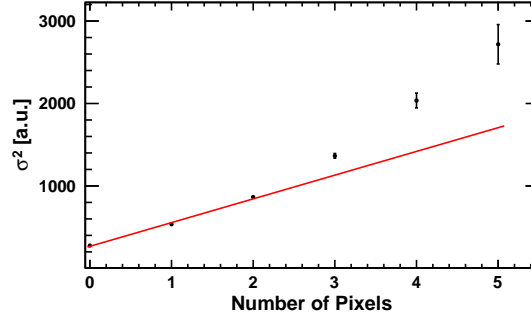


Fig. 6.16: Each peak in the spectrum shown in Fig. 6.15 is fitted by a Gaussian function, σ^2 in an arbitrary unit (QDC bin) from the fitting functions are plotted against the number of pixels. A linear fit is performed on the plotted points, the errors of the first three points are smaller than the marker.

The width of the first peak (σ_0 from the Gaussian fit) in Fig. 6.15 corresponds to the fluctuation of the electronic noise. It is independent from the SiPM and reflects the quality of the readout electronics. The width of the second and subsequent peaks (σ_N) increases due to two reasons: the statistical nature of the amount of charge produced by a pixel firing and the non-uniformity of the gain over the pixels. Using the propagation of uncertainty, σ_N^2 follows:

$$\sigma_N^2 = N \cdot \sigma_G^2 + \sigma_0^2 \quad \text{where } \sigma_G^2 = \sigma_1^2 - \sigma_0^2, \quad \text{and } N = 1, 2, 3 \dots \quad (6.8)$$

Therefore, higher order peaks start to smear due to their increased peak widths. Fig. 6.16 shows σ^2 of each peak in the spectrum in Fig. 6.15 plotted versus their corresponding number of pixels. A linear fit is performed on the data points, in the whole data range. Since the first three points have significantly smaller errors compared to later points, the fitting result is dominated by these points. The result suggests for large number of pixels, the width increases faster than what Eq. 6.8 has predicted. One possible explanation is the effect of signal afterpulses. Since an afterpulse may happen closely after the pixel discharging, results in partially integrated by the QDC. This further smears the separation between the peaks and produce an asymmetric tail on the right side of the pixel peak. When the peaks are fitted to a Gaussian function, the resulting σ is therefore larger than the predicted value from Eq. 6.8.

As a comparison, a pulse area spectrum and the corresponding σ^2 versus number of pixels plot of a SiPM PM1125 from KETEK is shown in Fig. 6.17. The device has much less afterpulse probability compared with the Hamamatsu SiPM. It can be seen that σ^2 versus number of pixels follows the Eq. 6.8 up to 8 pixels until σ^2 value starts to deviate.

According to Eq. 5.10, the gain falls to zero at the breakdown voltage, this is used to determine the breakdown voltage of the SiPM. Fig. 6.18 shows the dependence between the gain and reverse bias voltage of the MPPC. A linear fit is used to extract the breakdown voltage of the device. The pixel capacitance can also be determined, since

$$C_{pix} = q_0 \frac{dG(V, T)}{dV} \quad (6.9)$$

which is the slope of the linear fit.

The dependence of the breakdown voltage on the temperature can be measured by repeating the gain-voltage sweep measurement under different temperature. The temperature coefficient for the Hamamatsu

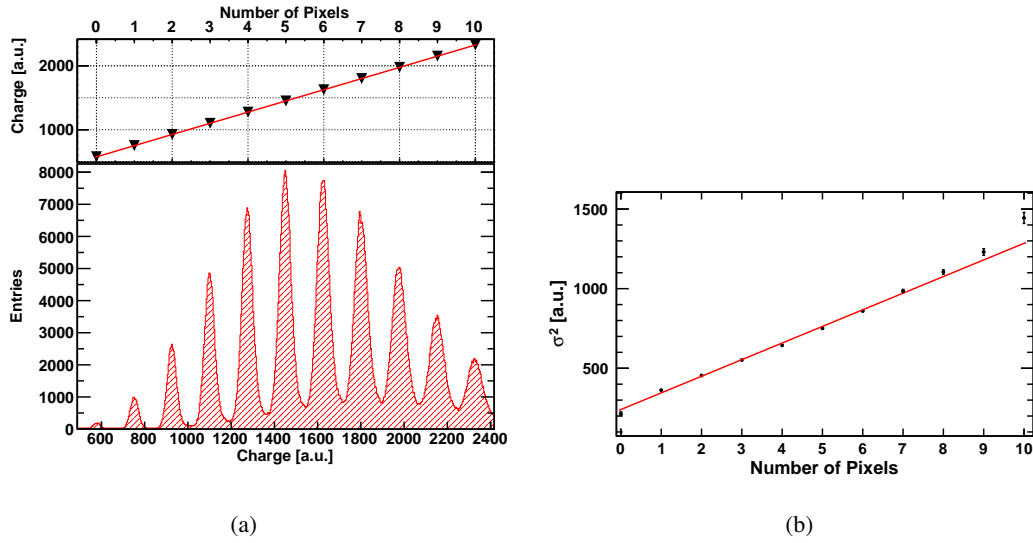


Fig. 6.17: The pulse area spectrum and the corresponding σ^2 versus number of pixels plot of the SiPM PM1125 from KETEK, with much less afterpulse probability compared to the Hamamatsu SiPM, σ^2 versus number of pixels follows Eq. 6.8 up to 8 pixels.

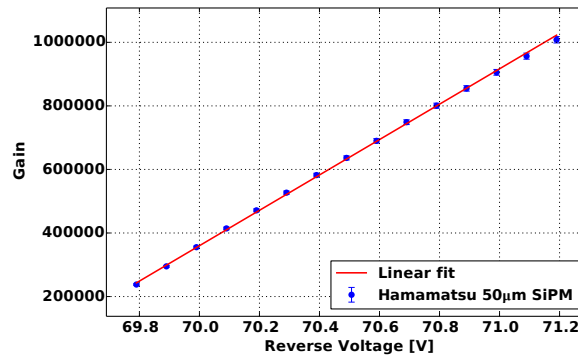


Fig. 6.18: The gain versus voltage measurement and a linear fit to determine the breakdown voltage of the Hamamatsu SiPM.

SiPM is measured as $dV_{bd}/dT \sim 56 \text{ mV/K}$. Knowing from Eq. 5.10, the gain therefore changes with the temperature when using a constant bias voltage. In order to achieve a consistent performance when using the SiPM, a stable temperature environment is required. For the fluctuation of temperature in a small range, a constant gain can be maintained by adjust the bias voltage accordingly.

Gate width

The gate width used for the gain measurement can be determined by parameter sweeping. Fig. 6.19 shows the measured gain of a Hamamatsu SiPM as a function of the gate width used in the measurement at 3 different bias voltages. The gate width is swept between 10 ns and 180 ns with a step of 5 ns. When the gate is equal or smaller than 15 ns, the QDC does not provide any output signal, this is also specified by

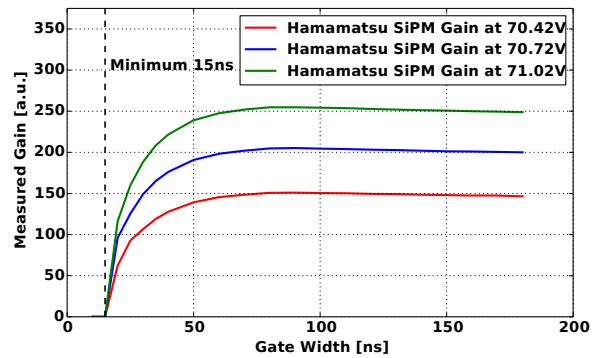


Fig. 6.19: The measured gain versus the gate width at three different bias voltages for the Hamamatsu SiPM.

the data sheet that the QDC starts to integrate the signal only after 15 ns from the leading edge of the gate. The trigger pulse for the LED is placed 17 ns after the gate's leading edge. The measured value reaches plateau when the gate width is equal or larger than 80 ns for all different bias voltages.

According to Tab. 6.3, the calculated single pixel signal decay time constant $\tau_d = 12.6$ ns, assuming the signal recovers to baseline in $5\tau_d$ and adding the LED trigger delay of 17 ns gives 80 ns. Therefore the gate width measurement is in consistent with the signal decay time measured from the static characterization.

The QDC integration gate used in the characterization measurements for Hamamatsu SiPM is 100 ns in order to account for the possible time jitter of the trigger and have a stable gain measurement.

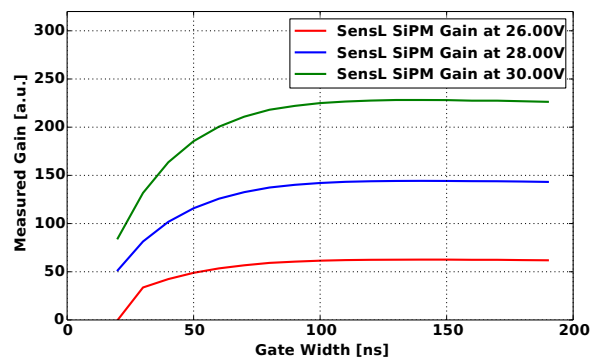


Fig. 6.20: The measured gain versus the gate width at three different bias voltages for the SensL SiPM.

As a comparison, Fig 6.20 shows the gate width scan on the SensL SiPM at three different voltages. The measured gain reaches plateau after the gate width is larger than 130 ns. During the gain experiment, a gate width of 150 ns is used for the SensL SiPM.

The KETEK SiPM PM1150 shows a significantly larger slow component in its signal pulse. This is also indicated by the RC constant calculated in Tab. 6.3. However the compatible gate width value was not used during the measurement, therefore the measured dG/dV shows a large error compared to the C/G measurement.

6.2.2 Fitting Methods for Gain Extraction

An attempt is made to investigate different methods of extracting gain information from the charge area spectrum. One of the main purpose is to have a reliable method which can determine the gain from the spectrum automatically. This is useful since the determination of the breakdown voltage of one device requires the order of 10 measurements at different voltages and for large number of SiPMs it means a significant number of repetitions of the same fitting process. However, due to the variation of performance between devices and at different voltages, the changing of noise of the electronics and the SiPM, the appearance of the spectrum may vary significantly. Therefore sometimes to find a reliable method is not trivial. Three methods are proposed by this thesis and their results are compared.

Multiple Gaussian function fit

The straight forward method to obtain the distance in the spectrum is to fit Gaussian functions to individual peaks and extract the distance by a linear fit on the means from Gaussian functions versus their corresponding number of fired pixels. The result of the method is shown in Fig. 6.17 already. When the peaks are less smeared, the method can obtain reliable results with small uncertainties. In order to perform the fit automatically, a guess on the range of the peak width is required.

Autocorrelation method

The peaks repetition period in QDC unit can be obtained easily by calculating the autocorrelation of the spectrum. If a signal $S(q)$ is periodic with period $q = G$, correlating $S(q)$ with $S(q + m)$ will be at maximum at $m = 0, m = G, m = 2G$, etc. The signal $S(q)$ is the spectrum histogram with q being the QDC unit, the period G is the distance between the peaks, i.e. the gain to be extracted. The autocorrelation of the spectrum denoted by $R(S(q))$ can be efficiently obtained by

$$R(S(q)) = \mathcal{F}^{-1}[\mathcal{F}(S(q)) \cdot \mathcal{F}^*(S(q))] \quad (6.10)$$

where \mathcal{F} denotes the Fast Fourier transform on the data, the asterisk denotes complex conjugate and \mathcal{F}^{-1} denotes the inverse Fast Fourier transform of the data [77]. Therefore the first local maximum where $q > 0$ in the autocorrelation spectrum corresponds to the distance between the peaks in the original spectrum. An example of the charge area spectrum of the Hamamatsu SiPM measured at 70.5 V and its autocorrelation spectrum to find the peak distance is shown in Fig. 6.21.

The autocorrelation methods shows stable result in consistent with the gain obtained from multiple Gaussian function fit. This method does not require any guess on the parameters of the spectrum. Therefore it is useful for the automatic data analysis.

Detector response function fit

Taking into account multiple detector effects, a function $S(n)$ can be constructed to describe the charge area spectrum of the SiPM. The spectrum $S(q)$ is a convolution of the electronics pedestal $P(q)$ and a Poisson distribution based detector signal function $D(q)$.

$$S(q) = P(q) \otimes D(q) \quad (6.11)$$

The electronics pedestal function $P(q)$ is a Gaussian function with its mean and σ determined by the position and width of the first peak in the charge area spectrum. The detector signal function $D(q)$ is described by a Poisson distribution convoluted with the function $Q(q)$ which describes the charge output

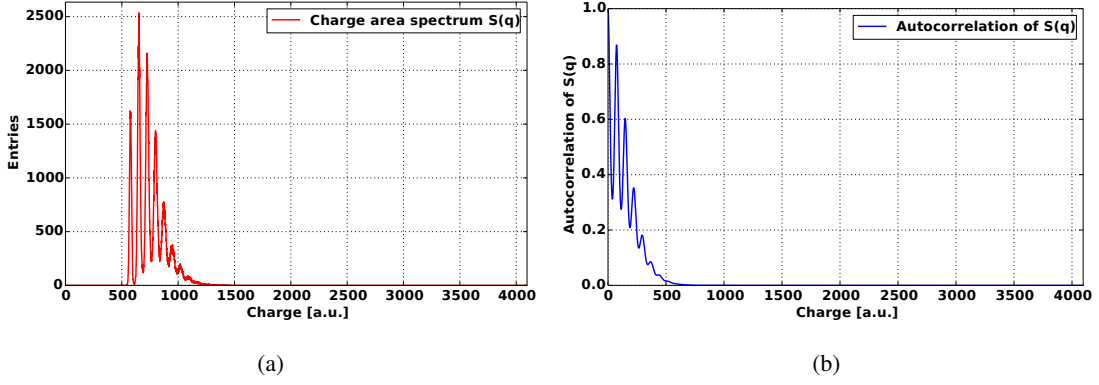


Fig. 6.21: An example of the original charge area spectrum (a) of a Hamamatsu SiPM the its autocorrelation spectrum (b). The position of the first peak in (b) where charge is larger than 0 corresponds to the distance between the peaks in (a).

of one pixel firing. This is a Gaussian function $Q'(q, \mu_G, \sigma_G)$, with μ_G being the gain of the SiPM and σ_G being the excess noise of a pixel, justified by the cross talk probability \mathcal{X} ($0 < \mathcal{X} < 1$):

$$Q'(q) = \frac{Q(q) + \mathcal{X}Q(q)^2 + \mathcal{X}^2Q(q)^3 + \dots}{1 + \mathcal{X} + \mathcal{X}^2 + \dots} = Q(q) \frac{1 - \mathcal{X}}{1 - \mathcal{X}Q(q)} \quad (6.12)$$

Using the convolution theorem, the Fourier transform of the detector signal function $D(q)$ can be given as :

$$\mathcal{F}(D(q)) = \exp(-N_{ph}) \sum_0^{\infty} \frac{N_{ph}^n}{n!} \mathcal{F}(Q'(q))^n = \exp[N_{ph} \cdot (\mathcal{F}(Q'(q)) - 1)] \quad (6.13)$$

where N_{ph} is the mean number of photons of the illumination light. In the end, the detector response function is given by:

$$S(q) = \mathcal{F}^{-1} \{ \mathcal{F}[P(q)] \cdot \mathcal{F}[D(q)] \} = \mathcal{F}^{-1} \{ \mathcal{F}[P(q)] \cdot \exp[N_{ph} \cdot (\mathcal{F}(Q'(q)) - 1)] \} \quad (6.14)$$

In order to fit the detector response function to the spectrum, following initial guess of the parameters are required:

- 0 pe. peak position and pedestal noise, this is the mean and σ of the Gaussian function $P(q)$
- Mean of the Poisson distribution (N_{ph}), which corresponds to the number of detected photon.
- The cross talk probability \mathcal{X}
- The pixel excess noise, this is σ of the Gaussian function $Q(q)$.
- The gain, this is the mean of the Gaussian function $Q(q)$

The detector response function fit is sensitive to the quality of the spectrum and requires a reasonable initial guess of the parameters for the fitting process to converge. Also, the function has not taken afterpulses into account. Nevertheless, it provides a comprehensive analysis of the measured spectrum.

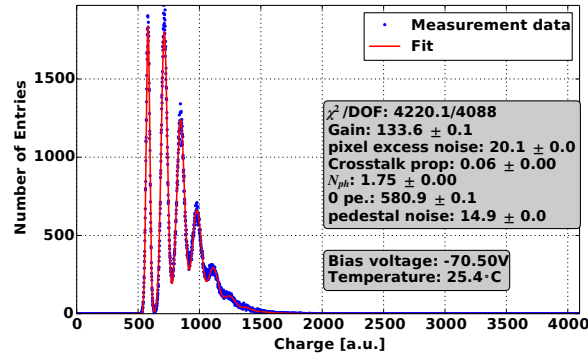


Fig. 6.22: An example of fitting the detector response function to the signal area spectrum measurement. The cross talk probability of the detector can be obtained together with the gain.

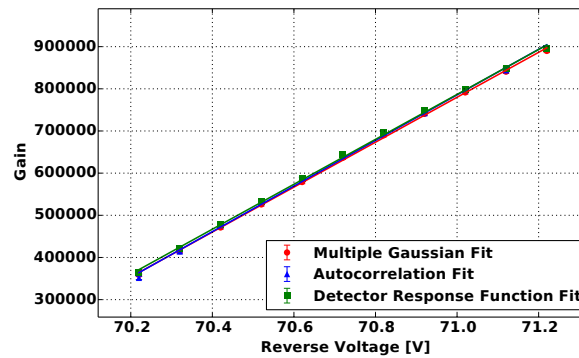


Fig. 6.23: The three different fitting methods were performed on the same set of data measured using a Hamamatsu SiPM.

Tab. 6.4: Results of two different fitting methods

	Multiple Gaussian	Autocorrelation	Detector Response Function
V_{bd}^G [V]	69.54 ± 0.03	69.55 ± 0.03	69.52 ± 0.03
dG/dV [$\times 10^5 \text{ V}^{-1}$]	5.50 ± 0.08	5.57 ± 0.07	5.49 ± 0.08

Comparison

The three fitting methods are used on the same set of data to extract gain and its dependence on the bias voltages measured with a Hamamatsu SiPM. The result is shown in Fig 6.23. The obtained V_{bd}^G and dG/dV is shown in Tab. 6.4. Due to the limited operating voltage range of the Hamamatsu SiPM, the uncertainty of the breakdown voltage obtained from the linear fit is not possible to be reduced below 0.5 V. However by repeating the experiment in the same condition, the error of the breakdown voltage is estimated at the level of 30 mV. The breakdown voltages obtained using the three methods are consistent within the uncertainty. The gain dependence on the voltage is consistent within 2%.

The cross talk probability extracted by the detector response fit for the detectors is shown in the next

section in comparison with the noise probability measured by other methods.

6.2.3 Noise

The noise characteristic of the SiPM includes the uncorrelated noise (DCR) and pixel discharging correlated noise (cross talk and afterpulses). Both of which can be measured using the same setup that is described in Fig. 6.13 with the LED turned off.

The occurrence of a dark count event is a Poisson process, and the distribution of time interval between consecutive dark counts is described by the exponential distribution. Therefore, if the charge integration interval is Δt , the probability of *not* getting any pixel firing signal within the time interval (denoted by $P_0(\Delta t)$) is:

$$P_0(\Delta t) = \exp(-\text{DCR} \cdot \Delta t) \quad (6.15)$$

This relation is used to measure the DCR of a SiPM.

Due to the fluctuation of the gain and the electronic noise from the readout circuit, 0.5 level of the gain is normally used as a threshold to determine if a pixel firing signal is detected. In addition, since the dark count event happens randomly with respect to the gate of QDC for charge integration, and the pixel firing signal is not a δ function, the effect of integrating partially the signal is investigated. This is done by triggering the pixels with LED light and changing the delay time between the light pulse with respect to the leading edge of the gate. If only partial of the pixel's firing signal is integrated, the measured gain is reduced. An effective gate width can be defined as the width in which the measured gain is larger than half of the maximum value. Fig. 6.24 shows the measured gain of a Hamamatsu SiPM at 70.72 V with a gate width of 100 ns as a function of the trigger delay between the LED trigger and the leading edge of the gate. The effective width is 102 ns. This is used as Δt in the Eq. 6.15 to calculate the DCR. For the SensL SiPM with longer pixel recharging time, the effective width for a gate width of 150 ns is 150 ns (see in the Fig. 6.25).

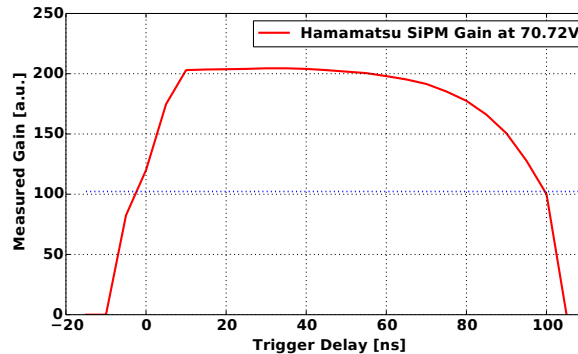


Fig. 6.24: The measured gain versus delay time between the LED trigger and the leading edge of the gate, the measurement is performed at a fixed bias voltage on a Hamamatsu SiPM using gate width of 100 ns. The effective gate width is 102 ns.

The pulse area spectrum measured in dark environment of the Hamamatsu SiPM is shown in Fig. 6.26. The bias voltage used is 70.5 V and the temperature is 25°C. The probability of not getting any pixel fired in the effective integration interval is the fraction of entries with charge below the 0.5 pixel threshold. The DCR at 0.5 pixel threshold can therefore be calculated using Eq. 6.15.

Fig. 6.27 shows the DCR measured as a function of the excess bias voltage for the SiPMs from different producers. The unit used for the DCR is thousand counts per second (kcps). The DCR of the devices

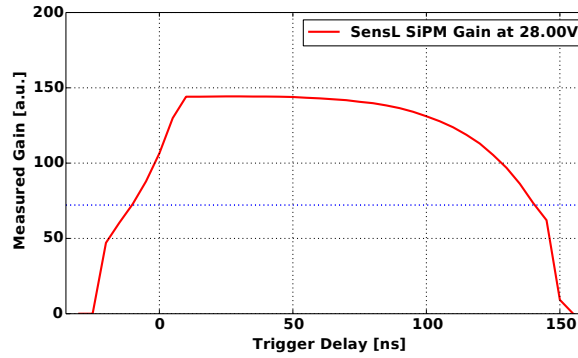


Fig. 6.25: The measured gain versus delay time between the LED trigger and the leading edge of the gate, the measurement is performed at a fixed bias voltage on a SensL SiPM using gate width of 150 ns. The effective gate width is 150 ns.

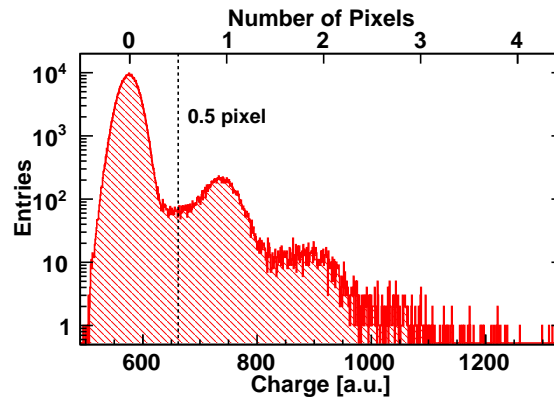


Fig. 6.26: Pulse area spectrum of the Hamamatsu SiPM measured in dark at 70.5 V and 25 °C. Counts with pulse area larger than $n_{pix} = 0.5$ are considered as dark counts.

ranges from ~ 200 kcps up to 1 Mcps. The increase of DCR with the excess bias voltage can be explained by the combination of the increase of avalanche triggering probability with the voltage and the tunneling effect to generate free charge carriers. At lower excess bias voltage, due to the small gain and limited amplification factor, the tail of the first peak in Fig. 6.26 may increase the counts above the 0.5 pixel threshold, results in an over estimation of the DCR. This effect is considered as the uncertainty of the measurement, and therefore included in the calculation of the error bars. This explains the relatively larger error of the DCR at the lowest excess bias voltage in Fig. 6.27.

A SiPM with larger pixels has higher geometric efficiency, thus the total depleted volume in the SiPM is also higher. This explains the 50 μm pixel KETEK SiPM has higher DCR compared to the 25 μm pixel KETEK SiPM. The disparity of DCR for SiPMs from different producers may originate from their own producing processes.

A second threshold is set at 1.5 pixel level where entries above the threshold are considered to have more than one pixel fired. The additional firing pixels may be triggered by cross talk or afterpulses. Thus the fraction of events which have more than one pixel fired can be defined as the correlated noise triggering

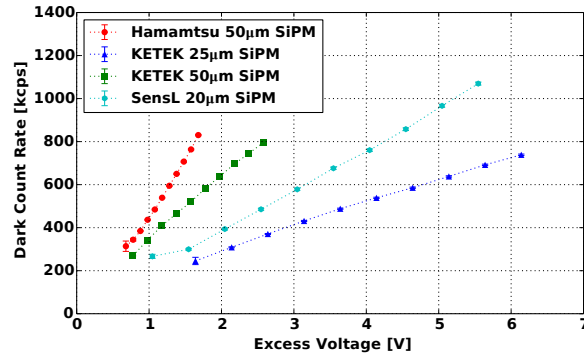


Fig. 6.27: The DCR of the four SiPM samples from different producers plotted as a function of the excess bias voltage.

probability (P_{cn}):

$$P_{cn} = \frac{N_{>1.5pix}}{N_{>0.5pix}} \times 100\% \quad (6.16)$$

where $N_{>0.5pix}$ and $N_{>1.5pix}$ are the number of entries with charge above the 0.5 and 1.5 pixel threshold respectively. When the DCR of the SiPM is sufficiently high, the probability of having two or more dark count events within the integration time is not negligible anymore. Therefore the dark count introduced additional counts are considered as an uncertainty to the calculated correlated noise probability.

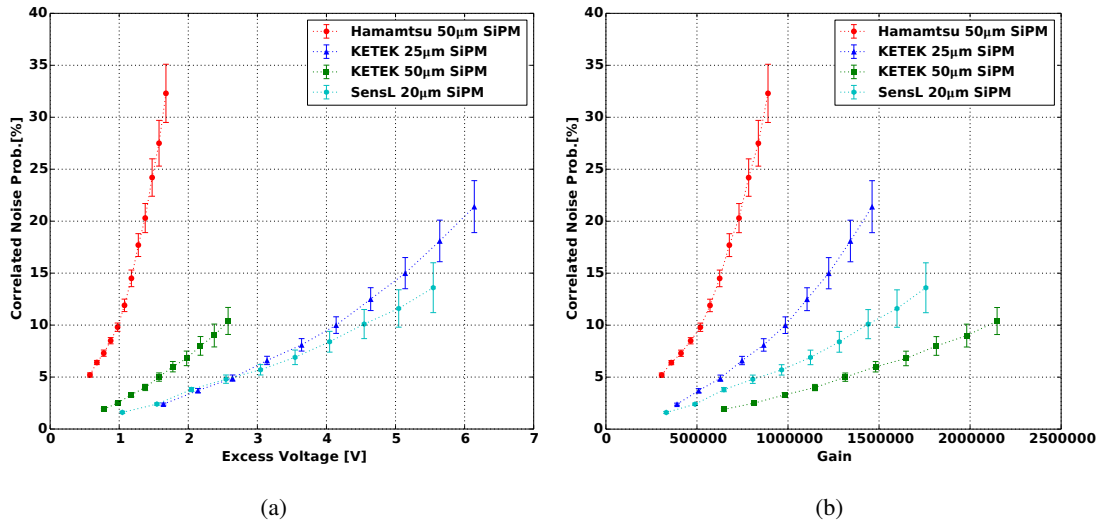


Fig. 6.28: The calculated correlated noise probability of the four SiPM samples from different producers plotted (a) as a function of the excess bias voltage and (b) as a function of the gain.

Fig. 6.28a shows the calculated correlated noise probability as a function of the excess bias voltage. The increasing of the correlated noise probability with the excess bias voltage originates from two factors. First, higher electric field in the SiPM can increase of the avalanche trigger probability, thus it becomes easier for an emitted photon or de-trapped free carrier from pixel discharge to trigger a correlated additional

pixel firing. More importantly, both the number of emitted photon and trapped carrier increases with the gain, thus the correlated noise probability strongly depends on the gain of the SiPM. This can be clearly seen in Fig. 6.28b, where P_{cn} is plotted as a function of the gain. The KETEK devices with different pixel sizes show that larger pixel device have less correlated noise probability than the smaller pixel device at the same gain. The difference originates from the lower cross talk of the large pixel device. Since the emitted photon may need to travel longer distance to trigger a cross talk in the larger pixel device, its total correlated noise probability is lower.

There are other methods of measuring the noise of the SiPM that can be found in [51], where the cross talk and afterpulse probability are measured separately. However, the methods introduced in this section provides a solution in the interest of shorter measuring time and simplified the instrumentation requirements to accomplish the experiment. This is extremely valuable when developing a test bench for an application where large quantity of SiPMs need to be characterized. The fact that the gain, breakdown voltage, DCR and correlated noise probability can be measured in a single data taking of experiment shows great potential for the massive characterization of the SiPMs to be used in the EndoTOFPET-US project. Also, the measured correlated noise probability serves the practical purpose of revealing the noise quality of the SiPM.

6.2.4 Signal Pulse Analysis

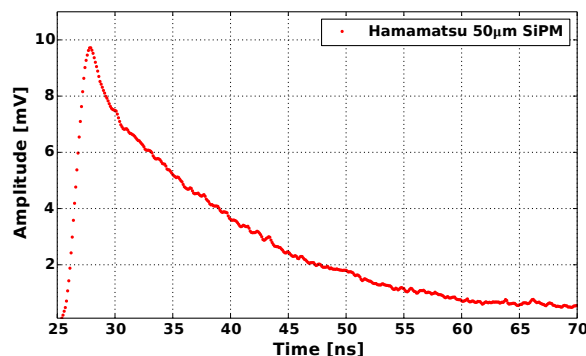


Fig. 6.29: An averaged one pixel firing signal pulse from the Hamamatsu SiPM.

The pulse shape of the SiPM amplified by a factor of 50 is recorded by a Tektronix DPO-7254 scope with 2.5 GHz bandwidth and a sampling rate of 20 Gsamples/second. In order to get the decay time of the signal, an exponential function is fitted to the waveform corresponding to one pixel fired. The SiPM is operated at a nominal voltage where the gain of the device is 7.5×10^5 . More than 100 pulses of one pixel fired signal without any afterpulses are selected from the acquired waveforms, and an averaged signal is used for the fitting. Fig 6.29 shows the averaged one pixel fired signal from the Hamamatsu SiPM, the rise time of the signal is about 1 ns, and the exponential fit between 30 ns and 60 ns gives a signal decay time of 13.6 ± 0.5 ns, the errors is obtained by varying the fitting range in ± 10 ns.

6.3 Summary and Comparison

6.3.1 Quenching resistance

The quench resistances of the SiPM samples which are determined in two different ways are shown in Tab. 6.5. Values measured from the forward IV measurement are in general larger than the values estimated by the C/G measurement. The forward IV measurement shows large systematic uncertainty due to the large current measuring range and therefore a frequent changing in measuring scales of the equipment. The values are consistent within the 20% level, and the overall agreement are considered satisfactory.

Tab. 6.5: Comparison of R_q^{IV} and R_q^{CV}

Name	R_q^{IV} [k Ω]	R_q^{CV} [k Ω]
MPPC S10362-11-050C	142 \pm 2	135 \pm 4
KETEK PM1125	817 \pm 16	670 \pm 2
KETEK PM1150	517 \pm 7	454 \pm 1
SensL MicroFB-10020	482 \pm 10	371 \pm 4

6.3.2 Breakdown Voltage

The breakdown voltages of the SiPM samples are determined in two ways and their values are compared in Tab. 6.6. Since the three different fitting methods have obtained identical breakdown voltage from the same set of data as shown in section 6.2.2, only values obtained by the multiple Gaussian function fit is used to represent V_{bd}^G . The values show agreement within 2%. However the breakdown voltage determined by gain measurement has higher precision, an important practical feature in operating the SiPM. Therefore the voltage dependent gain measurement is considered a crucial procedure in the characterization of the SiPM. On the other hand, since the current voltage scan around the breakdown voltage region of the SiPM can be performed quickly, it is useful in the study of the temperature dependence of the breakdown voltage. The breakdown voltage value extracted by the current voltage scan is in average larger and may not refer to the same condition as the one defined by the gain measurement. Further studies are required in order to understand their differences.

Tab. 6.6: Comparison of V_{bd}^{IV} and V_{bd}^G

Name	V_{bd}^{IV} [V]	V_{bd}^G [V]
MPPC S10362-11-050C	69.6 \pm 0.1	69.54 \pm 0.03
KETEK PM1125	25.4 \pm 0.1	24.86 \pm 0.03
KETEK PM1150	25.4 \pm 0.1	25.22 \pm 0.01
SensL MicroFB-10020	24.7 \pm 0.2	24.45 \pm 0.01

6.3.3 Gain and Pixel capacitance

The pixel capacitance obtained by the C/G-frequency measurement below the breakdown voltage of the SiPM can be compared to the calculated dG/dV from the gain measurement above the breakdown.

Table 6.7 provides a comparison of the values for the SiPM samples. In average the capacitance determined via C/G-frequency measurement is larger than that extracted by the gain measurement. This systematic difference is considered mainly due to the absolute calibration of the gain measurement. However, the fact that SiPMs from KETEK and SensL do not show indication of full depletion in the CV measurement (c.f. Fig. 6.10) may suggest that their C_{pix}^{CV} values have large errors which are hard to estimate. In addition, the dG/dV measured by the gain measurement has more practical use for the SiPM operation, therefore it is also considered an essential figure of merit of the SiPM. The KETEK PM1150 is not measured with a compatible gate, therefore a large error is observed between C_{pix}^G and C_{pix}^{CV} .

Tab. 6.7: Comparison of C_{pix}^{CV} with C_{pix}^G

Name	C_{pix}^{CV} [fF]	dG/dV [$\times 10^3/V$]	C_{pix}^G [fF]
MPPC S10362-11-050C	93.2 ± 0.2	550 ± 8	88.0 ± 1.1
KETEK PM1125	51.6 ± 0.8	238.1 ± 0.5	38.1 ± 0.1
KETEK PM1150	250 ± 34	834 ± 2	133.4 ± 0.3
SensL MicroFB-10020	64.2 ± 0.1	316.8 ± 0.6	50.7 ± 0.1

6.3.4 Signal Decay Time

The signal decay time can be determined from the RC constant using C/G measurement, or from the waveform analysis with an exponential function fit. The practical purpose of getting the signal decay time is to determine the charge integration time in the gain measurement. However it is a safer way to perform a gate width scan as shown in the previous section to determine the proper integration gate.

6.3.5 Noise

The comparison of DCR and correlated noise probability between different SiPMs is discussed in the section 6.2.3. Here only the comparison between the cross talk obtained by detector response function fit and the correlated noise probability is shown in Fig. 6.30.

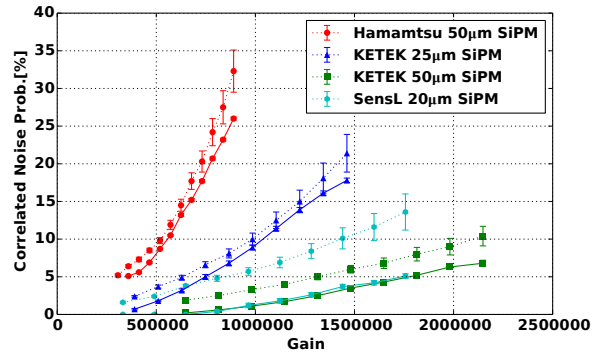


Fig. 6.30: The correlated noise probability measured by pulse area spectrum described in section 6.2.3 (dotted line) is compared to the cross talk probability obtained by the detector response function fit described in 6.2.2 (solid line). Both of which are plotted as a function of the gain.

The cross talk probability from the detector response function fit is systematically lower than P_{cn} for all measured devices. This is expected since the correlated noise probability includes the contribution from afterpulses which the detector response fit does not take into account. The difference between the correlated noise probability and the cross talk probability obtained by the detector response fit is used as an indication of the afterpulse probability in the simulation described in Chapter 7.

The method of measuring correlated noise probability introduced in this chapter provides a fast way of estimating the correlated noise level of the SiPM. Due to its simplified assumptions, namely any additional pulses more than one pixel fired within the charge integration gate are contributed by the correlated noise, the parameter deviates significantly from the real correlated noise probability. This happens when the DCR of the device is significantly high and the probability of having two dark count events in the charge integration gate is not negligible anymore. Other methods of measuring the cross talk and afterpulses are described in [51], the use of low threshold discriminator and pulse counter requires a reconnection of the equipment, which will significantly extend the measuring time. Therefore the method is not used for the quality assurance test for the characterization of a large number of SiPMs to be commissioned in the EndoTOFPET-US detector.

Chapter 7

THE DIGITAL SiPM

Although each pixel of a silicon photomultiplier (SiPM) operates as a binary device, conventional SiPM combines the charge output of multiple single photon avalanche diodes (SPADs) into a single analog output signal. The next logical step in the SiPM development is to embed readout circuitry into the detector chip. In practice, this is done by integrating the SPAD design into an existing CMOS process, which is developed by the microelectronics industry to provide reliable and reproducible electronics at low cost. The so-called digital SiPM (dSiPM) design has the detector on the same substrate with complex electronics that can have functionalities of signal quenching, data storing or data treatment etc.

The dSiPM can provide improved performance and new features compared to the conventional analog SiPM. With a counter circuitry connected to each SPAD, the dSiPM is able to count photon more accurately without the need of an additional gain calibration. As stated previously, the Gaussian distributed jitter in the signal delay time is one of the main sources which dominates the time resolution of the detector system. An on-chip TDC can record the pixel firing time with much reduced signal routing delay, and thus greatly improves the time resolution. The improvements of energy counting and time resolution are especially attractive for positron emission tomography (PET) applications. In addition, a more complex circuitry can be implemented to realize detector functionalities such as pixel masking for the dark count rate (DCR) suppression, active signal quenching for the correlated noise suppression, improved high counting rate capability, and application specific triggering logic for the data readout.

However, the state of the art dSiPM is still limited by many aspects. The implementation of SPAD in a CMOS process faces severe constraints in designing an effective SPAD [78]. Placing the circuitry close to the SPAD may reduce the fill factor, which result in lower photon detection efficiency (PDE). The CMOS process is mainly developed for the transistor fabrication, thus the impurities and defects introduced by the fabrication process, which does not affect the performance of a transistor, can dramatically increase the DCR of a dSiPM. These are the problems still to be solved in future development of this technology. However, the detail of the design and fabrication of a dSiPM is not in the scope of this thesis. The content of this chapter is limited to the measurement result of a dSiPM prototype. The Multi-channel Digital SiPM (MD-SiPM), which features multiple on-chip TDCs and a unique trigger logic, is developed for the EndoTOFPET-US project by Delft University of Technology. Its prototype is characterized, and its performance is compared to a conventional SiPM (MPPC S10362-11-050C) with a similar detector form factor. The result is presented in this chapter.

7.1 The MD-SiPM Prototype

The MD-SiPM is fabricated using a $0.35\ \mu\text{m}$ high voltage CMOS process [36]. The sensor features 416 (16×26) SPADs, and a total detector area of $800 \times 780\ \mu\text{m}^2$. The single pixel size is $50 \times 30\ \mu\text{m}^2$ with a

fill factor of 57%. The PDE of the sensor operating at 2.5 V excess bias is 12.5%, and can be up to 17% at 4 V excess bias. Each pixel consists of a SPAD with a 1-bit counter for pixel firing registration and circuits for pixel masking and signal shaping. The signal from a pixel is routed directly to one of the 3 TDCs shared by a column of pixels in an interlaced configuration. In total 48 TDCs are available for the sensor. Fig 7.1 shows the connection configuration between the pixels and the on chip TDCs.

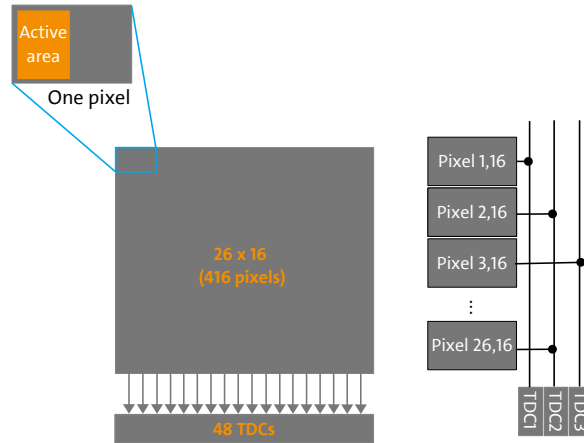


Fig. 7.1: A diagram shows the connection configuration of the MD-SiPM prototype. The fill factor is the ratio between active area of the total area of a pixel. The rest of the area is occupied by the electronics.

The chip operates in self-triggered mode with framed readout. The start signal pulse sent to the device clears all pixel counters and starts the TDC clock. A firing SPAD due to photon detection or dark count, causes the 1-bit counter's increment, and stops the connected TDC, recording the pixel firing time. The 1-bit counter records only the first firing of a pixel and therefore eliminates afterpulses completely. At the end of the frame, the counted number of fired pixels and TDC data are read out. The frame acquisition time can be defined by the user before starting a measurement.

7.1.1 Dark Count Rate

The breakdown voltage of the MD-SiPM sample is at 19.5 V, and the device can be operated in a range of 0.5 V to 4 V excess above the breakdown. The dark count rate (DCR) of the device is measured as a function of excess bias voltage. The measurement is performed in a light-tight environment. Eq. 6.15 also applies to the DCR measurement of the MD-SiPM, in which Δt is the frame acquisition time and P_0 is the ratio of frames without dark counts to the total number of frames. The frame acquisition time used for the DCR measurement is 100 ns. In contrast to the conventional SiPM, the DCR of the MD-SiPM can be measured on a pixel-by-pixel basis, and the overall DCR of the device is the sum of all pixels' DCR. Fig. 7.2 shows a DCR distribution map in the sensor measured at 2.5 V excess bias and room temperature.

The MD-SiPM provides possibility to selectively deactivate (masking) individual pixels which is used to suppress the overall DCR of the sensor. The DCR distribution map shows that few pixels contribute significantly to the total DCR of the sensor. Switching them off can largely reduce the total DCR at the cost of reducing the PDE at the same time. The trend of the trading off between DCR and relative PDE (to the PDE value when all pixels are activated) at 2.5 V excess bias and room temperature is shown in Fig. 7.3. Small amount of pixel masking (<30%) have larger impact on the reduction of DCR than the loss of PDE.

Table 7.1 shows the DCR per unit detector area of the MD-SiPM and that of the MPPC S10362-11-050C from Hamamatsu. Both sensor features $\sim 1 \text{ mm}^2$ detector area. The MD-SiPM has significantly larger

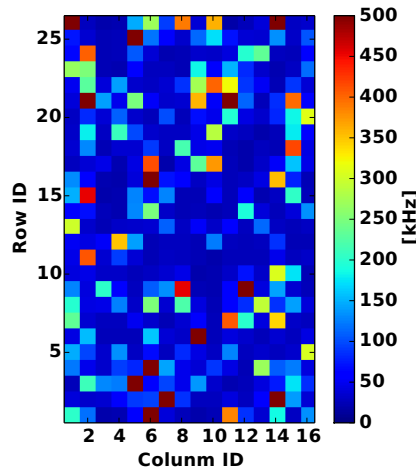


Fig. 7.2: The distribution of DCR among the pixels in a MD-SiPM sensor.

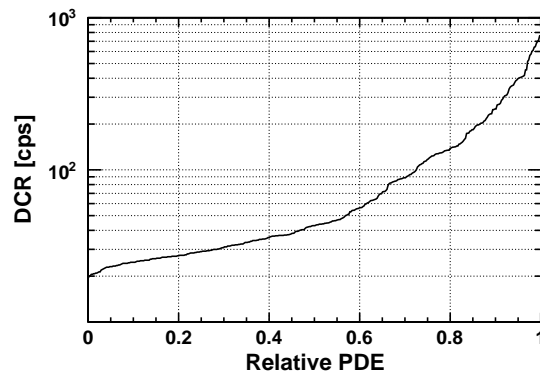


Fig. 7.3: The MD-SiPM's total DCR versus relative PDE. When all pixels are activated, the relative PDE is one.

DCR mainly due to the limitations from fabrication process. However, the pixel masking function can help in moderating the DCR. Fig. 7.4 shows the DCR of the MD-SiPM with different percentage of pixel masking as a function of the excess bias voltage. The DCR of the MPPC S10362-11-050C is also plotted in comparison.

7.1.2 Trigger Validation

Operating in self-triggered mode with a fixed frame acquisition time, dark counts cause pixel firing and therefore reduce the dynamic range. They also introduce fake TDC activations whose time stamp is not the arrival time of a photon from the scintillation light. The occurrence of a scintillation event in PET application is random relative to the acquisition frame. Therefore a validation is required to periodically check the pixel and TDC activations and reset those who are introduced by dark counts. The ‘‘Smart Reset’’ (SR) function of the chip is implemented for this purpose. The 48 TDCs on the chip give the

Tab. 7.1: DCR per unit detector area of a MPPC and a MD-SiPM

	MPPC	MD-SiPM
DCR [$\text{cps}/\mu\text{m}^2$]	0.5	50

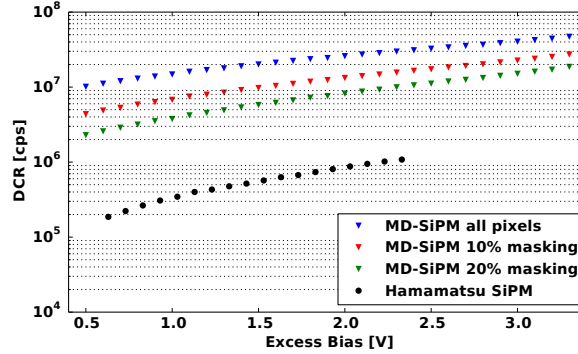


Fig. 7.4: The dependence of MD-SiPM’s total DCR on excess bias voltage with different percentage of pixel masking. The DCR of the MPPC sample as a function of the excess bias voltage.

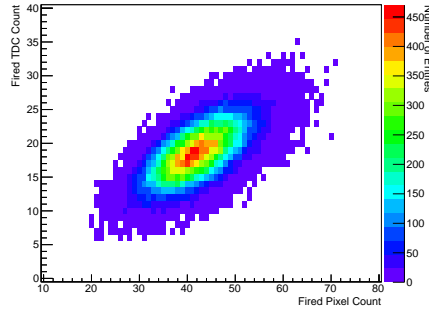


Fig. 7.5: Number of activated TDCs as a function of number of fired pixels in a frame of 400 ns measured in dark. Because of the shared TDC configuration, a mean number of 42 dark counts have triggered a mean number of 19 TDCs per frame.

device the capability of recording 48 timing information corresponding to the earliest fired pixels. For a low number of photons, the number of TDC measurements is proportional to the accumulated number of pixel fired (shown in Fig. 7.5). Due to the electronic scheme of the chip, it is faster to read out the number of activated TDCs without influencing the pixel operation. The scintillation light from a LYSO crystal (light yield of 32000 photons/MeV with a decay time of 40 ns [79]) is expected to cause a burst of pixels and TDC activations, while the dark count accumulation is much slower. Therefore an energy equivalent threshold can be set on the number of activated TDCs to distinguish a scintillating event from accumulated dark counts in a frame.

When using the number of occupied TDCs as threshold, it is necessary that the pixel’s sensitive time longer than TDCs’ sensitive time, so that the chip has a uniform energy response to a scintillating event which happens during the later part of a frame (cf. Fig. 7.6).

Fig. 7.7 shows the functionality test for the SR function. The plot shows dark counts for different

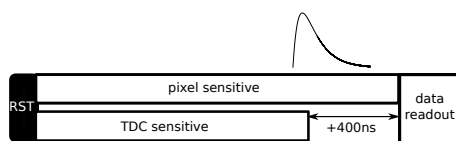


Fig. 7.6: The diagram shows the timing of pixels and the TDCs sensitive time in a frame acquisition time. When a scintillation event happens in the later part of a frame, multiple TDCs may have recorded the time of arrival of the early photons, an extended pixel working time of 400 ns allows the device to record the whole scintillation process.

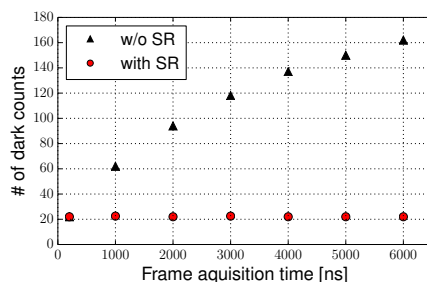


Fig. 7.7: Trigger validation functionality test, the plot shows the “Smart Reset” (SR) function effectively keeps dark counts independent from the frame acquisition time.

frame acquisition times measured with and without SR function. The SR check interval is set to 200 ns in the measurement. Without SR function, 160 out of 416 pixels are activated by dark count for a $6\ \mu\text{s}$ frame acquisition time. While the SR function keeps the total dark count independent from the length of frame acquisition time. The effectiveness of the SR reset in the detection of a scintillation event will be shown in the section 7.1.4

7.1.3 MD-SiPM Response Function

Due to the limited number of pixels of the sensor, the number of recorded photons is not proportional to the number of incident photons. Additionally, with the self-triggered frame readout scheme, a pedestal of dark count further reduces the dynamic range of the sensor. Thus for a linear energy response, it is necessary to correct the detector non-linearity.

A Monte Carlo approach is chosen for the correction of the detected photons by simulating the detector’s response to different number of incident photons and producing a detector response curve. The number of fired pixels in response to a given number of incident photons in a given frame acquisition time can be predicted. The developed Monte Carlo simulation takes all known characteristics of the prototype MD-SiPM into account, including the pixel-by-pixel DCR, pixel masking, pixel to TDC connection scheme and the self-triggered readout logic. Fig 7.8 shows the comparison of simulated frames of the measurement taken by a MD-SiPM in the dark. The slight discrepancy between simulated data and measurements on the activated TDC counts is due to the assumed uniformly distributed dark counts in the simulation while in reality noisy pixels are not uniformly distributed, therefore the probability of triggering each of the 48 TDCs differs. However the non-uniformity of TDC activation probability has no influence on energy response correction.

Fig 7.9 shows the simulated response curve of the MD-SiPM using 800 ns frame acquisition time. The detector PDE at 2.5 V excess bias is 12.5% [36] and total DCR is 50 Mcps. The simulated incident photons are uniformly distributed over the detector area. A probability density function is used to described the

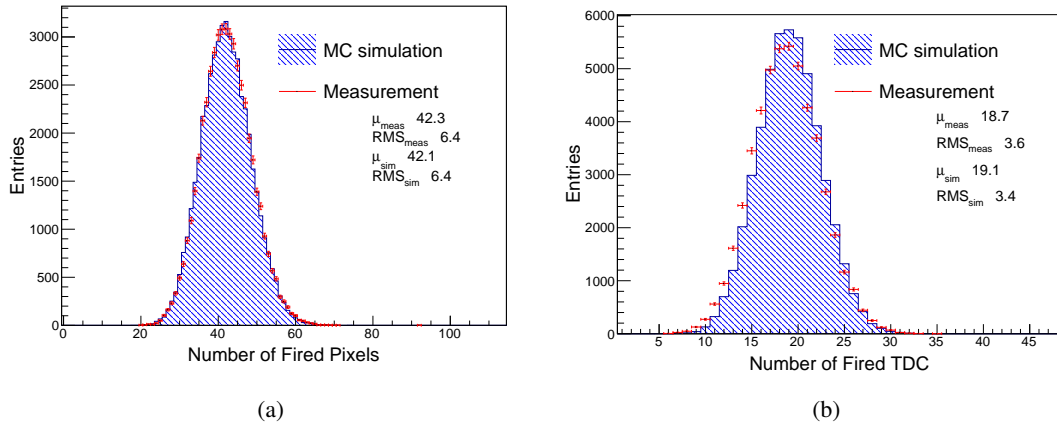


Fig. 7.8: Comparison between 50,000 simulated frames without incident photon and a measurement taken by a MD-SiPM in the dark. (a) shows the comparison between number of fired pixels and (b) shows the comparison between number of triggered TDCs.

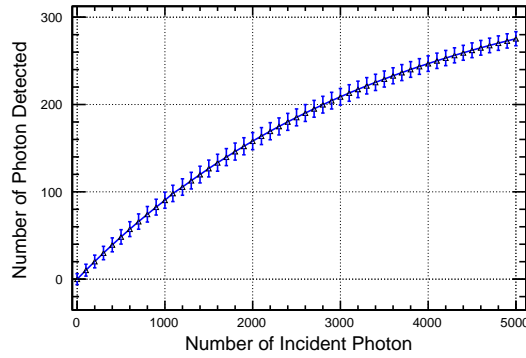


Fig. 7.9: The MC simulation and digitization tool predicts the detector response to different number of incident photons fall on detector surface. Simulation result points are connected by a line to guide the eye.

arrival time of the photons:

$$f(t) = \frac{\exp(-\frac{t}{\tau_d}) - \exp(-\frac{t}{\tau_r})}{\tau_d - \tau_r} \quad (7.1)$$

where τ_r and τ_d is the rise time and decay time of the photon flux. For a LYSO crystal, 100 ps and 40 ns are used for the rise and decay time respectively. A pedestal of 42 dark counts in the 800 ns frame acquisition time which is used for scintillator measurement is subtracted from the curve.

7.1.4 Scintillator Measurement

The MD-SiPM is coupled to a $1 \times 1 \times 15 \text{ mm}^3$ LYSO crystal produced by Hilger [79] to measure the photon energy spectrum of a ^{22}Na and ^{137}Cs source. Due to the geometry mismatch between the crystal and the MD-SiPM, only 62.4% of the crystal's surface area is covered by the MD-SiPM as shown in Fig. 7.10. The crystal is held by a plastic holder and is in dry contact with the sensor. There is no wrapping

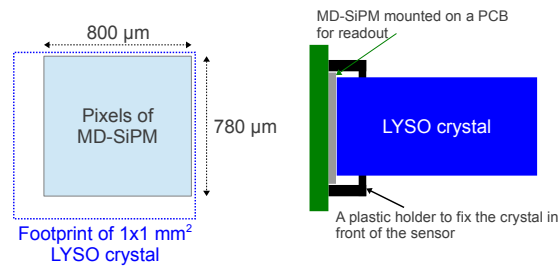


Fig. 7.10

or coating treatment to the crystal. A frame acquisition time of 800 ns is used in the measurement. The number of fired pixels and activated TDCs together with their recorded time stamps in each frame are stored.

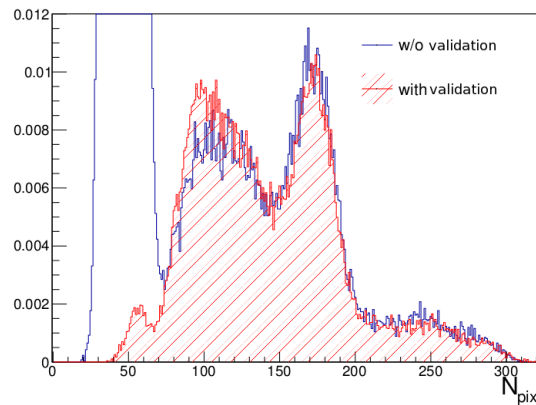


Fig. 7.11

First, the MD-SiPM is used to readout the scintillation light from the LYSO crystal irradiated by 511 keV gamma photon from a ^{22}Na source with and without the SR function activated. Fig. 7.11 shows that after applying the SR function with a threshold of 30 TDCs, frames with a valid scintillation event are effectively selected and the multiplicity of noise events is significantly reduced.

Fig. 7.12 shows a spectrum of ^{22}Na source after correcting for the non-linearity. The energy resolution at Full-Width-Half-Maximum (FWHM) for the 511 keV photo-peak is 33.9%. Fig. 7.13 shows the photo-peak position of 511 keV, 1275 keV from ^{22}Na and 661.7 keV from ^{137}Cs after the non-linearity correction is applied to the spectra. The poor energy resolution is probably a result of the low light yield which is caused by lack of wrapping treatment on the crystal and dry contact between the crystal and the MD-SiPM as well as the geometry mismatch between the crystal and the MD-SiPM. The final implementation of the MD-SiPM to the internal probe of the EndoTOFPET-US detector will have a dedicated crystal for the MD-SiPM, and well defined gluing procedure to attach the crystal to the wire bonded MD-SiPM chip. The required crystal and procedure is not available at the time when this thesis is written.

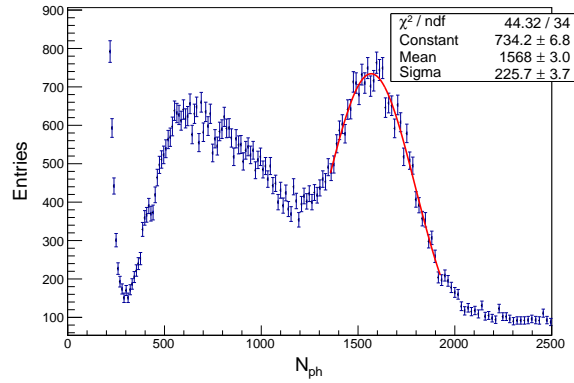


Fig. 7.12: Light yield spectrum obtain by MD-SiPM coupled with a $1 \times 1 \times 15 \text{ mm}^3$ LYSO in the unit of incident photons fall on the surface of the detector. The spectrum is corrected for the non-linear response using the MC-simulation curve described in section 7.1.3.

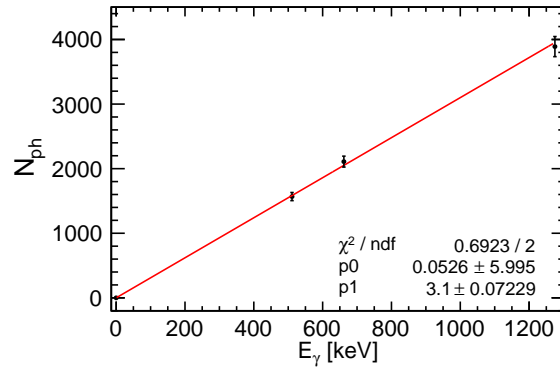


Fig. 7.13: The system's response to the photo-peak after non-linear correction for the gamma emission of ^{22}Na (511 keV and 1275 keV) and ^{137}Cs (661.7 keV)

7.2 Comparison between MD-SiPM and MPPC

A direct comparison is made between the MD-SiPM and a conventional SiPM, the MPPC S10362-11-050C from Hamamtsu. Their characteristics and their performance on reading out the LYSO crystal is compared since both sensors are potential candidates for PET applications.

7.2.1 Scintillation measurement of the MPPC

The $1 \times 1 \times 15 \text{ mm}^3$ LYSO crystal used in the radiation measurement for the MD-SiPM is coupled to the MPPC. The crystal is used without wrapping or coating treatment and is in dry contact with the MPPC. Energy spectra of ^{22}Na and ^{137}Cs source are measured. The MPPC is operated at 1.4 V excess bias at 20°C . The output signal from MPPC is duplicated by a Lecroy 428F linear FAN-IN/FAN-OUT model. One of the two outputs is fed to a low threshold discriminator from CAEN (Model N96) to create a gate of 600 ns for the QDC. The other output from the FAN-IN/FAN-OUT model is delayed by about 30 ns using

Tab. 7.2: Figures of Merit used for the MPPC Response Simulation

PDE	23%
DCR	450 kcps
cross talk	10.5%
after pulse	17.7%
recovery time	13.5 ns

KX15 coaxial cable and then integrated by the QDC.

The simulation program used to simulate MD-SiPM's behavior is modified to simulate the response of the MPPC. The 600 ns charge integration time is used as the frame acquisition time. MPPC's pixel cross talk is taken into account by randomly firing one of the 4 direct neighbor pixels with a certain probability if a pixel was fired by a photon. Pixel's recovery time and its re-firing within the charge integration time has to be taken into account since the integration time is much longer than the pixel recharging time constant. A $t_0 = 5$ ns dead time is implemented after a pixel's firing [80]. The gain of the pixel then recovers following the exponential function with a recharging time constant of $\tau_r = 13.5$ ns, which is measured by the scope in Chapter 6.2.4. The exponential function used in the simulation program is:

$$G(t) = G_0 \cdot (1 - e^{-(t-t_0)/\tau_r}) \quad (7.2)$$

where G_0 is the initial gain of the pixel, and $G(t)$ is the gain of the pixel at time t (in the unit of nanosecond) after the the pixel's firing.

Afterpulses of the MPPC are also taken into account in the simulation. After a pixel discharging is triggered, an additional firing of the same pixel is introduced with its firing time uniformly distributed in a time interval after the initial firing. The ratio between the additional number of pixel firing due to afterpulsing and the total number of pixel firing is the experimentally measured afterpulse probability. The input parameters for the simulation is shown in the Tab. 7.2. The DCR is measured by the characterization measurements described in Chapter 6.2.4, the cross talk probability is the number extracted with the detector response fit from Chapter 6.2.2. The afterpulse probability is calculated by taking the difference between the correlated noise probability and the cross talk probability. The PDE of the MPPC is taken from [51].

Fig. 7.14 shows the energy spectra of the two sources after non-linear detector response correction.

7.2.2 Comparison

The operating voltage that is used for the MPPC is 1.4 V above the breakdown voltage, and the gain of the MPPC is 7.48×10^5 . The MD-SiPM prototype is operated at 22.5 V which corresponds to 2.5 V above the breakdown voltage.

The MPPC has a DCR of $0.5 \text{ cps}/\mu\text{m}^2$ (450 kcps in total) at its nominal operating voltage while the MD-SiPM has $50 \text{ cps}/\mu\text{m}^2$ (50 Mcps in total). Both devices are operated at 20°C. In the gamma spectroscopy measurement, given the same signal integration time window, the number of pixels fired by noise for the MPPC is negligible. While in the case of the MD-SiPM, on average 42 dark counts per $6 \mu\text{s}$ are accumulated if a "Smart Reset" validation of 800 ns is used. This reduces the dynamic range of the MD-SiPM from 416 to about 370 pixels.

Both sensors show strong non-linear response to the scintillation light from the LYSO crystal. The MD-SiPM has 416 pixels and each pixel can be used only once per acquisition frame. The MPPC has 400 pixels and a pixel can fire multiple times with a recovery time constant of 13.5 ns. Due to this fact, a stronger non-linear behavior of the MD-SiPM compared to the MPPC is expected. The MPPC has a

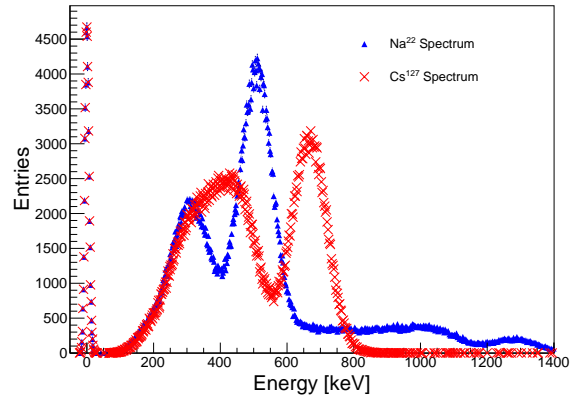


Fig. 7.14: Na^{22} and Cs^{137} gamma emission spectra measured by a MPPC coupled to LYSO crystal. The spectra are corrected for the non-linear response of the detector.

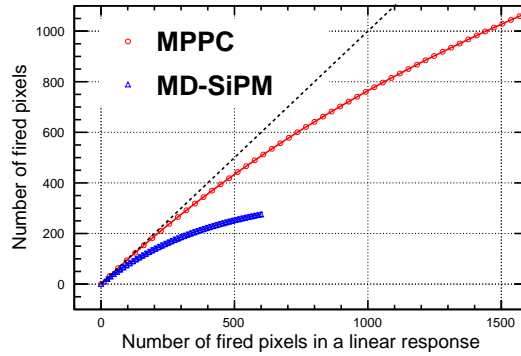


Fig. 7.15: MC simulation predicted detector response curve of MPPC and the MD-SiPM. The dash line shows the ideal linear response.

PDE of 23% (excluding cross talk and afterpulses), which is almost twice of the MD-SiPM's 12.5% PDE. Fig. 7.15 shows the photon detection response curve of the MPPC and MD-SiPM, and their deviations from an ideal linear detector, respectively. The result is obtained by the MC simulation program. Table 7.4 summarizes the detector response to 511 keV of the two systems. The detector's non-linear effect is defined as the decrease of fired pixels to an ideal linear response in percentage.

The energy resolution of different photo peaks at Full-Width Half-Maximum (FWHM) measured by two sensors are shown in Tab. 7.3. All numbers are obtained after the non-linearity correction to the spectra. The energy resolution for 511 keV photons at FWHM is 23.2% for the MPPC and 33.9% for the MD-SiPM. The poor energy resolution is probably due to the lack of wrapping treatment and the dry contact between the detector and the crystal. The MD-SiPM is further affected by its stronger non-linear behavior due to its pixel's 1-bit memory. According to the Monte Carlo study provided in Chapter 4, 23~24% energy resolution at FWHM for the 511 keV photo-peak is obtained for the MD-SiPM with about 50 Mcps DCR and 12.5% PDE.

Tab. 7.3: Energy resolution at FWHM (σ_E^{FWHM}/E)

E [keV]	MPPC	MD-SiPM
511	23.2%	33.9%
661.7	18.8%	28.6%
1275	14.7%	-

Tab. 7.4: Detector response to 511keV gamma

	MPPC	MD-SiPM
# of pixel fired	466	131
corresponding linear response	577	196
non-linear correction	19.2%	33.2%
# of incident photon	1702	1568

7.3 Conclusion

The digital implementation of the SiPM, namely the MD-SiPM that is developed for the EndoTOFPET-US project, performs worse than the analog SiPM with a similar form factor in term of energy resolution. This is mainly due to the limited dynamic range and high DCR of the MD-SiPM. However, its DCR can be improved by paying the price of a reduced PDE.

For the EndoTOFPET-US project, the digital SiPM is the only feasible solution due to the strict geometrical constraint. The result presented in this work has validated that the MD-SiPM is a viable solution for the read out of the internal probe.

Chapter 8

RADIATION DAMAGE TO SiPM

After more than 30 years of development, the analog SiPMs are now well established high-gain photodetectors, which have found numerous applications in nuclear medicine, high energy physics and astronomy physics [81]. They are highly sensitive devices, which are capable of detecting single photon. Thus the impact of radiation damage to SiPM's performance becomes potential concerns in some field. In numerous investigations [82, 83], it has been found, that for high-energy radiation the dominant radiation effect for SiPMs is an increase in the dark-count rate due to defects in the silicon crystal. Given that radiation damage presents a serious limitation for many applications, several groups together with the producers of SiPMs are undertaking major efforts to make SiPMs more radiation tolerant. Thanks to the SiPM characterization procedure developed for this work, a contribution was made to the studies of radiation hardness of the analog SiPM.

This chapter summarizes the X-ray radiation damage study performed on the analog SiPM MPPC S10362-11-050C from Hamamatsu. The characterization methods introduced in Chapter 6 are used to evaluate the performance of the SiPM before and after irradiation.

8.1 X-ray Radiation Damage in Silicon Detector

The radiation damage mechanism in silicon detectors can be divided in two classes: bulk damage and surface damage. The bulk damage is caused by the non-ionizing energy loss interactions of a primary particle with a lattice silicon atom. With sufficient energy, the silicon atom can be removed from the crystal lattice, becomes an interstitial defect and leaves a vacancy in the lattice. The energy threshold for the bulk damage in silicon varies for different type of particles. The energy of X-ray used for the irradiation study in this thesis is below 300 keV, which is the threshold energy for the formation of defects in the silicon bulk, therefore only the surface damage is concerned.

The surface damage is the defects in the dielectrics, at the Si-SiO₂ interface and at the interfaces between dielectrics. In SiO₂ X-rays produce on average one electron-hole (eh) pair every 18 eV of deposited energy. Depending on ionization density and electric field, a fraction of the eh pairs recombine. The remaining charge carriers move in the SiO₂ by diffusion and, if an electric field is present, by drift. Most electrons, due to their high mobility and relatively low trapping probability, leave the SiO₂. However holes, which move via polaron hopping, are typically captured by deep traps in the SiO₂ or at the Si-SiO₂ interface, which results in fixed positive charge states (with density N_{ox}) and interface traps (with density N_{it}). The interface traps, if exposed to an electric field, act as generation centers for a surface current with density J_{surf} .

Before irradiation, typically values for N_{ox} and J_{surf} are a few 10^{10} per cm^2 and a few nA/cm^2 , respectively. The surface current contribute significantly to the measured dark current of the SiPM below

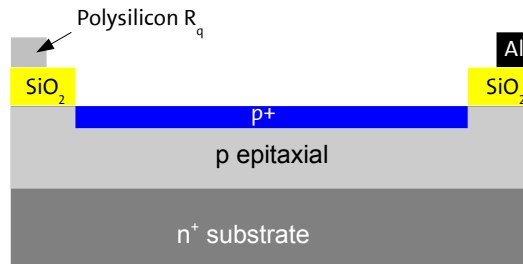


Fig. 8.1: Schematic cross section of the SiPM MPPC S10362-11-050C from Hamamatsu after [84]. The Al contact line, the polysilicon layer of the quenching resistor and the SiO₂ layer are added. The drawing is not to the scale, from the capacitance measured above full depletion, the p-epitaxial layer is estimated to be about 2.3 μm .

the breakdown voltage. After irradiation, the increase of both values depends on many factors including the radiation dose, the production technology, the crystal orientation and the value and the direction of the electric field in the oxide. A significant increase of the dark current below the breakdown voltage can be expected. In case a fraction of the charge carriers from the surface generation current reaches the amplification region of the diode, an increase of dark count rate (DCR) may also occur above the breakdown voltage. This however depends on the details of the design of the SiPM.

8.2 X-ray Irradiation

The X-ray irradiations up to 20 kGy were performed at an X-ray tube (PW2273/20 from PANalytical). Using a Mo target the dose rate in SiO₂ at a distance of 20 cm was approximately 0.6 Gy/s. After characterizing the SiPMs, four have been irradiated to 200 Gy and two of those later to 20 kGy. No bias has been applied to the SiPM during irradiation. The X-ray irradiations to 2 MGy and 20 MGy were performed with X-rays of 8 keV in the P11 beam line of PETRAIII [85] with a dose rate of approximately 2 kGy/s. Two sensors were irradiated to 2 MGy, and two others to 20 MGy. All irradiations and measurements were performed at 22 to 25°C. In between measurements and irradiations the SiPMs were stored at 20°C to prevent annealing.

8.3 SiPM Characteristics Before and After Irradiation

The static and dynamic characteristics of the devices are measured before and after different doses of X-ray irradiations.

8.3.1 Forward Current

Fig. 8.2 shows the forward IV measurements of the SiPM samples before and after different doses of X-ray irradiation. A decrease of the voltage drop (V_d in Eq. 6.1) over the diode for samples with above 200 kGy irradiation is observed. One possible explanation is the radiation induced positive oxide charges in the

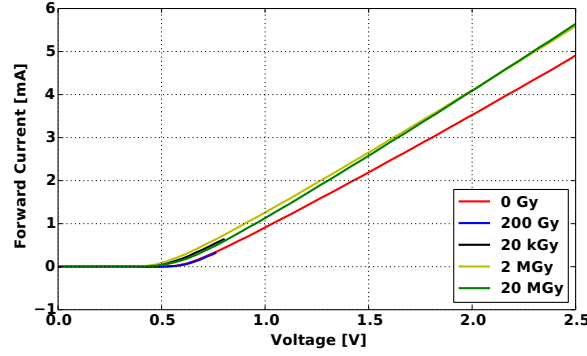


Fig. 8.2: Forward IV measurements for the Hamamatsu SiPM after different X-ray doses of irradiation, curves are measured using different samples.

Tab. 8.1: The measured R_q^{IV} as a function of X-ray doses.

0 Gy	200 Gy	20 kGy	2 MGy	20 MGy
$150 \pm 2 \text{ k}\Omega$	-	-	$136 \pm 2 \text{ k}\Omega$	$133 \pm 2 \text{ k}\Omega$

p-epitaxial layer has caused the voltage drop over the buried n^+p junction to increase, and thus effectively “shift” the measured forward IV curve to a lower voltage.

Due to a technical reason, only a referenced non-irradiated SiPM and the samples with 2 MGy and 20 MGy irradiation are measured to the voltage range where the linear fit can extract the quenching resistant. The values obtained for these samples are listed in Tab. 8.1. Note that different SiPMs are used for different doses of X-ray irradiation, a variation of 5% in R_q among the samples before irradiation is estimated.

The R_q^{IV} of the SiPM shows slight decrease after the X-ray irradiation, this may be explained by the irradiation induced damages on the polysilicon which cause their resistance to decrease. However, it is observed that the measured IV curves show dependence on the ramping speed of the applied voltage for irradiated SiPM samples. Therefore a systematic uncertainty on the values is hard to estimate.

8.3.2 Reverse Current

Fig 8.3a shows the reverse IV curve for several SiPM samples before and after irradiation of 200 Gy, 20 kGy, 2 MGy and 20 MGy. The measured current below the breakdown voltage increases by several orders of magnitude after irradiation. As explained previously, the X-ray irradiation creates Si-SiO₂ interface traps acting as current generation centers and increase the dark current. The increase of the dark current at 60 V as a function of the irradiated X-ray doses is shown in the Fig 8.3b.

The V_{bd}^{IV} of the samples are determined before and after the X-ray irradiation using the reverse IV curve. Fig. 8.4 shows the results of the sample number 919 before and after the X-ray irradiation of 200 Gy and 20 kGy, and the sample number 802 before and after the X-ray irradiation of 2 MGy. Due to the large increase of the surface current after irradiation, the current increasing rate change before and after the breakdown voltage is much less obvious after the X-ray irradiation. This is reflected in the derivative of the logarithmic IV curve, no sharp peak is shown for the irradiated samples. It is also possible that the irradiation on the sensor is not uniform, therefore some pixels are damaged and become conductive while still pixels working properly. As an overall effect, no sharp increase of the current is observed. Thus the

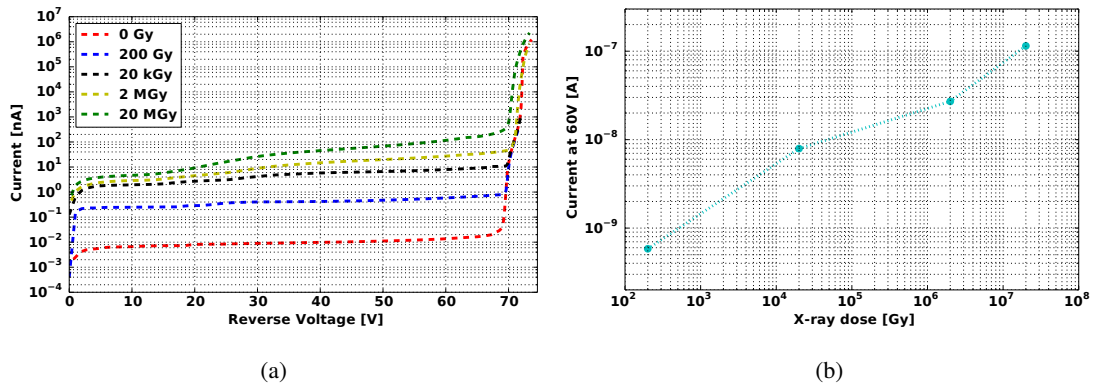


Fig. 8.3: (a) Reverse IV measurements for different SiPM samples after different X-ray doses of irradiation. (b) The measured dark current at 60 V as a function of irradiation dose, the data is connected by a dotted line to guide the eye.

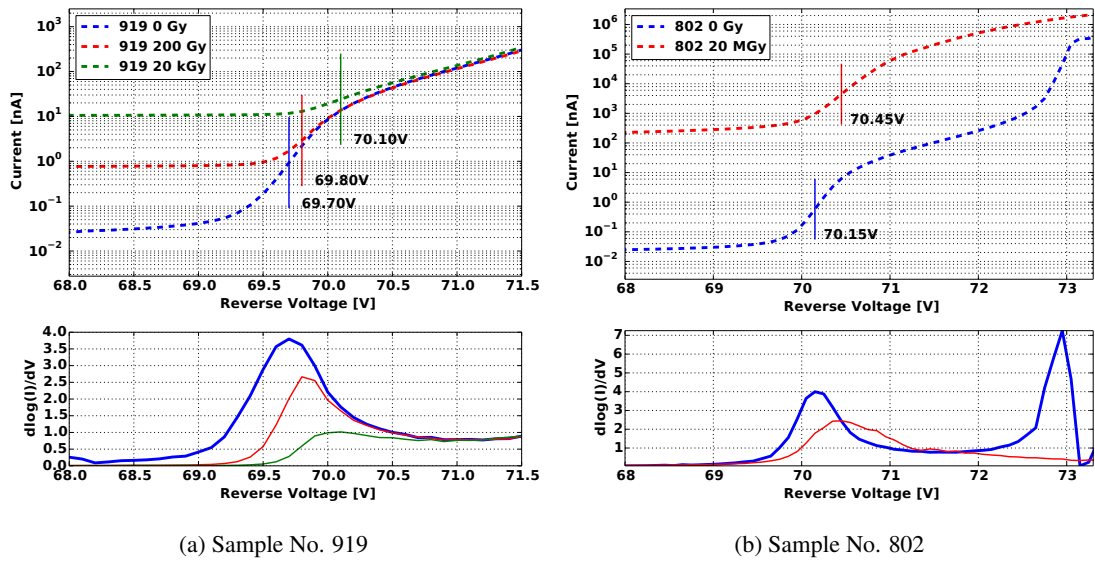


Fig. 8.4: Reverse IV curves of the Hamamatsu SiPM samples before and after different doses of X-ray irradiation. The breakdown voltage is determined as the position of the local maximum in the derivative of the logarithmic IV curve.

Tab. 8.2: V_{bd}^{IV} from reverse IV measurements

Sample No.	Before Irradiation [V]	After Irradiation [V]	Dose
922	69.7	69.8	200 Gy
919	69.7	69.8	200 Gy
804	70.14	71.34	2 MGy
805	70.28	71.48	2 MGy
802	70.15	70.45	20 MGy
925	69.59	70.09	20 MGy

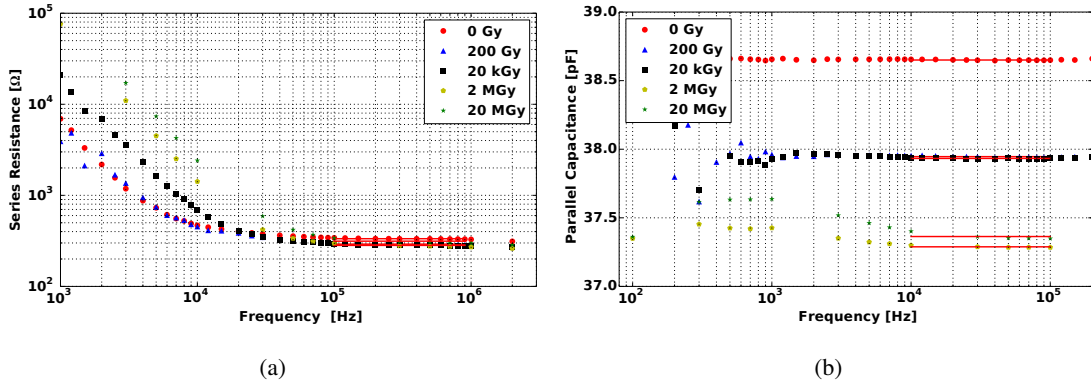


Fig. 8.5: The C/G measurement with frequency sweeping measured at 67 V and 25°C for different X-ray doses. A constant fit is applied to the data at high frequencies for (a) the parallel capacitance and (b) the series resistance.

obtained V_{bd}^{IV} for the irradiated samples may be not reliable.

Table 8.2 summarizes V_{bd}^{IV} for different samples before and after X-ray irradiation. The error of all V_{bd}^{IV} values is 0.1 V, which is the voltage sweeping step size.

8.3.3 C/G versus Frequency

The series resistance and parallel capacitance of SiPM samples with different X-ray doses measured by the C/G measurements with frequency sweeping is shown in Fig. 8.5. The measurements was performed for frequencies in the range between 100 Hz and 2 MHz at bias voltage of 67 V. The amplitude of the AC voltage is 500 mV. The constant fit is performed on the values between 100 kHz and 1 MHz for the series resistance and between 10 kHz and 100 kHz for the parallel capacitance. Table 8.3 summarizes the calculated values of R_q^{CV} and C_{pix}^{CV} together with $\tau_d^{CV} = R_q^{CV} \cdot C_{pix}^{CV}$, which is approximately the recharging time of a single pixel, as a function of the X-ray doses.

Although the measured pixel capacitance shows small decrease after X-ray irradiation, considering the measurement error of 1.5% and variation between different SiPM samples, the pixel capacitance is essentially independent of the X-ray dose. Whereas the similar decrease of quenching resistance is observed as from the forward current measurement, despite the measured R_q^{CV} is about 10% lower than R_q^{IV} at 0 Gy.

Tab. 8.3: R_q^{CV} and C_{pix}^{CV} by the C/G frequency sweeping for different X-ray doses.

Dose	0 Gy	200 Gy	20 kGy	2 MGy	20 MGy
R_q^{CV} [k Ω]	134 \pm 5	117 \pm 5	114 \pm 5	113 \pm 5	126 \pm 5
C_{pix}^{CV} [fF]	96.6 \pm 1.5	94.9 \pm 1.5	94.8 \pm 1.5	93.2 \pm 1.5	93.4 \pm 1.5
τ_d^{CV} [ns]	12.9 \pm 0.6	11.1 \pm 0.6	10.8 \pm 0.6	10.5 \pm 0.6	11.8 \pm 0.6

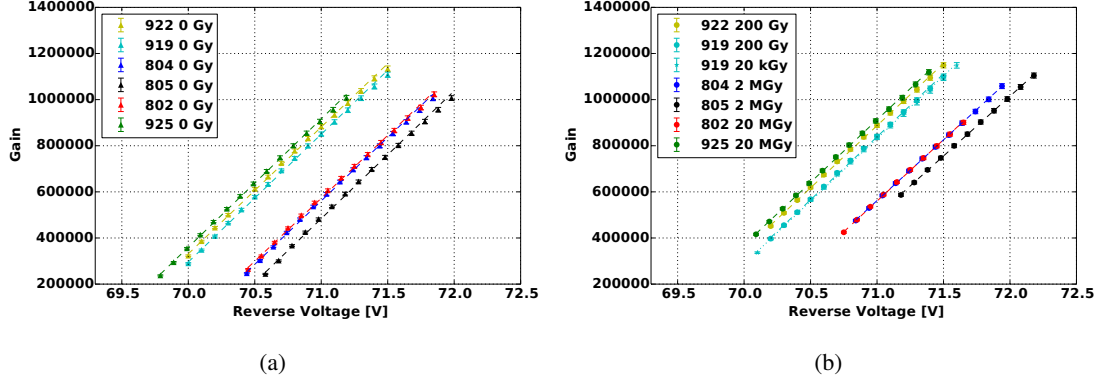


Fig. 8.6: Gain as a function of the reverse bias voltage for different SiPM samples (a) before the X-ray irradiation, (b) after different doses of X-ray irradiation.

8.3.4 Gain and Breakdown Voltage

The gain and breakdown voltage of the SiPM are characterized before and after different doses of irradiation. The setup used for the characterization measurements is described in Chapter 6. The integration time of the QDC is 100 ns, and all measurements are carried out at $25\pm 0.5^\circ\text{C}$. Fig 8.6 shows the gain dependence on the reverse bias voltage for different SiPM samples before and after irradiation. Values of V_{bd}^G and dG/dV are summarized in the Tab. 8.4. The pixel capacitance C_{pix}^G is calculated with equation 6.9. In addition to the calculated uncertainties given in the table, values of C_{pix}^G is estimated to have systematic uncertainties of about 10%.

Within the measurement errors the breakdown voltage does not change with irradiation. Whereas small changes in values of the pixel capacitance are observed. The decreases of pixel capacitance after irradiation are between 2% and 6%, and are independent from the irradiation dose.

8.3.5 Dark Count Rate

The DCR of the samples after different doses of X-ray irradiation are measured. The detail of the experiment is described in Chapter 6 and the effective gate for equation 6.15 is 100 ns. All measurements are carried out in dark environment at $25\pm 0.5^\circ\text{C}$. The DCR of the SiPM samples before irradiation at gain of $7.5\times 10^5 \text{ V}^{-1}$ has a varies about 10%.

Fig 8.7 shows the DCR versus the excess voltage, $V_{op} - V_{bd}^G$, for SiPMs before and after irradiation to 200 Gy, 20 kGy, 2 MGy and 20 MGy. Whereas the DCR before and after irradiation to 200 Gy and 20 kGy are similar, they increase significantly after irradiation to 2 MGy and 20 MGy. This can be explained by the increase with X-ray dose in the number of electrons which reach the amplification region and cause a Geiger discharge of a pixel due to the increased surface generation current at the depleted Si-SiO₂ interface.

Tab. 8.4: Dose dependence of the gain and breakdown voltage of the different SiPM samples

Sample No.	Before Irradiation			After Irradiation			Dose
	V_{bd}^G [V]	$dG/dV [\times 10^5/V]$	C_{pix}^G [fF]	V_{bd}^G [V]	$dG/dV [\times 10^5/V]$	C_{pix}^G [fF]	
922	69.40±0.03	5.50±0.04	88.0±0.6	69.35±0.03	5.39±0.05	86.2±0.8	200 Gy
919	69.47±0.03	5.54±0.03	88.6±0.5	69.46±0.03	5.46±0.05	87.4±0.8	200 Gy
				69.47±0.03	5.44±0.04	87.0±0.6	20 kGy
804	69.98±0.03	5.50±0.04	88.0±0.6	69.93±0.03	5.27±0.06	84.3±1.0	2 MGy
805	70.13±0.03	5.54±0.04	88.6±0.6	70.04±0.03	5.19±0.08	83.0±1.1	2 MGy
802	69.95±0.03	5.45±0.04	87.2±0.6	69.95±0.03	5.32±0.07	85.1±1.3	20 MGy
925	69.35±0.03	5.57±0.04	89.1±0.6	69.32±0.03	5.43±0.05	86.9±0.8	20 MGy

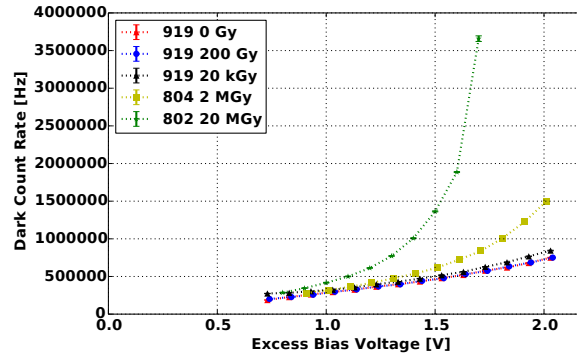


Fig. 8.7: Dark count rate for several SiPMs as function of the excess voltage, $V_{op} - V_{bd}^G$, before and after irradiation to 200 Gy, 20 kGy, 2 MGy and 20 MGy. The sample number is shown in the legend. Data points are connected by the dash line to guide the eye.

8.3.6 The Correlated Noise

The correlated noise probability (P_{cn}) which is the combined contribution of cross talk and afterpulse, defined by equation 6.16, is measured simultaneously with the DCR. Fig. 8.8 shows the correlated noise probability as function of excess voltage before and after irradiation to 200 Gy, 20 kGy, 2 MGy and 20 MGy. For small doses the correlated noise probability is essentially independent from the X-ray dose, it increases for the high dose irradiations. A possible reason is the increase of after-pulses due to the radiation-induced defects. This however needs further studies.

8.3.7 Pulse Shape

The output signal of the SiPM samples are amplified by a factor of 50 using the Philips Scientific waveform amplifier and recorded by the Tektronix DPO-7254 oscilloscope for the investigation of pixel's recharging time. The scope has bandwidth of 2.5 GHz and a maximum sampling rate of 20 Gsamples/second. The SiPM is illuminated with the pulsed LED, using a trigger shorter than 3 ns. The bias voltage for the SiPM is chosen such that the gain of the SiPM is at $(7.50 \pm 0.02) \times 10^5$. More than 100 pulses corresponding to single pixel discharging are selected off-line to produce an averaged pulse signal from the SiPM. The selection requires the maximum pulse height occurs within ± 1 ns of the time expected for the LED signal,

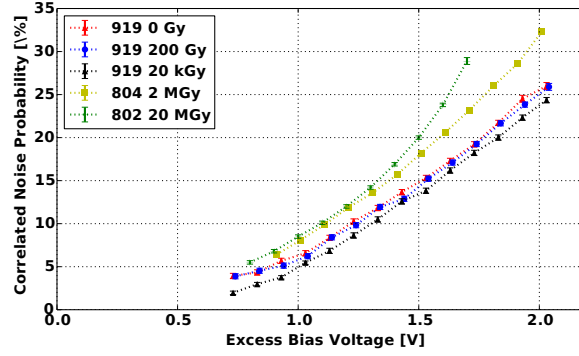


Fig. 8.8: The correlated noise probability for several SiPMs as function of the excess voltage, $V_{op} - V_{bd}^G$, before and after irradiation to 200 Gy, 20 kGy, 2 MGy and 20 MGy. The sample number is shown in the legend. Data points are connected by the dash line to guide the eye.

and that its value is in the range ± 1 mV of 10 mV, the average of single pixel events, and that the pulse shape did not show a step of more than 1 mV to 40 ns after the start of the pulse.

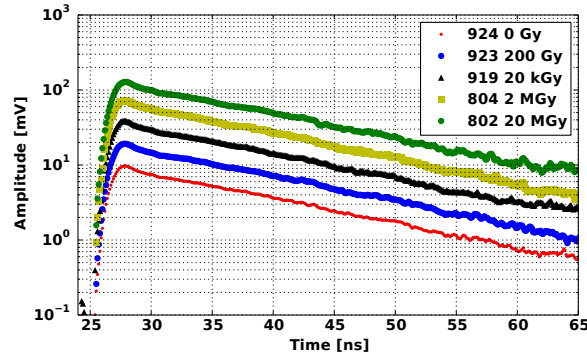


Fig. 8.9: The averaged pulse shape of ~ 100 single pixel events with a selection which suppresses after-pulses, for SiPMs operated at a gain of 7.5×10^5 before and after irradiation to 200 Gy, 20 kGy and 20 MGy. For better visibility, the curves are shifted by a factor of two for every step in dose.

Fig 8.9 shows the averaged pulses from the SiPM samples before and after irradiation to 200 Gy, 20 kGy, 2 MGy and 20 MGy. Note that for better visibility, the curves are shifted by a factor of two for every step in dose. The rise time of the pulses is about 1 ns. At the maximum there is a small peak with a width of about 1 ns, which is related to the Geiger discharge and the value of the parasitic capacitance, C_q , in parallel to the quenching resistor, R_q (c.f. Fig 6.8). The slow component in the measured pulse shape is fitted to an exponential function for the estimation of the pixel's recharging time, denoted by τ_d^{WF} . The fitting range for the exponential function is chose to be from 30 ns to 50 ns in Fig. 8.9. The uncertainty is estimated by varying the end of the fit range by ± 10 ns. Table 8.5 summarizes the pixel recharging time as a function of the X-ray irradiation doses.

The fitted pixel recharging time is independent from the X-ray irradiation dose within the experimental uncertainties.

Tab. 8.5: Pixel recharging time for SiPMs measured at a gain of 7.5×10^5 as a function of dose

Dose	0 Gy	200 Gy	20 kGy	2 MGy	20 MGy
τ_d^{WF} [ns]	13.6 ± 0.5	13.6 ± 0.5	13.7 ± 0.5	13.3 ± 0.5	13.8 ± 0.5

8.4 Discussion of the Results

The pixel capacitance and quenching resistance of the SiPM pixel and the figures of merit for the SiPM operation are investigated before and after X-ray irradiation with different doses.

The pixel capacitance of the SiPM is determined in two ways: use the capacitance frequency measurement below the breakdown voltage and the gain measurement above the breakdown voltage. For the non-irradiated sample, C_{pix}^G is about 8% lower than C_{pix}^{CV} . Since the change of C_{pix} from below to above the breakdown voltage should be negligible, the difference in C_{pix} obtained by the two measurements is mainly attributed to the absolute calibration of the gain measurement. Both measurements show a decrease of C_{pix} with X-ray dose. However the change is so small that the gain of the SiPM is hardly affected, therefore it can be concluded that the gain of the Hamamatsu SiPM remains independent from irradiation dose up to 20 MGy.

Values of the quenching resistance decrease after X-ray irradiation up to 20 MGy (shown in Tab. 8.1 and Tab. 8.3). The result is consistent for R_q measured by the forward IV measurement and C/G-frequency measurement. A possible explanation is the radiation-induced traps in the polysilicon quenching resistors, which cause their resistance to decrease. However from an operational point of view, the RC constants, both τ_d^{CV} and τ_d^{WF} , remain unchanged within the measurement error before and after the irradiation. Therefore the charge integration time for the signal readout and potentially the timing performance of the SiPM are unaffected by the irradiation with a dose up to 20 MGy.

The breakdown voltage measured by the gain measurement stays constant within the measurement errors. The breakdown voltage extracted by the reverse IV curve shows a significant increase after the irradiation with a dose above 20 kGy. This increase can be explained by a dramatic increase in the surface current, which causes a smoother transition of the current increase before and after the device's breakdown. The transition can be seen from the logarithmic scale derivative curves of IV measurements shown in Fig. 8.4. The errors of V_{bd}^{IV} are hard to estimate. It should be noted that the high field breakdown also critically depends on environmental parameters such as humidity, which was not controlled in the measurement. Nevertheless, as discussed in Chapter 6, the breakdown voltage determined by the gain measurement has more practical meaning for the SiPM operation. The fact that its value is independent from the X-ray dose up to 20 MGy is a potential advantage for the Hamamatsu SiPM for its operation in an aggressive radiation environment.

Below the breakdown voltage, the reverse current increases by about three orders of magnitude for X-ray doses between 0 and 20 MGy. The total increase can be explained by the radiation-induced increase in surface current at the depleted Si-SiO₂ interface and some charge carrier multiplication.

Above the breakdown, up to an X-ray dose of 20 kGy the voltage dependence of the reverse current can be described by the sum of the dose independent bulk current, which leads to Geiger discharges, plus the radiation induced surface current which is hardly amplified. The increase of the reverse current with dose is less than a factor of two for excess voltages above 0.5 V. For X-ray doses of 2 and 20 MGy the reverse current above breakdown voltage increases by 2 to 3 orders of magnitude and significant shifts of the voltage are observed, at which the current starts to increase. In addition only part of the dark current can be explained by the measured DCR, gain and correlated noise. The observed current therefore is ascribed to three effects: a high field charge carrier multiplication which does not trigger Geiger discharges, electron-hole pairs generated in the bulk and electron-hole pairs generated at the Si-SiO₂ interface. The later two cases both cause Geiger discharges.

Electrons generated at the Si-SiO₂ interface are responsible for the observed dose dependence of DCR on X-ray dose. An X-ray dose of 200 Gy does not affect the DCR, at 20 kGy a small but significant increase at the 10% level is observed, and finally at 20 MGy the DCR increases by about an order of magnitude for excess bias voltages above 1.8 V. The correlated noise probability also shows an increase depending on the X-ray dose. These effects are the potential limiting factors for the application of SiPM if its high photon sensitivity is required. High noise rate after X-ray irradiation may deteriorate the signal to noise ratio and render the operational detector unusable. For the application of SiPMs in HEP detectors such as calorimeters, further study of neutron radiation-induced bulk damages still need to be investigated.

Chapter 9

CONCLUSION

The work presented in this thesis deals with scintillation detectors which use inorganic scintillators to convert the energy of ionizing particles to light, and silicon photomultipliers (SiPM) for the detection of visible light. The study of the SiPM is mainly focused on its application in the proposed EndoTOFPET-US detector, which is a multi-modality positron emission tomography detector for the development of new biomarkers for pancreas and prostate cancers.

A Monte Carlo simulation tool of a single channel detector is developed to help the optimization of the detector design. Based on the simulation results, the crystal length that is optimum for the detector sensitivity while ensures a 200 ps coincidence time resolution (CTR) is 15 mm. Using 15 mm crystals in both internal and external detectors should provide an overall single channel sensitivity in the range of 8.2-9.4%. In addition, in order to achieve a 200 ps CTR, more than 1700 photons should be detected in the 511 keV photo-peak. Provided a LYSO with light yield of 32000 photons per MeV and the assumed light loss in the propagation, a minimum SiPM photon detection efficiency (PDE) of 15.5% is required. This should in turn give a minimum energy resolution for the 511 keV photo-peak larger than 17% after non-linearity correction. This energy resolution is sufficient to separate Compton continuum from the photo-peak in the energy spectrum. The requirements for the MD-SiPM are a PDE larger than 10% and a dark count rate (DCR) smaller than 10 Mcps. Provided the measured results of the prototype, cooling of the device during operation is necessary in order to fulfill the requirements. An energy resolution for the 511 keV photo-peak below 20% can be obtained with the above mentioned PDE and DCR value. While the PDE of the device is crucial for the time performance, a high dark count rate may result in further loss in the detector sensitivity.

In order to identify suitable photodetectors for positron emission tomography or other applications a series of experimental methods are established. The static characterization measurements allow the determination of the pixel capacitance, quenching resistance, and breakdown voltage of the SiPM, whereas the dynamic characterization measurements measure the gain, breakdown voltage, DCR, correlated noise probability and the signal pulse shape. Several SiPM samples produced by different manufacturers are characterized and the results are summarized. The breakdown voltage of the SiPM can be determined with the highest precision using the gain measurement. This is an essential requirement for the characterization measurement. With a precise knowledge of the breakdown voltage, characteristics of a SiPM such as gain, DCR and correlated noise probability during its operation can be accurately controlled by tuning the excess bias voltage. A normal voltage power supply with 10 bit resolution in the 100 V range can provide a voltage output with a precision of 10 mV and a stability normally of the same order. The STiC readout chip, which is the candidate SiPM readout ASIC for the EndoTOFPET-US detector, provides an output voltage precision of 20 mV [34]. Therefore the 30 mV precision of breakdown voltage obtained by the developed gain measurement is compatible with the above mentioned voltage regulation precision and

fulfills the requirement for the SiPM characterization test. The gain of the SiPM is in the order of 10^6 and depends linearly on the excess bias voltage. Its value can be measured with a precision below 2%. As a comparison, [51] quotes the uncertainty of the gain measurement in the order of 5% and their breakdown voltage is obtained with a precision of 0.1 V.

The pixel capacitance and its quenching resistance determine the pixel recharging time constant, which in turn affects the measuring condition such as the charge integration time interval for the gain measurement. This parameter should be determined before the gain measurement in order to have a reliable and correct measurement result. The whole procedure is established and fully automatized through the development of this work. The dark count rate of the SiPM samples are in the range of 200 kcps up to 1 Mcps per mm^2 within the operating voltage range of interest. The correlated noise probability also shows a dependence on the excess bias voltage which originates from the gain dependence of cross talk and afterpulses. The parameters determined in different ways generally agree within their estimated uncertainties, and are consistent with the reference data quoted by the manufacturers. Although the cross talk and after-pulse probability is not measured separately, the correlated noise probability measurement proposed by this work has largely reduced complexity of the setup and measurement time to characterize the noise property of the SiPM. This is valuable for a large scale measurement campaign. The setup developed in this lab is able to characterize all 16 channels of a Hamamatsu SiPM Matrix for their V_{bd} , gain, DCR and correlated noise probability with the above mentioned precision in 15 minutes. This is required for the quality assurance measurements of the mass quantity of SiPMs to be used in the EndoTOFPET-US detector, and potentially can be beneficial for other detectors using a large number of SiPMs.

A digital version of the SiPM utilizing the CMOS process to embed localized signal digitization and on chip time-to-digit converters (TDC), namely the MD-SiPM prototype, is introduced and tested. The prototype consists of 416 single photon avalanche diode (SPAD) pixels and 48 on-chip TDCs connected in parallel to the pixels. The characterization of the dark count rate shows a significantly higher value of about 50 Mcps per mm^2 compared to its analog counterpart. However, the noisy pixels of the sensor can be selectively turned off and thus the overall DCR of the device is reduced. In addition, the on-chip electronics can be used to further reduce the effect of noise, by generating event driven trigger validation signals. In order to evaluate the performance of the device reading out scintillators, the sensor is coupled to a LYSO crystal for a gamma spectroscopy measurement using a ^{22}Na source. A Hamamatsu SiPM with similar sensitive area is used to read out the same crystal for comparison. The obtained spectra from both sensors are corrected for their non linearity using a custom developed simulation tool. The energy resolution at full-width-half-maximum (FWHM) for the 511 keV photo-peak is 33.9% for the MD-SiPM and 23.2% for the Hamamatsu SiPM. The worse than expected energy resolution is mainly attributed to the lack of a dedicated crystal wrapping and gluing process and therefore significant loss of photons on the surface of the crystal. Due to the extremely small geometrical acceptance in the proposed internal probe of the EndoTOFPET-US detector, the MD-SiPM is potentially the only feasible solution. Further tests in the detector performance will be carried out with an improved chip design and dedicated crystal coupling and wrapping processes.

The SiPM characterization measurement is also used to study the X-ray induced surface damage to a Hamamatsu SiPM. Characteristic parameters of the SiPM are measured and compared as a function of X-ray doses up to 20 MGy. Changes of several parameters as a function of the X-ray dose is observed, in particular the dark current below the breakdown voltage, and DCR and correlated noise probability above the breakdown voltage. The change in quenching resistance and pixel capacitance are considered negligible for the operation of the SiPM. The study shows that the Hamamatsu SiPM can be operated after X-ray irradiation to a dose of 20 MGy. Up to 20 kGy the changes are minor, whereas for the dose value of 20 MGy the DCR increases by an order of magnitude. This is a limiting factor for the use of a SiPM in a radioactive environment with its high photon counting sensitivity. Further studies of neutron induced bulk damages are needed if the SiPMs are adopted for high energy physics experiments in building calorimeters.

Bibliography

- [1] S. A. Dyer, *Wiley Survey of Instrumentation and Measurement*. John Wiley and Sons Ltd., 2004.
- [2] D. L. Bailey, D. W. Townsend, P. E. Valk, and M. N. Maisey, *Positron Emission Tomography: Basic Sciences*. Springer, 2003.
- [3] M. Kumar and S. K. Sarin, "Biomarkers of diseases in medicine," *Current Trends of Science Platinum Jubilee Special, Indian Academy of Sciences, Bangalore, India*, pp. 403--417, 2009.
- [4] S. B. Aijnger, T. Laubert, U. Roblick, and J. Habermann, "Serum Biomarkers for Improved Diagnostic of Pancreatic Cancer: a Current Overview," *Journal of Cancer Research and Clinical Oncology*, vol. 137, no. 3, pp. 375--389, 2011.
- [5] A. Jemal *et al.*, "Cancer Statistics, 2008," *CA: a cancer journal for clinicians*, vol. 58, no. 2, pp. 71--96, 2008.
- [6] America Cancer Society, "Cancer Facts and Figures 2010," 2010.
- [7] "Endo-TOFPET-US Proposal: Novel multimodal endoscopic probes for simultaneous PET/ultrasound imaging for image-guided interventions," Jan. 2010, European Union 7th 186 Framework 187 Program (FP7/2007-2013) under Grant Agreement No. 256984.
- [8] E. Garutti *et al.*, "Silicon photomultiplier characterization and radiation damage investigation for high energy particle physics applications," *Journal of Instrumentation*, vol. 9, no. 03, p. C03021, 2014. [Online]. Available: <http://stacks.iop.org/1748-0221/9/i=03/a=C03021>
- [9] D. W. Rickey, R. Gordon, and W. Huda, "On Lifting the Inherent Limitations of Positron Emission Tomography by Using Magnetic Fields (MagPET)," *Automedica*, vol. 14, pp. 355--369, 1992.
- [10] D. E. Robley, *The Atomic Nucleus*. Tata McGraw Hill Publishing Company Limited, 1955.
- [11] H. E. Johns and J. R. Cunningham, *Physics of Radiology, 4th edition*. Charles C Thomas Pub Ltd., 1983.
- [12] B. Guerin and G. E. Fakhri, "Novel Scatter Compensation of List-mode PET Data Using Spatial and Energy Dependent Corrections," *IEEE transactions on medical imaging*, vol. 30, no. 3, 2011.
- [13] M. Conti, I. Hong, and C. Michel, "Reconstruction of Scattered and Unscattered PET Coincidences Using TOF and Energy Information," *Physics in medicine and biology*, vol. 57, pp. 307--317, 2012.
- [14] C. W. E. van Eijk, "Inorganic Scintillators in Medical Imaging," *Physics in medicine and biology*, vol. 47, pp. 85--106, 2002.
- [15] K. A. Comanor, P. R. G. Virador, and W. W. Moses, "Algorithms to Identify Detector Compton Scattering PET Modules," *IEEE transactions on nuclear science*, vol. 43, no. 4, 1996.

- [16] Y. Shao, S. R. Cherry, S. Siegel, and R. W. Silverman, "A Study of Inter-Crystal Scatter in Small Scintillator Arrays Designed for High Resolution PET Imaging," *IEEE Transactions on Nuclear Science*, vol. 43, no. 3, pp. 1938--1944, 1996.
- [17] Z. H. Cho and S. C. Juh, "Resolution and Sensitivity Improvement in Positron Emission Tomography," in *IEEE Nuclear Science Symposium and Medical Imaging Conference Record*, 1991, pp. 1623--1627.
- [18] A. Wagadarikar, A. Ivan, S. Dolinsky, and D. McDaniel, "Sensitivity Improvement of Time-Of-Flight (ToF)-PET Detector Through Recovery of Compton Scattered Annihilation Photons," in *IEEE Nuclear Science Symposium and Medical Imaging Conference Record*, 2012, pp. 3178--3183.
- [19] W. R. Leo, *Techniques for Nuclear and Particle Physics Experiments: A How-To Approach*. Springer, 1994.
- [20] G. F. Knoll, *Radiation Detection and Measurement, 4th edition*. John Wiley and Sons Ltd., 2010.
- [21] S. Derenzo, M. Weber, E. Bourret-Courchesne, and M. Klintonberg, "The quest for the ideal inorganic scintillator," *Nuclear Instruments and Methods in Physics Research A*, vol. 505, pp. 111--117, 2003.
- [22] Y. Shao, "A new timing model for calculating the intrinsic timing resolution of a scintillator detector," *Physics in Medicine and Biology*, vol. 52, pp. 1103--1117, 2007.
- [23] M. W. Fishburn and E. Charbon, "System Tradeoffs in Gamma-Ray Detection Utilizing SPAD Arrays and Scintillators," *IEEE Transactions on Nuclear Science*, vol. 57, no. 5, pp. 2549--2557, 2010.
- [24] M. Daube-Witherspoon and G. Muehllehner, "Treatment of axial data in three-dimensional PET," *Journal of Nuclear Medicine*, vol. 28, pp. 1717--1724, 1987.
- [25] C. S. Levin, "Primer on Molecular Imaging Technology," *European Journal of Nuclear Medicine and Molecular Imaging*, vol. 32, no. 2, pp. S325--S345, 2005.
- [26] The EndoTOFPET-US collaboration, "EndoTOFPET-US Specifications," March 2011.
- [27] M. A. Spurrier *et al.*, "Effects of Ca^{2+} Co-doping on the scintillation properties of $\text{LSO}:\text{Ce}$," *IEEE Transactions on Nuclear Science*, vol. 55, no. 3, 2008.
- [28] T. Szczesniak *et al.*, "Fast Photomultipliers for TOF PET," *IEEE Transactions on Nuclear Science*, vol. 56, no. 1, Feb. 2009.
- [29] Hamamatsu Photonics K. K., "Photomultiplier tubes: basics and applications, 3rd edition," 2007.
- [30] L. Swiderski *et al.*, "Light Yield Non-Proportionality and Energy Resolution of Praseodymium Doped LuAG Scintillator," *IEEE Transactions on Nuclear Science*, vol. 56, no. 3, pp. 934--938, 2009.
- [31] G. Lutz, *Semiconductor Radiation Detectors*. Springer, 1999.
- [32] D. O'Connor, *Time-correlated Single Photon Counting*. Academic Press, 1984.
- [33] M. D. Rolo *et al.*, "TOFPET ASIC for PET applications," *Journal of Instrumentation*, vol. 8, p. C2050, Feb. 2013.

- [34] W. Shen, "Development of High Performance Readout ASICs for Silicon Photomultiplier (SiPMs)," 2012, PhD Thesis, Ruperto-Carola-University of Heidelberg, Germany.
- [35] "Adenocarcinoma of the Pancreas," 2002. [Online]. Available: <http://www.surgery.usc.edu/divisions/tumor/pancreasdiseases/webpages/pancreascancer/Adenocarcinomaofpancreas.html>
- [36] S. Mandai and E. Charbon, "Timing optimization of a h-tree based digital silicon photomultiplier," *Journal of Instrumentation*, vol. 8, no. 09, p. P09016, 2013. [Online]. Available: <http://stacks.iop.org/1748-0221/8/i=09/a=P09016>
- [37] S. Seifert, H. T. van Dam, and D. R. Schaart, "The Lower Bound on the Timing Resolution of Scintillation Detectors," *Physics in Medicine and Biology*, vol. 57, no. 7, pp. 1797--1814, 2012.
- [38] W. W. Moses and S. E. Derenzo, "Empirical observation of resolution degradation in positron emission tomographs utilizing block detectors," *Journal of Nuclear Medicine*, vol. 34, p. 101P, 1993.
- [39] W. Shen *et al.*, "STiC - A Mixed Mode Chip for SiPM ToF Applications," in *IEEE Nuclear Science Symposium and Medical Imaging Conference Record*, 2012, pp. 877--881.
- [40] R. Bugalho *et al.*, "EndoTOFPET-US Data Acquisition System," *Journal of Instrumentation*, vol. 8, no. 02, p. C02049, 2013.
- [41] S. Agostinelli *et al.*, "Geant4 -- a simulation toolkit," *Nuclear Instruments and Methods in Physics Research Section A: Accelerators, Spectrometers, Detectors and Associated Equipment*, vol. 506, no. 3, pp. 250 -- 303, 2003. [Online]. Available: <http://www.sciencedirect.com/science/article/pii/S0168900203013688>
- [42] J. Allison *et al.*, "Geant4 developments and applications," *Nuclear Science, IEEE Transactions on*, vol. 53, no. 1, pp. 270--278, 2006.
- [43] GEANT4 collaboration, "GEANT4 User Documentation." [Online]. Available: <http://geant4.cern.ch/support/userdocuments.shtml>
- [44] "Geant4 Physics Reference Manual." [Online]. Available: <http://geant4.web.cern.ch/geant4/G4UsersDocuments/UsersGuides/PhysicsReferenceManual/html/PhysicsReferenceManual.html>
- [45] D. Cooke *et al.*, "Crystal growth and optical characterization of cerium-doped Lu_{1.8}Y_{0.2}SiO₅," *Journal of Applied Physics*, vol. 88, no. 12, pp. 7360--7362, Dec 2000.
- [46] A. J. Wojtowicz *et al.*, "Scintillation properties of selected oxide monocrystals activated with Ce and Pr," *Optical Materials*, vol. 28, no. 1, pp. 85 -- 93, 2006, Polish-French-Israeli Symposium on Spectroscopy of Modern Materials in Physics Polish-French-Israeli Symposium on Spectroscopy of Modern Materials in Physics. [Online]. Available: <http://www.sciencedirect.com/science/article/pii/S0925346705001540>
- [47] E. Auffray *et al.*, "A Comprehensive & Systematic Study of Coincidence Time Resolution and Light Yield Using Scintillators of Different Size, Wrapping and Doping," in *IEEE Nuclear Science Symposium Conference Record*, 2011.
- [48] A. Levin and C. Moisan, "A More Physical Approach to Model the Surface Treatment of Scintillation Counters and its Implementation into DETECT," *IEEE Nuclear Science Symposium Conference Record*, vol. 2, pp. 702--706, Nov. 1996.

- [49] M. Janecek and W. W. Moses, "Simulating scintillator light collection using measured optical reflectance," *Nuclear Science, IEEE Transactions on*, vol. 57, no. 3, pp. 964--970, June 2010.
- [50] S. Nayar, K. Ikeuchi, and T. Kanade, "Surface reflection: physical and geometrical perspectives," *Pattern Analysis and Machine Intelligence, IEEE Transactions on*, vol. 13, no. 7, pp. 611--634, Jul 1991.
- [51] Eckert, P. and Schultz-Coulon, H.-C. and Shen, W. and Stamen, R. and Tadday, A., "Characterisation studies of silicon photomultipliers," *Nuclear Instruments and Methods in Physics Research A*, vol. 620, pp. 217--226, Aug 2010. [Online]. Available: <http://adsabs.harvard.edu/abs/2010NIMPA.620..217E>
- [52] H. J. Yoon, S. Itoh, and S. Kawahito, "A CMOS Image Sensor with In-pixel Two-stage Charge Transfer for Fluorescence Lifetime Imaging," *IEEE Transactions on Electron Device*, vol. 56, no. 2, pp. 214--221, Feb. 2009.
- [53] S. M. Sze and K. K. Ng, *Physics of Semiconductor Devices, 3rd edition*. Wiley-Interscience, 2006.
- [54] R. Grazioso *et al.*, "APD-based PET detector for simultaneous PET-MR imaging," *Nuclear Instruments and Methods in Physics Research Section A: Accelerators, Spectrometers, Detectors and Associated Equipment*, vol. 569, no. 2, pp. 301--305, 2006. [Online]. Available: <http://www.sciencedirect.com/science/article/pii/S0168900206014574>
- [55] G. A. Baraff, "Maximum Anisotropy Approximation for Calculating Electron Distributions; Application to High Field Transport in Semiconductors," *Physical Review*, vol. 133, no. 1A, pp. A26--A33, Jan. 1964.
- [56] Y. Okuto and C. R. Crowell, "Energy-Conservation Consideration in the Characterization of Impact Ionization in Semiconductors," *Physical Review B*, vol. 6, no. 8, pp. 3076--3080, Oct. 1972.
- [57] C. R. Crowell and S. M. Sze, "Temperature Dependence of Avalanche Multiplication in Semiconductors," *Applied Physics Letters*, vol. 9, no. 6, pp. 242--244, Sept. 1966.
- [58] E. Kamrani, F. Lesage, and M. Sawan, "Premature edge breakdown prevention techniques in cmos apd fabrication," in *New Circuits and Systems Conference (NEWCAS), 2012 IEEE 10th International*, 2012, pp. 345--348.
- [59] S. M. Sze and G. Gibbons, "Effect of Junction Curvature on Breakdown Voltage in Semiconductors," *Solid-State Electronics*, vol. 9, pp. 831--845, 1966.
- [60] B. Dolgoshein *et al.*, "An Advanced Study of Silicon Photomultiplier," *ICFA Instrumentation Bulletin*, vol. 23, pp. 28--41, 2001.
- [61] B. F. Aull *et al.*, "Geiger-Mode Avalanche Photodiodes for Three-Dimensional Imaging," *Lincoln laboratory journal*, vol. 13, no. 2, 2002.
- [62] S. Cova *et al.*, "Avalanche Photodiodes and Quenching Circuits for Single-Photon Detection," *Applied Optics*, vol. 35, no. 12, pp. 1956--1976, April 1996.
- [63] A. Gallivanoni, I. Rech, and M. Ghioni, "Progress in quenching circuits for single photon avalanche diodes," *Nuclear Science, IEEE Transactions on*, vol. 57, no. 6, pp. 3815--3826, 2010.
- [64] F. Zappa *et al.*, "Monolithic active-quenching and active-reset circuit for single-photon avalanche detectors," *Solid-State Circuits, IEEE Journal of*, vol. 38, no. 7, pp. 1298--1301, 2003.

- [65] M. Ward and A. Vacheret, "Impact of After-Pulse, Pixel Crosstalk and Recovery Time in Multi-Pixel Photon Counter Response," *Nuclear Instruments and Methods in Physics Research Section A: Accelerators, Spectrometers, Detectors and Associated Equipment*, vol. 610, no. 1, pp. 370 -- 373, 2009. [Online]. Available: <http://www.sciencedirect.com/science/article/pii/S0168900209011243>
- [66] K. F. Johnson, "Extending the dynamic range of silicon photomultipliers without increasing pixel count," *Nuclear Instruments and Methods in Physics Research Section A: Accelerators, Spectrometers, Detectors and Associated Equipment*, vol. 621, no. 1, pp. 387 -- 389, 2010. [Online]. Available: <http://www.sciencedirect.com/science/article/pii/S0168900210011034>
- [67] V. C. Spanoudaki and C. S. Levin, "Photo-detectors for time of flight positron emission tomography (tof-pet)," *SENSORS*, vol. 10, no. 11, pp. 10 484--10 505, 2010.
- [68] R. Pagano *et al.*, "Dark Current in Silicon Photomultiplier Pixels: Data and Model," *IEEE transactions on electron devices*, vol. 59, no. 9, pp. 2410--2416, Sept. 2012.
- [69] R. Newman, "Visible Light from a Silicon p-n Junction," *Physical Review*, vol. 100, pp. 700--703, Oct. 1955.
- [70] Andrea L. Lacaita and Franco Zappa and Stefano Bigliardi and Manfredo Manfredi, "On the Bremsstrahlung Origin of Hot-Carrier-Induced Photons in Silicon Devices," *IEEE transactions on electron devices*, vol. 40, no. 3, pp. 577--582, March 1993.
- [71] I. Rech *et al.*, "Optical crosstalk in single photon avalanche diode arrays: a new complete model," *Opt. Express*, vol. 16, no. 12, pp. 8381--8394, Jun 2008. [Online]. Available: <http://www.opticsexpress.org/abstract.cfm?URI=oe-16-12-8381>
- [72] A. Spinelli and A. L. Lacaita, "Physics and Numerical Simulation of Single Photon Avalanche Diodes," *IEEE Transactions on Electron Devices*, vol. 44, no. 11, pp. 1931--1943, 1997.
- [73] A. Lacaita and M. Mastrapasqua, "Strong Dependence of Time Resolution on Detector Diameter in Single Photon Avalanche-Diodes," *Electronics Letters*, vol. 26, pp. 2053--2054, Nov. 1990.
- [74] K. Yamamoto *et al.*, "Development of Multi-Pixel Photon Counter (MPPC)," in *IEEE Nuclear Science Symposium Conference Record*, 2006, pp. 1094--1097.
- [75] Philips Scientific, "Philips Scientific Fast Pulse Preamplifier Model 6954 data sheet." [Online]. Available: <http://www.phillipsscscientific.com/pdf/6954ds.pdf>
- [76] CAEN electronic instrumentation, "QDC 965A data sheet." [Online]. Available: <http://www.caen.it>
- [77] S. Kay, *Intuitive Probability and Random Processes using MATLAB*. Kluwer Academic Publishers, 2006.
- [78] A. Rochas *et al.*, "Low-noise silicon avalanche photodiodes fabricated in conventional CMOS technologies," *IEEE Transactions on Electron Devices*, vol. 49, pp. 387--394, Mar 2002.
- [79] Hilger Crystals, "Hilger LYSO(Ce) crystal data sheet." [Online]. Available: <http://www.hilger-crystals.co.uk>
- [80] Hamamatsu, "MPPC data sheet." [Online]. Available: <http://www.hamamatsu.com>
- [81] P. Buzhan *et al.*, "Silicon photomultiplier and its possible applications," *Nuclear Instruments and Methods in Physics Research A*, vol. 504, pp. 48--52, May 2003.

- [82] Y. Musienko *et al.*, “Radiation damage studies of multipixel Geiger-mode avalanche photodiodes,” *Nuclear Instruments and Methods in Physics Research A*, vol. 581, pp. 433--437, Oct. 2007.
- [83] I. Nakamura, “Radiation damage of pixelated photon detector by neutron irradiation,” *Nuclear Instruments and Methods in Physics Research A*, vol. 610, pp. 110--113, Oct. 2009.
- [84] K. Yamamoto, K. Yamamura, K. Sato, and S. Kamakura, “Newly developed semiconductor detectors by Hamamatsu,” in *International Workshop on New Photon-Detectors*, 2007.
- [85] [Online]. Available: http://petra3.desy.de/index_eng.html

ACKNOWLEDGEMENTS

First and foremost, I want to thank Prof. Dr. Erika Garutti for offering me this great opportunity to join the project, she has provided her expertise and invaluable guidance throughout my researching work, and supported me with patience for my thesis. I would like to thank Prof. Dr. Robert Klanner, who offers his superb expertise and insight in helping me finish my thesis. I extend my thanks and gratitude to my thesis and defense referee committee, for their time and efforts in reviewing my thesis.

My special thanks go to Dr. Alessandro Silenzi for his endless help and advice, and for the three years of working time with him. I am also grateful to Dr. Martin Göttlich, who provided guidance during my first year in DESY. Many thanks to Dr. Marco Ramilli for his inspiring ideas and discussions about the SiPM test and simulation. I also appreciate helps from Sebastian Laurien for debugging the setups with me and making them closer to perfection.

I would like to thank Karsten Gadow and Mathias Reinecke from DESY, Wolfgang Gärtner and Juergen Schütt from the university of hamburg who helped me build setups for SiPM tests. Without their delicate designs and excellent work, it would be impossible for me to finish my experiments.

The PhD work is funded by the European Union Seventh Framework Programme, under Grant Agreement number 256984 (EndoTOFPET-US). I am sincerely thankful to the colleagues of the EndoTOFPET-US collaboration for their strong supports, especially to Prof. Dr. Ir. Edoardo Charbon and Mr. Shingo Mandai, who provided the MD-SiPM samples and shared their expertises to help me with tests for the MD-SiPM.

It has been my pleasure to be a part of both the DESY FLC group and the UHH detector lab group. I am grateful to the FLC group leader Dr. Ties Behnke and Dr. Felix Sefkow, the FLC group secretary Andrea Schrader. Along the three years of time, I have received supports from too many people to count. Milan Zvolisky and Daniele Cortinovia assisted me with SiPM characterizations, Dr. Jiaguo Zhang, Jörn Schwandt and Ioannis Kopsalis helped me with the sensor irradiation, Dr. Stefan Mättig, Dr. Jenny Sibille Pöhlsen, Milan and Alessandro offered their helps in correcting my thesis, Peter Buhmann and Michael Matysek maintain the equipments and coordinate the laboratory and many more people who have helped me in different ways. Although your names are not mentioned here, your helps have not gone unnoticed. All my colleagues from the two groups make the place a pleasant and inspiring working environment.

Finally, I would like to thank my parents, my beloved wife and all my friends, your understanding and supports provide me strength and willpower to finish my thesis.